Efects of External Electric Field, Magnetic Field, and Magnetic Anisotropy on the Magnetic Properties of Fe Alloyed GaSb Diluted Magnetic Semiconductor and First Principle Study of its Structural and Electronic Properties

By

Mesfin Birile Woldetsadik

A Dissertation Submitted to

the Department of Physics of Addis Ababa University

in Partial Fulfillment of the Requirements for the

Degree of Doctor of Philosophy in Physics

Addis Ababa

Ethiopia

August, 2020

ADDIS ABABA UNIVERSITY

DEPARTMENT OF PHYSICS

The undersigned hereby certify that they have read and recommend to the College of Natural and Computational Sciences for acceptance a thesis entitled **Efects of External Electric Field, Magnetic Field, and Magnetic Anisotropy on the Magnetic Properties of Fe Alloyed GaSb Diluted Magnetic Semiconductor and First Principle Study of its Structural and Electronic Properties** by **Mesfin Birile Woldetsadik** in partial fulfillment of the requirements for the degree of **Doctor of Philosophy**.

Dated: **August 2020**

Approved by the Examination Committee

External Examiner: _____

Dr. Sudip Chakraborty

Internal Examiner: _____

Dr. Belayneh Mesfin

Advisor: _____

Prof. P. Singh

Co-Advisor: _____

Dr. Chernet Amente

Chairman: _____

Dr. Teshome Senbeta

ADDIS ABABA UNIVERSITY

Date: **August 2020**

Author: Mesfin Birile

Title: **Efects of External Electric Field, Magnetic Field, and Magnetic Anisotropy on the Magnetic Properties of Fe Alloyed GaSb Diluted Magnetic Semiconductor and First Principle Study of its Structural and Electronic Properties**

Department: **Physics**

Degree: **Ph.D.** Convocation: **August** Year: **2020**

Permission is herewith granted to Addis Ababa University to circulate and to have copied for non-commercial purposes, at its discretion, the above title upon the request of individuals or institutions.

Signature of Author

Dedication

This dissertation is dedicated to:

My Mother W/ro Kelmua Auwgchew and father Ato Birile Woldetsadik (who are unlucky to see these good days)

Contents

List of Figures

List of Tables

Abstract

Starting with a Kondo lattice model type Hamiltonian, we have studied the effects of impurity concentration x, electric field, magnetic field, and magnetic anisotropy energy on the magnetic properties of $Fe/GaSb$ diluted magnetic semiconductor. Analytical technique is employed to analyze the magnon dispersion relation, magnetization, critical temperature T_c, specific heat capacity, and susceptibility of the system. Our analysis indicate the enhancement of T_c with increasing impurity concentration x and/or with the magnetic and electric fields. Due to the inclusion of the magnetic anisotropic energy, we could identify a significant reduction of magnon dispersion/band gap energy and a slight reduction of magnetization. It is also shown that electric field and magnetic field have the tendency of enhancing the magnetic susceptibility and lowering the magnon specific heat when applied separately or simultaneously. On the other hand, the magnon specific heat tends to slightly increase contrary to the magnetic susceptibility with increase in magnetic anisotropic energy. We have also investigated the structural and electronic properties of both pristine and Fe alloyed GaSb semiconductor using generalized gradient approximation method (GGA) for versatile pseudopotentials within the density functional theory (DFT) using Quantum ESPRESSO package. These first-principles studies compare the lattice parameters, the band structures, the density of states, and the corresponding projected states of Fe/GaSb and GaSb. Our findings are in good agreement with experimental results showing 1.5 to 2% lattice parameter and 10% band gap variations and also within 3% band gap error from previous DFT calculations for GaSb. Moreover, the Hubbard model (DFT+U) calculations are performed for the energy band gap correction for the doped system.

Acknowledgements

First and foremost, I would like to thank God for giving me the blessing, knowledge, strength and ability to complete this PhD study. I would like to express my gratitude to my advisor Prof. P. Singh, who formulated the problem for this PhD dissertation and has always been a truly inspiring advisor and my co-advisor Dr. Chernet Amente for his endless support, patient guidance, invaluable encouragement and excellent advice for the successful completion of this research work.

My deepest gratitude also goes to my colleagues, all staff members of the Department of Physics, AAU. Specially, Dr. Belayneh Mesfin and Dr. Deribe Hirpo for their motivation and unreserved support in my quest for knowledge. Their brotherly approach, passion and work discipline is indescribable. Dr. Theshome Senbeta, head of the Department, who works day and night to facilitate all the official matters to all the staff members and students fairly. Moreover, Dr. Mulugeta Bekele for welcoming and paving the road to me to be part of the staff members of the Department of Physics, the secretary W/ro Tsilat Adinew for her unreserved encouragement and motherly approach, and Ato Debebe Mamo for his day to day motivation. Had it not been with you this work would not have been completed.

My special thanks also goes to my fellow PhD students specially Abebe Tadesse for his computational and technical assistance. I should not forget to thank all my friends and others that inspired and supported me in any way.

I would also like to thank the Department of Physics, Addis Ababa University for sponsoring this PhD study.

My deepest thanks also goes to my wifes families (W/ro Tikikle Zigido, Ato Bogale Demissie, her brothers and sisters and Dr. Akalu Lentro) for their love and continual support.

Finally, I take this opportunity to express my profound gratitude to my sisters and brother, specially W/ro Zenebech Birile for her love, moral support and being like mom; my wife Hirut Bogale, for her love, encouragement, for taking care of our children and made my life an enjoyable one. I also want to thank my children: Bethel, Dagmawit and Emmanuela, for the happiness and inspiration they bring to me.

Chapter 1

General Introduction

The realization of materials that combine semiconducting behavior with robust magnetism has long been a dream of material physics [1, 2]. One strategy for creating systems that are simultaneously semiconducting and magnetic, initiated in the late 1970s is to introduce local moments into well-understood semiconductors. The result is a new class of materials now known as diluted magnetic semiconductors (DMSs) [3]. Such a compound is an alloy between a non-magnetic semiconductor and a magnetic element like the transition and rare-earth elements.

Since the initial discovery of DMS in II-VI semiconductor compounds [3], many papers have been published investigating DMSs electronic, magnetic, optical, thermal, transport, and statistical properties, in many journals, and even in popular magazines [4]. This interest not only comes from the DMS themselves as good theoretical and experimental subjects, but also can be better understood from a broader view from the relation of DMS research with spintronics [3, 5].

Mn-doped GaAs has become, among DMS materials, one of the best candidates for technological application. Recently, the Mn-doped III-V semiconductors has been studied and a critical temperature T_c up to 200 K [6] was achieved by patterning a heavily Mn-doped $(Ga_{1-x}, Mn_x)As$ thin film into nanostructures engineering, which is quite promising although still too low for the envisaged room temperature (RT) applications. However, Mn-based DMSs have not been put to practical use because of the following three obstacles: (i) T_c is still lower than RT; (ii) the solubility of Mn in III-V semiconductors is quite low; and (iii) the Mn atoms substituted at cation sites in III-V group semiconductors behave as Mn^{2+} acceptors, so that n-type DMSs cannot be

produced [7].

In order to overcome the problems noted above, Fe-based DMSs have recently been attracting much attention. In particular, in Fe-doped III-V semiconductors, the substitutional Fe atoms are expected to exist as a neutral state (Fe^{3+}), in which case they will not provide extrinsic carriers for the system [8]. Thus, the conduction carriers are not provided by the dopant Fe impurities but instead are supplied from the conduction or valence bands. Since the effect of impurity scattering is small, the coherence length is increased. This provides the possibility of realizing new functionalities, such as low power consumption and high-speed operation, due to the quantization of the electronic structures. It is also note-worthy that both n- and p-type DMS systems can be fabricated easily since the carrier characteristics can be controlled independently of the Fe impurities [7].

Inspired by these fascinating electronic and magnetic properties, researchers have worked to understand the ferromagnetic mechanism in Fe-based DMSs. Hai, et al. have succeeded in fabricating (In,Fe)As, which is an n-type ferromagnetic DMS, and have obtained $T_c \leq 70\ K$ [9, 10, 11]. Recently, Tu, et al. [12, 13] have developed a new p-type Fe-doped intrinsic III-V ferromagnetic semiconductor $(Ga_{1-x}, Fe_x)Sb$, which demonstrated ferromagnetism up to 340 K for an Fe concentration of $x = 25\%$ without any other secondary phases such as metallic Fe, intermetallic Fe-Sb, or Fe-Ga precipitation. A number of experimental works have also shown the appearance of a ferromagnetic ordering in III-V semiconductor hosts heavily doped with Fe atoms, in particular, (In,Fe)As [8, 14], and (Al,Fe)Sb [15].

In the present thesis, we have studied magnetic properties of $Fe/GaSb$ diluted magnetic semiconductor by varying the impurity concentration x and/or electromagnetic fields, and/or magnetic anisotropic energy, and the structural and electronic properties of both GaSb semiconductor and $Fe/GaSb$ diluted magnetic semiconductor (DMS). The thesis is organized as follows: Chapter 1 is devoted to literature reviews of novel DMSs, origins of ferromagnetism, theoretical models of ferromagnetism, and brief discussions of previous computational and experimental works along with the results obtained. Chapter 2 and 3, starting with a model Hamiltonian consisting of local and itinerant electrons, the interaction of itinerant electrons with localized moments in the form of s-d exchange interaction and their interaction with magnetic fields, elec-

tric fields, and magnetic anisotropic energy, we investigate the effect of impurity concentration and/or the electromagnetic fields and/or the magnetic anisotropic energy on the magnetic properties in the $Fe/GaSb$ DMS system employing analytical method. We find that the magnetic properties are influenced by the electromagnetic field and magnetic anisotropic energy for applications in spintronics, information storage and processing. Chapter 4 presents basic introduction of density functional theories (DFTs) and practical calculations in DFTs. In Chapter 5, we investigate the structural and electronic properties of pristine and Fe doped GaSb within DFTs employing quantum ESPRESSO software package. Finally, the summary and conclusion of the overall work is presented.

Chapter 2

Literature Review

2.1 Introduction

Semiconductor physics and magnetism are established subfields of condensed matter physics that continue to reveal a rich variety of unusual phenomena, often in new types of solid-state materials. Integrated circuits and high-frequency devices made of semiconductors, used for information processing and communications, have had great success using the charge of electrons in semiconductors. Mass storage of information indispensable for information technology is carried out by magnetic recording (hard disks, magnetic tapes, magneto-optical disks) using spin of electrons in ferromagnetic materials. It is then quite natural to ask if both the charge and spin of electrons can be used to further enhance the performance of devices. We may then be able to use the capability of mass storage and processing of information at the same time [3, 4].

Dilute magnetic semiconductors are class of magnetic semiconductors, materials possessing magnetic and semiconducting properties, in which a fraction of the cations is replaced by magnetic ions (see Fig. 2.1). The exchange interaction between the spin of the dopant atoms and the carriers in the semiconductor host is expected to bring about global ferromagnetic order in the entire lattice in these materials. The transport, optical, and magnetic properties of the host semiconductors will be altered due to the exchange interaction between the conduction carriers and the localized moments of the magnetic ions.

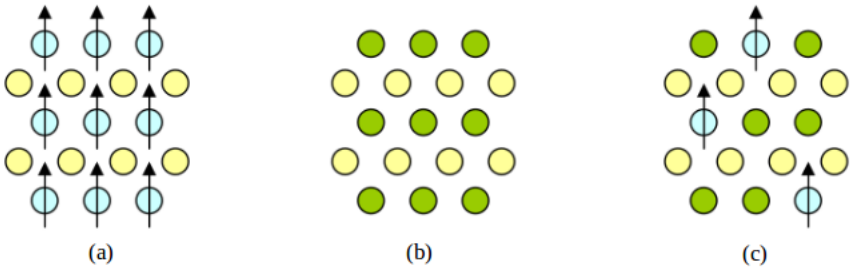

Figure 2.1: Schematic showing (a) a magnetic semiconductor, (b) a non-magnetic semiconductor, and (c) a diluted magnetic semiconductor [16].

The emerging research area known as 'spintronics' or spin-based electronics seeks to extend the properties and applications of established devices by making use of the spin of electrons in addition to their charge.

Spin orientation of conduction electrons survives for a relatively long time (nanoseconds compared to tens of femtoseconds during which electron momentum and energy decay), which make spintronic devices particularly attractive for memory, storage, and magnetic sensors applications, and potentially for quantum computing where electron spin would represent a bit (called qubit) of information instead of the on or off positions of a conventional computer circuit. What is expected from these materials is to have a large commercial and economic impact in non-volatile memories in contrast to semiconductor memories that we use today.

In this Chapter, a literature review of the search for novel III-V based diluted magnetic semiconductors, origin of ferromagnetism, theoretical models of ferromagnetism, properties of GaSb semiconductors, and experimental works on Fe doped GaSb diluted magnetic semiconductor are presented.

2.2 The Search for Novel DMSs

Magnetic semiconductor such as europium chalcogenides EuX, with X = O, S, Se, Te, and Cr-spinels which are families of important AB_2X_4 oxide minerals, where A and B are metal ions and X = O, S, Se, have been extensively studied since the 1960s [17]. The identification of EuO by Matthias, et al. [18], which was reported as truly ferromagnetic at 77 K with saturation moment

of close to 7 Bohr magnetons ($7\mu_0$), is the first rare earth oxide to be found to become ferromagnetic with true ferromagnetic coupling. This is the first motivation for further investigations of europium chalcogenides as magneto-optic memories in computers and magneto-optic modulators [19]. However, structures of those composites are different from Si or GaAs: the crystals are very hard to be produced in experiment, have low Curie temperature T_c (50 K or lower), strong insulation, and poor semiconducting transport property [16], hence those composites further hampered their value in application.

In diluted magnetic semiconductors, the cations of semiconductor materials are partially substituted with a transition-metal impurity, such as iron (Fe), chromium (Cr), cobalt (Co) and manganese (Mn) or with rare-earths [1, 20]. These magnetic impurities can be incorporated in the lattice up to large alloy fraction preserving the crystalline and band structure of the host semiconductor [21].

The early work on DMS started in 1980s, when typically transition metal, Mn is substituted on a small fraction, x, of a host semiconductor in II-VI compounds. Therefore, the compounds are expressed as $(II_{1-x}Mn_x)VI$ which becomes $(Zn_{1-x}Mn_x)Se$, $(Cd_{1-x}Mn_x)Te$ [20, 22] and so on. Tremendous progress was made in the understanding of exchange interactions between magnetic moments of the dopants and the charge carriers in the host. However, their spin glass behavior or weak ferromagnetism, with T_c of only a few Kelvin served as impediments in the development for applications requiring ferromagnetic order at room temperature [23].

Nevertheless, this was a precedent to research into III-V materials as potential DMS candidates. A T_c of 173 K was achieved in Mn-doped GaAs by using low temperature annealing techniques which is quite promising [24, 25]. However, the much lower solubility of Mn in III-V semiconductors, compared to II-VI semiconductors, along with its poor stability and low Curie temperature are found to be the main barrier for fabrication. In order to have ferromagnetism in such DMS, a sizable amount of magnetic ions are needed.

A rapid progress of DMS research in 1990s stemmed, to a large extent, primarily by molecular beam epitaxy (MBE) and by laser ablation. These methods have made it possible to obtain DMS with the content of the magnetic constituent beyond thermal equilibrium solubility limits from the development of methods of crystal growth [16].

A breakthrough was made by Ohno and Munekata [1] on Mn doped InAs using MBE technique and this initial work opened up the technologically significance of III-V semiconductors as potential hosts for DMS applications and ferromagnetism was observed in p-type InMnAs.

Recently, the Mn-doped III-V semiconductors has been studied and a T_c up to 200 K was achieved by patterning a heavily Mn-doped $Ga_{1-x}Mn_xAs$ thin film into nanostructures engineering [26]. Although still the obtained temperature is too low for the envisaged room temperature applications, this field has been advancing rapidly ever since. However, the search for better materials and an understanding of the physical mechanisms underlying the magnetism is an ongoing process.

More recently, a number of experimental works have shown the appearance of a ferromagnetic ordering in III-V semiconductor hosts heavily doped with Fe atoms, in particular, (Ga,Fe)Sb [12, 13], (In,Fe)As [8, 14], and (Al,Fe)Sb [15]. Accordingly, up to 25% sizeable amount of Fe impurity relative to the Ga content could be introduced into GaSb semiconductor host without the formation of second-phase. The obtained result indicates that (Ga,Fe)Sb thin film layers prepared by MBE demonstrated ferromagnetic property up to a temperature of 340 K [13] and hence, entail further analysis using different techniques as well.

The search for novel DMS candidates has concentrated on three major fronts: i) the microscopic origins and fundamental physics of the ferromagnetism that occurs in these systems, ii) the materials science of growth and defects, and iii) the development of spintronic devices with new functionalities.

2.3 Origin of Ferromagnetism

Magnetism cannot be separated from electricity, because electron revolving around a nucleus in an atom produces a small magnetic field [27]. The magnetic behavior of materials can be classified into five major groups: diamagnetism, paramagnetism, ferromagnetism, ferrimagnetism and antiferromagnetism [28].

Diamagnetism is caused by the orbital motion of electrons creating tiny current loops and when an external magnetic field is applied to a material, these current loops tend to align in

such a way as to oppose the applied field and paramagnetism occurs when a material becomes magnetic temporarily when placed in a magnetic field and reverts to its nonmagnetic states as soon as the external field is removed [29].

In a ferromagnet, in addition to the electrons' intrinsic magnetic moment's tendency to be parallel to an applied field, there is also a tendency for these magnetic moments to orient parallel to each other to maintain a lowered-energy state. Thus, even in the absence of an applied magnetic field or electric current, the magnetic moments of the electrons in the material spontaneously line up parallel to one another [29]. Ferromagnetism is then a phenomenon by which a material can exhibit this spontaneous magnetization and it is one of the strongest forms of magnetism. It is responsible for most of the magnetic behavior encountered in every day life and is the basis for all permanent magnets (as well as the metals that are noticeably attracted to them).

In particular, a material is ferromagnetic in narrower sense only if all of its magnetic ions add a positive contribution to the net magnetization. If some of the magnetic ions add a negative contribution to the net magnetization (if they are partially anti-aligned), then the material is ferrimagnetic. If the ions anti-align completely so as to have zero net magnetization, despite the magnetic ordering, then it is an antiferromagnet [29]. Antiferromagnets have a zero net magnetic moment, meaning no field is produced by them and are less common compared to the other types of behaviors, and are mostly observed at low temperatures.

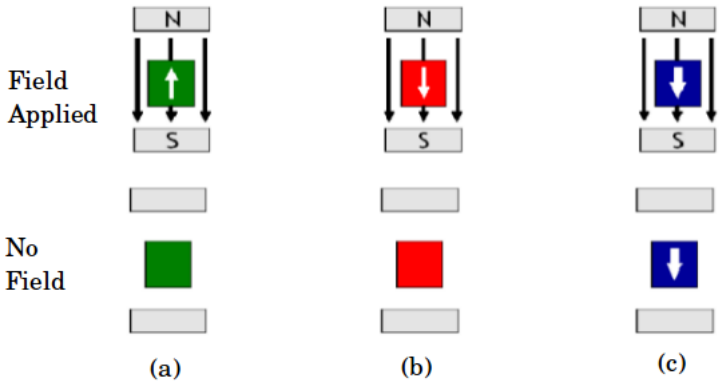

Figure 2.2: Macroscopic behavior observed in (a) diamagnetic, (b) paramagnetic, and (c) ferromagnetic materials [29].

All of these alignment effects only occur at temperatures below a certain critical temperature, called the Curie temperature T_c [29] (for ferromagnets and ferrimagnets) or the Neel temperature (for antiferromagnets). Curie temperature is the temperature above which the material cease to exhibit spontaneous magnetization. If the crystal symmetry is such that the localized dipole moment alignment at different lattice sites results in a net macroscopic magnetization at $T = 0\ K$ even in the absence of an external magnetic field then such a solid is referred to as ferromagnetically ordered (see Fig. 2.2). Unlike paramagnetic materials, the atomic moments in these materials exhibit very strong interactions. These interactions are produced by electronic exchange forces and result in a parallel or antiparallel alignment of atomic moments. The exchange force is a quantum mechanical phenomenon due to the relative orientation of the spins of two electrons.

Fig. 2.3 shows the reduction of magnetization with the increase in temperature and the temperature dependence of the magnetic susceptibility of ferromagnet. The susceptibility, χ, of a ferromagnet above the Curie temperature has the form

$$\chi = \frac{C}{T - T_c}. \tag{2.3.1}$$

This is the Curie-Weiss law in the mean field approximation with Curie constant C for $T > T_c$.

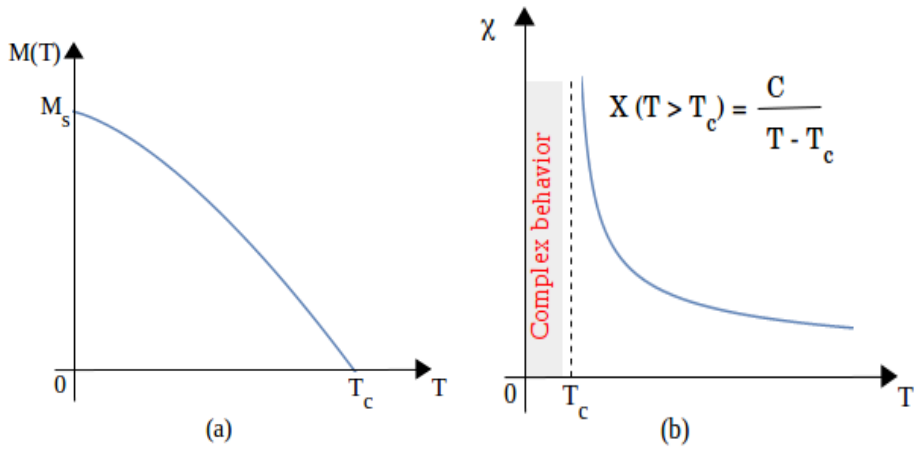

Figure 2.3: (a) Variation of the saturation magnetization with temperature and (b) Temperature dependence of the magnetic susceptibility of a Ferromagnet [29].

Ferromagnetism can be as strong as chemical bonds. Very often the quantum ground state of a many-electron system has nonzero local spin density, aligned either in the same direction in space at every point in the system as in simple ferromagnets, or in noncollinear, ferrimagnetic, or antiferromagnetic materials in congurations in which the spin direction varies spatially.

III-V semiconductors when doped with transition metal, those have been mainly used so far such as Mn, Fe, and Cr, the Mn^{2+} or Fe^{3+} ions mostly substitute III atoms in the host semiconductor. These Mn^{2+} and Fe^{3+} ions provide angular momentum $L = 0$ and $S = 5/2$ magnetic moments due to their half-filled 3d shells. Depending on their concentration and energetic position within the band gap, the Mn^{2+} or Fe^{3+} states can either form an impurity band or they act as an impurity level, creating valence band holes. Besides, Mn, and Fe can also occupy interstitial positions in the zinc blende lattice. The dependence of the energy of the system on the relative orientation of Mn or Fe moments is generally referred to as an exchange interaction [6, 30].

2.3.1 Exchange Interaction

In physics, the exchange interaction (with an exchange energy and exchange term) is a quantum mechanical effect that only occurs between identical particles. Both bosons and fermions can experience the exchange interaction. For fermions, the exchange interactions are due to Pauli's exclusion principle which is purely electrostatic or Coulombic in origin. Qualitatively speaking, Pauli's exclusion principle prohibits two electrons with same spin from taking same state and hence on an average they would be farther apart and therefore Coulombic interaction energy would be lowered compared to the case when two electrons have opposite spin and hence can occupy same state. For bosons, the exchange interaction takes the form of an effective attraction that causes identical particles to be found closer together, as in Bose-Einstein condensation. The most common exchange interactions [6, 30] which are dominant in DMSs are listed bellow:

(a) Super-Exchange Interaction

In cases when paramagnetic ion/atom electron clouds do not overlap and there is another non-paramagnetic ion/atom sitting in between, we call such interactions as superexchange interaction.

It is a result of the electrons having come from the same donor atom and being coupled with the receiving ions spins; and the interaction takes place via this intermediate nonmagnetic ion [31].

(b) Direct or Potential Exchange Interaction

It arises from the direct Coulomb interaction between spins (s-d interaction). It was formulated to describe magnetic behaviour in conventional materials like Fe, Co, and Ni. The interaction occurs when the magnetic ions interact through their overlapping charge distributions [32].

(c) Indirect Exchange Interaction

In the sea of conduction electrons, two paramagnetic ions/atoms can interact with each other by the mediation of free electrons. This type of exchange interaction is called indirect exchange interaction. One of the main mechanisms for indirect exchange interactions in DMS is RKKY (Ruderman-Kittel-Kasuya-Yosida) mechanism [32]. Fig. 2.4 shows the above three types of exchange interaction.

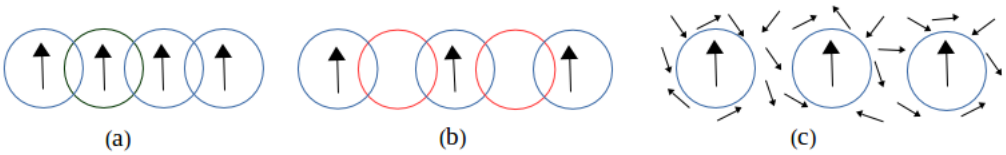

Figure 2.4: Schematic illustration of (a) direct exchange, (b) super-exchange, and (c) indirect exchange [32].

2.3.2 Exchange Interactions Included in DMS

Spin-spin exchange interaction is the key point through which various magnetic moments are formed. In DMS, exchange interaction include interactions between s electrons in conduction band, p electrons in valence band, and d electrons from magnetic ions (s-d and p-d exchange interaction), and interactions between d electrons from magnetic ions (d-d exchange interaction) [33].

(a) s-d Interaction

It is the interaction between conduction s band electron spins and magnetic ion spins resulting from the Coulomb interaction. These interactions are ferromagnetic in nature and their exchange energy value is close to 0.2 eV, almost for all DMSs.

(b) p-d Interaction

It is the interaction between valence charge carriers and localized magnetic ion spins. These interactions are anti-ferromagnetic (negative exchange energy) in nature. The exchange energy value is six to eight times greater than s-d interaction.

Both s-d and p-d interactions are described by Kondo-like Hamiltonian given by [19]

$$H_{ex} = -J(r - R_i)\mathbf{s}.S_i, \tag{2.3.2}$$

where s is a spin operator of the band electron or hole, S_i is a spin operator of the magnetic ion which is localized in the crystal lattice point, R_i, and $J(r - R_i)$ is the exchange integral.

(c) d-d Interaction

The d-d interaction is the interaction between localized magnetic ion spins. This interaction is also known as Heisenberg exchange interaction and is given by the following Hamiltonian.

$$H_{ij} = -\sum_{i=j} J_{dd}(R_{ij})\mathbf{S}_i.\mathbf{S}_j, \tag{2.3.3}$$

where $J_{dd}(R_{ij})$ is the localized magnetic ion spins exchange integral.

2.4 Theoretical Models of Ferromagnetism

All proposed models of ferromagnetism in III-V DMS can be classified into two major groups: ab-initio or first principle studies, and (semi)-phenomenological models that start from an effective Hamiltonian that incorporates the principal features of the material.

First principle studies are based on the parameter-free calculations within the density functional theory (DFT) (see, e.g., reviews [34, 35] and more recent work [36, 37]). The DFT heavy computer calculations intend to treat realistic systems in their detailed complexity starting from the electronic properties of constituent atoms. In particular, every electron state is involved in effective exchange interaction with all other electron states. Therefore, different types of exchange interactions intermix and influence each other. The complexity of the DFT picture reflects the complexity of the real systems. To gain deeper qualitative understanding of the magnetism of the system, it is, however, very useful to relate the DFT results to the results of the model-Hamiltonian treatments attempting to single out the leading exchange mechanisms responsible for establishing the long-range magnetic order.

(Semi) phenomenological models study the problem with an effective Hamiltonian containing experimentally determined parameters and are more interesting since the underlying physics is more transparent and open for further investigation. The starting Hamiltonian usually takes into account only interaction between two (neighboring) impurities, or one impurity and the environment (see, e.g., reviews in [38, 39]). Different assumptions concerning the energy position and the role of the 3d sates of the magnetic impurities are formulated. Sometimes the strength of this interaction is extracted from first principle calculations. Although a number of different theories have been proposed and most of the model-Hamiltonian studies agree with each other in that the presence of holes plays important role in ferromagnetism of DMS, the mechanisms responsible for the origin of ferromagnetism in diluted magnetic semiconductor is not fully understood and explained yet.

A key issue [40] for the theory of the III-V DMS ferromagnets is whether the carriers end up residing in a tightly bound anti-bonding state that has primarily d-character, or in a more spatially extended structure that has primarily the p-character of the host valence band. Because the moments in DMS systems are dilute, large values for the inter-moment couplings responsible for carrier-mediated ferromagnetism require acceptor level states that extend over at least a few lattice constants.

The theoretical models that have been most commonly used to explain ferromagnetism in diluted magnetic semiconductors are discussed below.

(a) The RKKY Model

This model is based on the long-range indirect exchange interaction that was developed to explain the ferromagnetism in rare-earth metals, where there is no direct overlap among the magnetic electrons. The RKKY interaction was originally developed by M.A. Ruderman and Charles Kittel in the 1950's as a way to describe unusually broad nuclear spin resonance lines that had been observed in natural metallic silver. The initial model was based on second-order perturbation theory to describe an indirect exchange where the nuclear spin of one atom interacts with a conduction electron via the hyperfine interaction, and this conduction electron then interacts with another nuclear spin thus creating a correlation between the two nuclear spins. Later the model was extended by Kasuya and Yosida to explain ferromagnetism in rare-earth metals. When a magnetic impurity is placed in a metal, the free electrons tend to align their spin in such a way to screen the spin of the impurity. The polarization of the free electrons around the impurity has an oscillatory behavior similar to Friedel oscillations when a charged impurity is screened. The spin polarization of conduction electrons governs the indirect interaction of two neighboring atoms which is characterized by the coefficient $J_{RKKY}(r_{ij})$ that appears in a simple effective Hamiltonian:

$$H_{ij} = -\sum_{i \neq j} J_{RKKY}(r_{ij}) \mathbf{S}_i . \mathbf{S}_j . \tag{2.4.1}$$

The RKKY exchange coefficient, J_{RKKY}, oscillates from positive to negative as the separation of the ions changes and has the damped oscillatory nature shown in Fig. 2.5. Therefore, depending upon the separation between a pair of ions their magnetic coupling can be ferromagnetic or antiferromagnetic. A magnetic ion induces a spin polarization in the conduction electrons in its neighborhood. This spin polarization in the itinerant electrons is felt by the moments of other magnetic ions within range, leading to an indirect coupling.

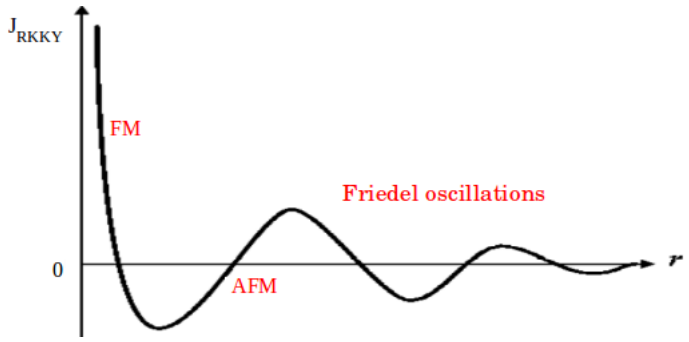

Figure 2.5: Variation of the indirect exchange coupling constant, J_{RKKY}, of a free electron gas in the neighborhood of a point magnetic moment at the origin $\boldsymbol{r} = 0$ [41].

The RKKY interaction as a mechanism to describe ferromagnetism in (Ga,Mn)As was first proposed by Matsukura, et al. [41]. However, a further investigation by many authors [44, 45] revealed that this mechanism is not reliable for diluted magnetic semiconductors since the distance between the carriers is larger than the average distance between two magnetic impurities. This is due to the self-compensation by MnI and AsGa that makes the concentration of holes significantly smaller than Mn density as explained earlier.

(b) The Heisenberg Models

The starting point of this model is the effective Hamiltonian proposed by Heisenberg [46]:

$$H_{ij} = -\sum_{i \neq j} J(r_{ij}) \mathbf{S}_i . \mathbf{S}_j . \tag{2.4.2}$$

The indices i, j run over the (random) positions of the magnetic atoms. The value of the exchange coupling constant $J(r_{ij})$ is either extracted from first principle studies [47], or from some band theory [48]. The Curie temperature evaluated through a mean field approximation is usually rough and yields an overestimation. One of the successes of the mean field theories is the prediction of the dependence of T_c on the hole density p for small concentration of Mn, which is roughly given by:

$$T_c = cxp^{1/3}, \tag{2.4.3}$$

where x is the magnetic impurity concentration, p is the hole concentration, and c is a constant specific to the host material.

(c) The Mean-Field Zener Model

Mean-field Zener model, as proposed by Dietl, et al. [49] is one of the most accepted model for ferromagnetism in (Ga,Mn)As and related DMS materials. The theory proposed by Zener [50] indicates that the direct super-exchange interaction [49] between half-filled d-shell electrons of transition metal (TM) cations and completely filled p-orbitals of anion is antiferromagnetic (see Fig. 2.6).

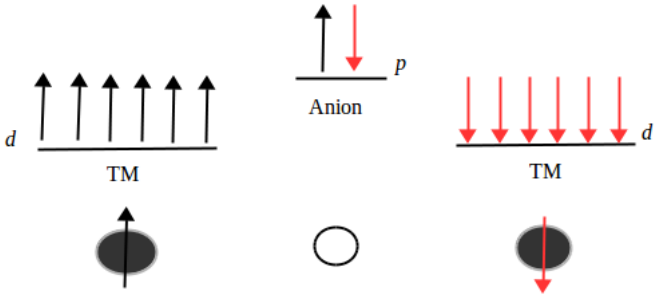

Figure 2.6: Direct super exchange interaction: Antiferromagnetic coupling of adjacent TM cations through shared anion [41].

Since the d-shell electrons from both adjacent TM atoms occupy the same p-level, their spins must be opposite according to Pauli exclusion principle. This leads to an antiferromagnetic coupling of nearest-neighbor TM cations through a shared anion. On the other hand, the indirect super exchange interaction between localized d-shell electrons of TM cations mediated by the delocalized band carriers tends to align the spin of the partially filled d-shells in a ferromagnetic manner (see Fig. 2.7).

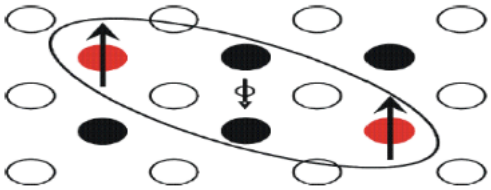

Figure 2.7: The mean-field model: Ferromagnetic coupling of localized Mn spins through the free holes [41].

In the Zener model, ferromagnetism is only possible when the indirect exchange interaction dominates over the direct super exchange interaction.

2.5 The GaSb Semiconductor

Gallium, aluminium and indium antimonides (GaSb, AlSb, InSb) are semiconductors of the group III-V family. The III-V binary compounds are of a great interest to the technological industry due to their applications in electro-optical devices. Indium antimonide photodiode detectors are photovoltaic, generating electric current when subjected to infrared radiation. A layer of indium antimonide sandwiched between layers of aluminium indium antimonide can act as a quantum well. This approach is studied in order to construct very fast transistors [51].

Pristine GaSb is always p type in nature irrespective of the growth technique and conditions and it can be used for infrared detectors, infrared light emitting diodes (LEDs), lasers and thermo-photovoltaic systems [52]. Work over the last three decades has been devoted mainly for understanding the nature and the origin of the residual acceptors which are the limiting factors for both fundamental studies and device applications. The residual acceptors with concentration of $\approx 10^{17}\ cm^{-3}$ have been found to be related to gallium vacancies (V_{Ga}) and gallium in antimony site (Ga_{Sb}) with doubly ionizable nature [53]. Attempts have been made to reduce their content by growing the crystals from nonstoichiometric melts [54]. Recent studies on epitaxial layers of GaSb grown by liquid phase epitaxy [55] and molecular beam epitaxy (MBE) with excess antimony [56] have shown the possibility of reducing substantially, the level of natural acceptors, and increasing the hole mobility. This stimulated the renewed interest in growth of GaSb crystals with reduced residual acceptors.

At present, GaSb technology is in its infancy and significant progress has to be made both in materials and processing aspects before it can be employed for device applications. Current research and developments are focused on areas of high quality materials growth, better understanding of electronic and photonic properties and fabrication of suitable device structures.

Iron being ferromagnetic in nature provided the necessary impetus to explore the structural and electronic changes by doping of iron on these antimonides. Doping of transition metals in group III Antimonides is important and has practical uses.

The band structure, effective masses, and transport properties are the most important features which describe the general nature of the GaSb semiconductor compound. The increased interest to this material may be explained by the unique feature of GaSb very narrow energy gaps, high mobility, and small effective masses of carriers and due of this the possibilities of practical applications in high frequency semiconductor devices (Gunn diode) [57]. There is also considerable scientific interest in all mixed III-V compounds of Ga series. The continuous variability of parameters in such kinds of materials makes possible the design of a material with virtually any gap width within the given range. The designability of such materials is especially useful for infrared or optical devices in which operation over particular wavelength ranges is required, such as in infrared sensors and injection lasers [58].

2.5.1 Crystalline Structure

The crystal lattice of GaSb belongs to the zinc-blende lattice, which is more common in III-V semiconductor based DMSs. The zinc-blende crystal consists of two identical interpenetrating face centered cubic (fcc) sublattices, formed by Ga and Sb atoms, are shifted by the fourth of the cubic diagonal relative to each other. The resulting structure is invariant under the symmetry operations of the tetrahedral point symmetry group and can be characterized by a single lattice constant a as illustrated in Fig. 2.8. In this configuration each ion is surrounded by four nearest neighbor ions of the different sublattice forming an equilateral tetrahedron with the edge length of $\frac{\sqrt{2}}{2}a$. The chemical bonds are established by the strongly hybridized s and p atomic shells. The resulting orbitals are oriented towards the first neighbor sites. The lack of inversion symmetry in the zinc-blende lattice also contributes to the spin-orbit interaction of the delocalized carriers,

and hence to the related spin transport.

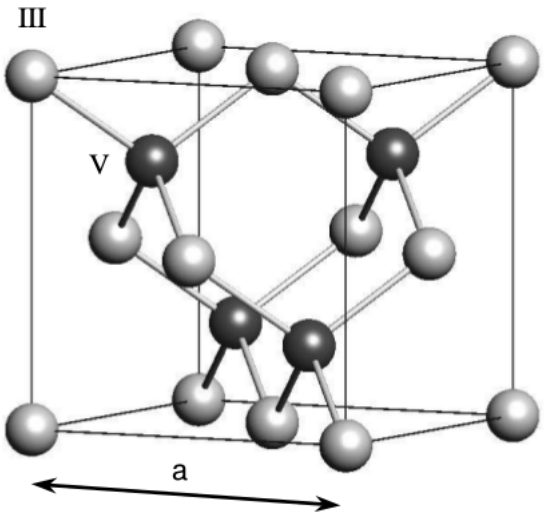

Figure 2.8: The Bravais cell of a (III,V) compound zinc-blende semiconductor. The crystal is characterized by a single lattice constant a [41].

2.5.2 Energy Band Structure

The conduction band in GaSb is characterized by three sets of minima; the lowest minima at Γ, slightly higher minima at the L-points at the surface of the Brillouin zone, and even higher minima at the X-points. The band structure along the symmetry lines of the Brillouin zone is displayed in Fig. 2.9 for GaSb.

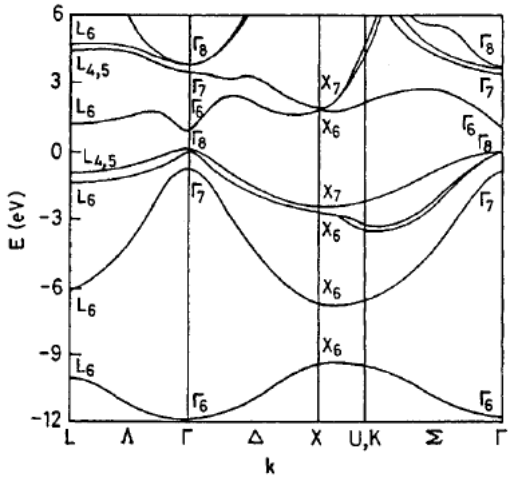

Figure 2.9: Band structure of GaSb obtained with a non-local pseudopotential calculation [42].

In the direct band material such as GaSb the position of minima at X and L can be determined by Hall effect and by study of the pressure dependence of resistivity. The measurements of ultraviolet reflectivity helps to determine the band gaps.

2.5.3 Transport Properties

By transport properties we mean the response of the electrons to applied forces. The important point is that an electron in a periodic potential is accelarated relative to the lattice in an applied electric or magnetic field as if the mass of electron were equal to an effective mass which differs from the mass of free electron. In order to get correct equations of motions, we have to take into account the effective masses of electrons. Effective mass is one of the important concepts in the analysis of semiconductors theory of scattering. In GaSb, the conduction band lowest valley occurs at the same k-value as the valence band maximum (for instance $k = 0$). It means that GaSb belongs to a direct gap semiconductors. The curvatures (or effective masses) of valence and conduction band edges are important features of transport properties of GaSb and is illustrated in Fig. 2.10. For GaSb, the experimental parameters, the effective mass of carriers in the Γ valley, $m_c = m_e = 0.041\ m$, where m is the free electron mass and the effective mass $m_\Gamma = 0.05\ m_e$.

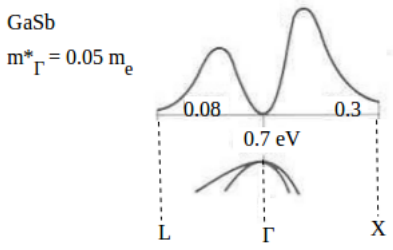

Figure 2.10: Effective masses in the energetic valleys of GaSb [43].

The large curvature of the band structure in Γ valley results in a low effective mass and corresponding high mobility of the conduction electrons. High electron mobility is used to good purpose in galvanomagnetic devices, based on either the Hall effect (proportional to μ, electron mobility) or magnetoresistance (proportional to μ^2). The high mobility also implies that conduction electrons acquire a high drift momentum in an electric field and hence there is strong energy transfer to the electron assembly leading to pronounced "hot electron" effects [30]. Table

2.1 summarizes some of the important material properties of GaSb.

Basic parameters of GaSb at room temperature	**Obtained Results**
Crystal structure	Zinc Blende
Number of atoms in 1 cm^3	3.53×10^{22}
Debye temperature	266 K
Density	5.61 g cm^{-3}
Effective electron mass	0.041 m_e
Lattice constant	6.09593 $\mathring{A}$
Optical phonon energy	0.0297 eV
Energy gap	0.726 eV
Energy separation ($E_{\Gamma L}$) between Γ and L valleys	0.084 eV
Energy separation ($E_{\Gamma X}$) between Γ and X valleys	0.31 eV
Intrinsic resistivity	10^3 Ω cm
Effective conduction band density of states	2.1×10^{17} cm^{-3}
Intrinsic carrier concentration	1.5×10^{12} cm^{-3}

Table 2.1: Some Material properties of GaSb [30].

2.6 Experimental Work on Fe Alloyed GaSb DMS

To the best of our knowledge, no thorough study of iron doped group III antimonides have been carried out so far in the literature. However, experimental works illustrated that (Ga,Fe)Sb is a new p type ferromagnetic semiconductor (FMS) with zinc-blende-type crystal structure like that of the GaSb semiconductors, whose intrinsic ferromagnetism is confirmed by magnetic circular dichroism (MCD) spectroscopy measurement [12, 13]. The transition metal (Fe) dopant ions may replace the III atoms (Ga) in GaSb host semiconductor and contribute to magnetic spin or they can occupy interstitial sites and act as defects, i.e., they can act as substitutional as well as interstitial impurity [5, 60, 61, 62].

In the cited experimental works, (Ga,Fe)Sb layers was grown by low-temperature molecular

beam epitaxy (LT-MBE) and the scanning transmission electron microscopy (STEM) lattice image indicates that the crystal structure of the (Ga,Fe)Sb layer maintain the zinc-blende crystal structure of the host semiconductor. Moreover, the magneto-optical properties of the (Ga,Fe)Sb thin films was also investigated by magnetic circular dichroism (MCD) spectroscopy in a reflection configuration [12] and the result indicates that the band structure of the heavily Fe-doped (Ga,Fe)Sb samples is of zinc-blende type and is consistent with the crystal structure observed in the STEM image.

It was also shown that T_c of (Ga,Fe)Sb followed the relation $T_c = Cxp^{1/3}$ as expected in a carrier-induced FMS. Remarkably, T_c of $(Ga_{1-x}Fe_x)Sb$ keeps increasing as Fe impurity concentration x increases and reaches 230 K at $x = 20\%$, as shown in Fig. 2.11, which is the highest T_c value reported in (Ga,Fe)Sb FMSs so far [12] with no observed saturation of T_c with increasing x. Moreover, by extrapolating the T_c vs x trend in Fig. 2.11, the researchers also illustrated that even higher T_c, reaches above room temperature, can be realized by further increasing x: (300 K) at $x = 23\%$ and 340 K at $x = 25\%$.

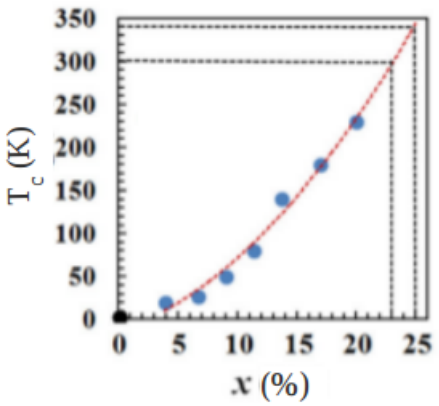

Figure 2.11: Curie temperature T_c vs Fe concentration x of $(Ga_{1-x}Fe_x)Sb$ [12].

In order to characterize the magnetic properties in more details, they also analyzed MCD intensity vs magnetic field (MCD vs H) characteristics measured at different photon energies. In Fig. 2.12, the clear hysteresis curves observed at all the photon energies demonstrate the presence of ferromagnetism in heavily Fe-doped (Ga,Sb) thin films is intrinsic and originates from the zinc-blende (Ga,Fe)Sb.

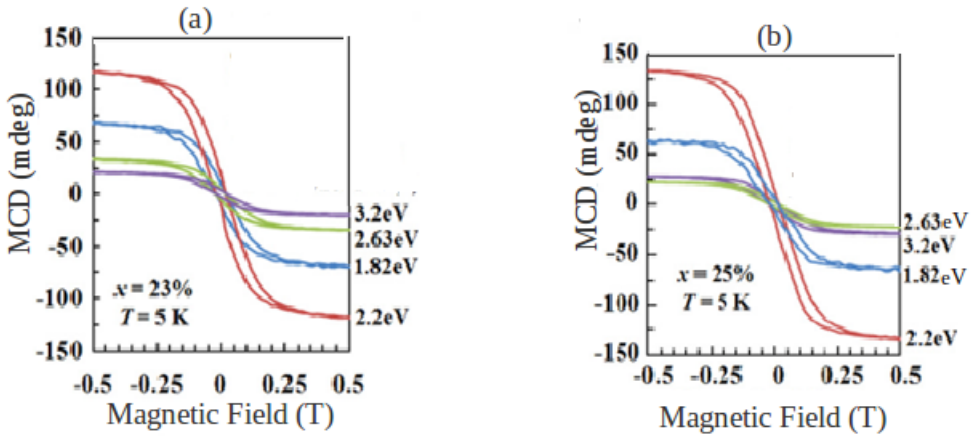

Figure 2.12: MCD vs magnetic fieldes characteristics measured at various photon energies (1.82, 2.2, 2.63, and 3.2 eV) at 5 K with (a) $x = 23\%$ and (b) with $x = 25\%$ [13].

The T_c vs x relation (see Fig 2.11), implying that ferromagnetism of $(Ga_{1-x}Fe_x)Sb$ with $x = 23\%$ and $x = 25\%$ has the same trend and origin as those of with lower Fe concentrations ($x \leq 20\%$) and the obtained result indicates that (Ga,Fe)Sb is a promising FMS material which may be used for semiconductor spintronics devices operating at room temperature.

Chapter 3

Effects of Magnetic Field, Electric Field and Anisotropic Energy on the Magnetic Properties of Fe Alloyed GaSb DMS

3.1 Introduction

Room temperature functionality of III-V elements based spintronic devices has not yet been realized due to insufficient feromagnetic transition temperature. However, recently, a number of experimental works have shown the appearance of a ferromagnetic ordering in III-V semiconductor hosts heavily doped with Fe atoms, in particular, (In,Fe)As [8, 14], (Ga,Fe)Sb [12, 13], and (Al,Fe)Sb [12].

Accordingly, up to 25% sizeable amount of Fe impurity relative to the Ga content could be introduced into GaSb semiconductor host without the formation of second-phase. (Ga,Fe)Sb thin film layers prepared by Molecular Beam Epitaxy (MBE) demonstrated ferromagnetic property up to a temperature of 340 K [13] and hence, entail further analysis using different techniques as well.

In this Chapter, starting with a Kondo lattice model type Hamiltonian, the effects of in-

creasing impurity concentration x and/or magnetic field, electric field, and magnetic anisotropic energy on the magnetic properties of $Ga/FeSb$ diluted magnetic semiconductor are studied using a model Hamiltonian to obtain magnon dispersion relation, magnetization, and critical temperature of the system.

3.2 Determination of Magnon Energy and Dispersion Relation in DMS

The low-lying energy states of spin systems coupled by exchange interactions are wave-like (see Fig. 3.1), as shown originally by Bloch for ferromagnets. The waves are called spin waves; the energy of a spin wave is quantized, and the unit of energy of a spin wave is called a magnon [27].

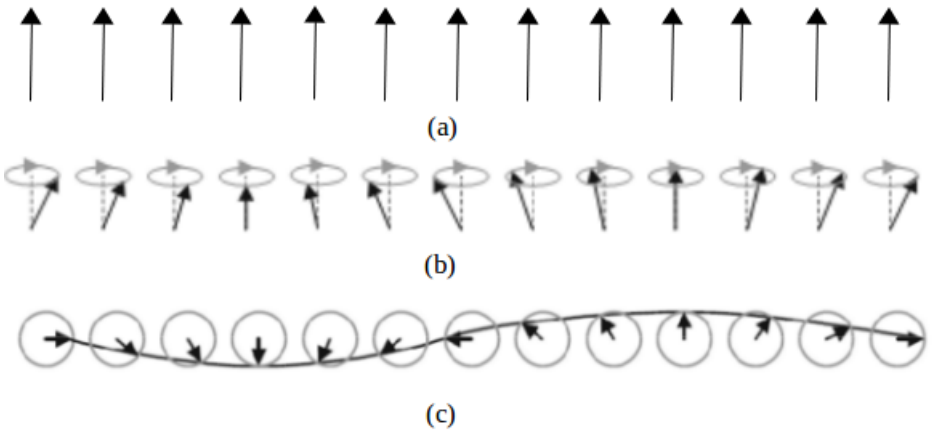

Figure 3.1: Schematic representations of the orientations in a row of spins in (a) the ferromagnetic ground state (b) a spin wave state (the low-lying elementary excitations are spin waves). The ends of the spin vectors precess on the surface of cones, with successive spins advanced in phase by a constant angle, and (c) the spins viewed from top showing one wavelength. The wave is drawn through the ends of the spin vectors [63].

The low energy excitations of ferromagnetic DMS are more complicated wave-like form, with only slight directional changes between neighboring magnetic moments. A model Hamiltonian which has proved useful in understanding the properties of spin wave in ferromagnetic diluted magnetic semiconductor is the Heisenberg Hamiltonian. Accordingly, the model Hamiltonian

used to describe the system is given by

$$\hat{H} = -\sum_{i,j} J_{ij}\mathbf{S}_i \cdot \mathbf{S}_j - g\mu_B \mathbf{B}\sum_i \mathbf{S}_i^z - \mu_e \mathbf{E}\sum_j \mathbf{S}_j^z + D\sum_i (\mathbf{S}_i^z)^2. \tag{3.2.1}$$

The first term $\sum_{i,j} J_{ij}\mathbf{S}_i \cdot \mathbf{S}_j$ is Heisenberg type Hamiltonian describing spin-spin interaction of the Fe^{+3} localized spin. J_{ij} is the exchange coupling energy between the localized spins S_i and S_j that runs over sites i and j which is positive for ferromagnetic ordering. The second term, $g\mu_B \mathbf{B}\sum_i \mathbf{S}_i^z$, gives the Zeemann energy that arises when magnetic field (MF) $\mathbf{B}$ has been applied, where g is the degeneracy factor (or gyromagnetic ratio) and μ_B is the Bohr magneton. The third term, $\mu_e \mathbf{E}\sum_j \mathbf{S}_j^z$, and the fourth term, $D\sum_i \mathbf{S}_i^{z^2}$, arise from the interaction of the localized moments with the applied electric field (EF) $\mathbf{E}$ and the magnetic anisotropic energy (MAE) D, respectively, where μ_e is the electric dipole moment.

For the two sites i and j, $\mathbf{S}_i = S_{ix}\hat{e}_x + S_{iy}\hat{e}_y + S_{iz}\hat{e}_z$ and $\mathbf{S}_j = S_{jx}\hat{e}_x + S_{jy}\hat{e}_y + S_{jz}\hat{e}_z$. Using the dot product of two vectors, i.e., $\mathbf{A} \cdot \mathbf{B} = A_x B_x + A_y B_y + A_z B_z$, we obtain

$$\mathbf{S}_i \cdot \mathbf{S}_j = S_{ix}S_{jx} + S_{iy}S_{jy} + S_{iz}S_{jz}. \tag{3.2.2}$$

Using the spin raising and lowering operators, $S^+ = S_x + iS_y$ and $S^- = S_x - iS_y$, respectively

$$\begin{aligned} S_x &= \frac{1}{2}(S^+ + S^-), \\ S_y &= \frac{-i}{2}(S^+ - S^-). \end{aligned} \tag{3.2.3}$$

Substituting Eq. (3.2.3) into Eq. (3.2.2), we get

$$\begin{aligned} \mathbf{S}_i \cdot \mathbf{S}_j &= \Big[\frac{1}{2}(S_i^+ + S_i^-) \times \frac{1}{2}(S_J^+ + S_j^-)\Big] + \Big[\frac{-i}{2}(S_i^+ - S_i^-) \times \frac{-i}{2}(S_j^+ - S_j^-)\Big] + S_i^z S_j^z \\ &= \frac{1}{4}\Big[(S_i^+ S_j^+) + (S_i^+ S_j^-) + (S_i^- S_j^+) + (S_i^- S_j^-)\Big] \\ &+ \frac{1}{4}[(-S_i^+ S_j^+) + (S_i^+ S_j^-) + (S_i^- S_j^+) + (-S_i^- S_j^-)] + S_i^z S_j^z \\ &= \frac{1}{2}\Big[(S_i^+ S_j^-) + (S_i^- S_j^+)\Big] + S_i^z S_j^z. \end{aligned}$$

Or,

$$\mathbf{S}_i \cdot \mathbf{S}_j = \frac{1}{2}[(S_i^+ S_j^-) + (S_i^- S_j^+)] + S_i^z S_j^z \tag{3.2.4}$$

The spin problem can be converted into a more standard many-body interacting problem by replacing the spins with boson creation and annihilation operators using the Holsten-Primakoff (HP) transformation [66].

Let $\hat{a}_i$ and $\hat{a}_i^\dagger$ be the boson lowering (annihilation) and raising (creation) operators, respectively, for the spin site S_i. They are related to the spin operators by the HP transformation as

$$\begin{aligned} S_i^+ &= \sqrt{2xs(1 - \frac{\hat{n}_i}{2xs})}\hat{a}_i, \\ S_i^- &= \hat{a}_i^\dagger \sqrt{2xs(1 - \frac{\hat{n}_i}{2xs})}, \end{aligned} \tag{3.2.5}$$

where x is the mean number of magnetic ions in the DMS and $\hat{n}_i = \hat{a}_i^\dagger \hat{a}_i$.

A disadvantage of the Holstein-Primakoff transformation is that working explicitly with the Hamiltonian H requires to carry out an expansion. This means that H in principle consists of infinitely many terms. The transformation is thus only reasonable when there is a physical justification for terminating the infinite series. At low temperatures, only a few magnons are excited so that in such cases one can limit only its lowest powers. The simplest approximation in this sense is the so-called spin-wave approximation. Here, we approximate these functions with their power expansions around the state of saturation magnetization as in Eq. (3.2.6). Some important expressions are also included in this equation to complete the algebra in Eq. (3.2.1).

$$\begin{aligned} S_i^+ &= \sqrt{2xs}\ \hat{a}_i; \qquad S_i^- = \sqrt{2xs}\ \hat{a}_i^\dagger; \\ \hat{n}_i &= \hat{a}_i^\dagger \hat{a}_i; \qquad\quad S_i^z = xs - \hat{a}_i^\dagger \hat{a}_i \end{aligned} \tag{3.2.6}$$

Using Eqs. (3.2.5) and (3.2.6) in Eq. (3.2.1), considering nearest neighbors interaction and with

the assumption that $J_{ij} = J$, we obtain

$$\begin{aligned}
\hat{H} &= -J\sum_{i,\delta}\Big[\frac{1}{2}((S_i^+S_{i+\delta}^-)+(S_i^-S_{i+\delta}^+))+S_i^zS_{i+\delta}^z\Big]-2\mu_BB\sum_i\mathbf{S}_i^z \\
&- \mu_eE\sum_{i,\delta}\mathbf{S}_{i+\delta}^z+D\sum_i\mathbf{S}_i^{z^2}. \\
&= -J\sum_{i,\delta}\Big[\frac{1}{2}((\sqrt{2xs}\hat{a}_i)(\sqrt{2xs}\hat{a}_{i+\delta}^\dagger)+(\sqrt{2xs}\hat{a}_i^\dagger)(\sqrt{2xs}\hat{a}_{i+\delta}))+S_i^zS_{i+\delta}^z\Big] \\
&- 2\mu_BB\sum_i(xs-\hat{a}_i^\dagger\hat{a}_i)-\mu_eE\sum_{i,\delta}(xs-\hat{a}_{i+\delta}^\dagger\hat{a}_{i+\delta})+D\sum_i(xs-\hat{a}_i^\dagger\hat{a}_i)^2. \\
&= -J\sum_{i,\delta}\Big[xs(\hat{a}_i\hat{a}_{i+\delta}^\dagger+\hat{a}_i^\dagger\hat{a}_{i+\delta})+(x^2s^2-xs(\hat{a}_{i+\delta}^\dagger\hat{a}_{i+\delta}+\hat{a}_i^\dagger\hat{a}_i)+\hat{a}_i^\dagger\hat{a}_i\hat{a}_{i+\delta}^\dagger\hat{a}_{i+\delta}\Big] \\
&- 2\mu_BB\sum_i(xs-\hat{a}_i^\dagger\hat{a}_i)-\mu_eE\sum_{i,\delta}(xs-\hat{a}_{i+\delta}^\dagger\hat{a}_{i+\delta})+D\sum_i(xs-\hat{a}_i^\dagger\hat{a}_i)^2.
\end{aligned} \tag{3.2.7}$$

We also know that the bosonic commutation relation is given by

$$[\hat{a}_i,\hat{a}_{i+\delta}^\dagger]=\delta_{i,i+\delta}=\begin{cases}0,\ if\ i\neq i+\delta\\ 1,\ if\ i=i+\delta\end{cases} \tag{3.2.8}$$

From Eq. (3.2.8), we obtain

$$\hat{a}_i\hat{a}_{i+\delta}^\dagger-\hat{a}_{i+\delta}^\dagger\hat{a}_i=\delta_{i,i+\delta} \tag{3.2.9}$$

Using Eq. (3.2.9) in Eq. (3.2.7) and rearranging terms, we get

$$\begin{aligned}
\hat{H} &= -Jxs\sum_{i,\delta}\delta_{i,i+\delta}-Jxs\sum_{i,\delta}\hat{a}_{i+\delta}^\dagger\hat{a}_i-Jxs\sum_{i,\delta}\hat{a}_i^\dagger\hat{a}_{i+\delta}-Jx^2\sum_{i,\delta}s^2 \\
&+ Jxs\sum_{i,\delta}\hat{a}_{i+\delta}^\dagger\hat{a}_{i+\delta}+Jxs\sum_i\hat{a}_i^\dagger\hat{a}_i-J\sum_{i,\delta}\hat{a}_i^\dagger\hat{a}_i\hat{a}_{i+\delta}^\dagger\hat{a}_{i+\delta} \\
&- 2\mu_BBx\sum_i s+2\mu_BB\sum_i\hat{a}_i^\dagger\hat{a}_i-\mu_eEx\sum_{i,\delta}s+\mu_eE\sum_{i,\delta}\hat{a}_{i+\delta}^\dagger\hat{a}_{i+\delta}) \\
&+ D^{'}x^2\sum_i s^2-2xsD\sum_i\hat{a}_i^\dagger\hat{a}_i+D\sum_i(\hat{a}_i^\dagger\hat{a}_i)^2.
\end{aligned} \tag{3.2.10}$$

Since the system is periodic (propagates throughout), we are looking for excitation which can be characterized by the well-defined (crystal momentum). So, we define the corresponding Fourier

transformed variables. That is,

$$\begin{aligned} \hat{a}_i &= \tfrac{1}{\sqrt{N}} \textstyle\sum_k \hat{a}_k e^{i\vec{k}\cdot\vec{r}_i}, \\ \hat{a}_i^\dagger &= \tfrac{1}{\sqrt{N}} \textstyle\sum_k \hat{a}_k^\dagger e^{-i\vec{k}\cdot\vec{r}_i}, \end{aligned} \tag{3.2.11}$$

where $\vec{k}$ is the wave vector and N is the total number of atoms in the crystal lattice.

Substituting Eq. (3.2.11) into Eq. (3.2.10), we get

$$\begin{aligned} \hat{H} &= -Jxs\sum_{k,k'}\delta_{k,k'} - Jxs\sum_{i,\delta}(\frac{1}{\sqrt{N}}\sum_{k'}\hat{a}_{k'}^\dagger e^{-i\vec{k'}\cdot(\vec{r}_i+\vec{\delta})})(\frac{1}{\sqrt{N}}\sum_k \hat{a}_k e^{i\vec{k}\cdot\vec{r}_i}) \\ &- Jxs\sum_{i,\delta}(\frac{1}{\sqrt{N}}\sum_k \hat{a}_k^\dagger e^{-i\vec{k}\cdot\vec{r}_i})(\frac{1}{\sqrt{N}}\sum_{k'}\hat{a}_{k'}e^{i\vec{k}\cdot(\vec{r}_i+\vec{\delta})}) - Jx^2\sum_{i,\delta}s^2 \\ &+ Jxs\sum_{i,\delta}(\frac{1}{\sqrt{N}}\sum_{k'}\hat{a}_{k'}^\dagger e^{-i\vec{k'}\cdot(\vec{r}_i+\vec{\delta})})(\frac{1}{\sqrt{N}}\sum_{k''}\hat{a}_{k''}e^{i\vec{k''}\cdot(\vec{r}_i+\vec{\delta})}) \\ &+ Jxs\sum_{i}(\frac{1}{\sqrt{N}}\sum_k \hat{a}_k^\dagger e^{-i\vec{k}\cdot\vec{r}_i})(\frac{1}{\sqrt{N}}\sum_{k'}\hat{a}_{k'}e^{i\vec{k'}\cdot\vec{r}_i}) \\ &-J \sum_{i,\delta}(\frac{1}{\sqrt{N}}\sum_k \hat{a}_k^\dagger e^{-i\vec{k}\cdot\vec{r}_i})(\frac{1}{\sqrt{N}}\sum_{k'}\hat{a}_{k'}e^{i\vec{k'}\cdot\vec{r}_i})(\frac{1}{\sqrt{N}}\sum_{k''}\hat{a}_{k''}^\dagger e^{-i\vec{k''}\cdot(\vec{r}_i+\vec{\delta})}) \\ &\quad (\frac{1}{\sqrt{N}}\sum_{k'''}\hat{a}_{k'''}e^{i\vec{k'''}\cdot(\vec{r}_i+\vec{\delta})}) \\ &- 2\mu_B Bx\sum_i s + 2\mu_B B\sum_i(\frac{1}{\sqrt{N}}\sum_k \hat{a}_k^\dagger e^{-i\vec{k}\vec{r}_i})(\frac{1}{\sqrt{N}}\sum_{k'}\hat{a}_{k'}e^{i\vec{k'}\vec{r}_i}) \\ &- \mu_e Ex\sum_{i,\delta}s + \mu_e E\sum_{i,\delta}(\frac{1}{\sqrt{N}}\sum_{k'}\hat{a}_{k'}^\dagger e^{-i\vec{k'}\cdot(\vec{r}_i+\vec{\delta})})(\frac{1}{\sqrt{N}}\sum_{k''}\hat{a}_{k''}e^{i\vec{k''}\cdot(\vec{r}_i+\vec{\delta})}) \\ &+ Dx^2\sum_i s^2 - 2xsD\sum_i(\frac{1}{\sqrt{N}}\sum_k \hat{a}_k^\dagger e^{-i\vec{k}\cdot\vec{r}_i})(\frac{1}{\sqrt{N}}\sum_{k'}\hat{a}_{k'}e^{i\vec{k'}\cdot\vec{r}_i}) \\ &+ D\sum_i((\frac{1}{\sqrt{N}}\sum_k \hat{a}_k^\dagger e^{-i\vec{k}\cdot\vec{r}_i})(\frac{1}{\sqrt{N}}\sum_{k'}\hat{a}_{k'}e^{i\vec{k'}\cdot\vec{r}_i}))^2. \end{aligned} \tag{3.2.12}$$

Equation (3.2.12), can then be simplified as

$$\begin{aligned}
\hat{H} &= -Jxs\sum_{k,k'}\delta_{k,k'} - \frac{Jxs}{N}\sum_{i,\delta,k,k'}\hat{a}^{\dagger}_{k'}\hat{a}_k e^{i(\vec{k}-\vec{k'})\cdot\vec{r}_i}e^{-i\vec{k'}\cdot\vec{\delta}} \\
&- \frac{Jxs}{N}\sum_{i,\delta,k,k'}\hat{a}^{\dagger}_{k}\hat{a}_{k'}e^{i(\vec{k'}-\vec{k})\cdot\vec{r}_i}e^{i\vec{k}\cdot\vec{\delta}} - Jx^2\sum_i s^2 \\
&+ \frac{Jxs}{N}\sum_{i,\delta,k,k'}\hat{a}^{\dagger}_{k'}\hat{a}_{k''}e^{i(\vec{k''}-\vec{k'})\cdot\vec{r}_i})e^{i(\vec{k''}-\vec{k'})\cdot\vec{\delta}} + \frac{Jxs}{N}\sum_{i,k,k'}\hat{a}^{\dagger}_{k}\hat{a}_{k'}e^{i(\vec{k'}-\vec{k})\cdot\vec{r}_i} \\
&- \frac{J}{N^2}\sum_{i,\delta,k,k',k'',k'''}\hat{a^{+}}_{k}\hat{a}_{k'}e^{i(\vec{k'}-\vec{k})\cdot\vec{r}_i}\hat{a}^{\dagger}_{k''}\hat{a}_{k'''}e^{i(\vec{k'''}-\vec{k''})\cdot\vec{r}_i}e^{i(\vec{k'''}-\vec{k''})\cdot\vec{\delta}} - 2\mu_B Bx\sum_i s \\
&+ \frac{2\mu_B B}{N}\sum_{i,k,k'}\hat{a}^{\dagger}_{k}\hat{a}_{k'}e^{i(\vec{k'}-\vec{k})\cdot\vec{r}_i} - \mu_e Ex\sum_i s + \frac{\mu_e E}{N}\sum_{i,\delta,k,k'}\hat{a}^{\dagger}_{k}\hat{a}_{k'}e^{i(\vec{k'}-\vec{k})\cdot\vec{r}_i}e^{i(\vec{k'}-\vec{k})\cdot\vec{\delta}} \\
&+ Dx^2\sum_i s^2 - \frac{2xsD}{N}\sum_{i,\delta,k,k'}\hat{a}^{\dagger}_{k}\hat{a}_{k'}e^{i(\vec{k'}-\vec{k})\cdot\vec{r}_i} + \frac{D}{N}(\sum_{i,k,k'}\hat{a}^{\dagger}_{k}\hat{a}_{k'}e^{i(\vec{k'}-\vec{k})\cdot\vec{r}_i})^2.
\end{aligned} \tag{3.2.13}$$

We also know that

$$\frac{1}{\sqrt{N}}\sum_i e^{i(\vec{k}-\vec{k'})\cdot\vec{r}_i} = \delta(\vec{k}-\vec{k'}). \tag{3.2.14}$$

Putting Eq. (3.2.14) in Eq. (3.2.13), we obtain

$$\begin{aligned}
\hat{H} &= -Jxs\sum_{k,k'}\delta_{k,k'} - Jxs\sum_{\delta,k,k'}\hat{a}^{\dagger}_{k'}\hat{a}_k\delta(\vec{k}-\vec{k'})e^{-i\vec{k'}\cdot\ \vec{\delta}} - Jxs\sum_{\delta,k,k'}\hat{a}^{\dagger}_{k}\hat{a}_{k'}e^{i\vec{k}\cdot\vec{\delta}} \\
&- Jx^2\sum_i s^2 + Jxs\sum_{\delta,k,k'}\hat{a}^{\dagger}_{k'}\hat{a}_{k''}\delta(\vec{k''}-\vec{k'})e^{i(\vec{k''}-\vec{k'})\cdot\vec{\delta}} + Jxs\sum_{k,k'}\hat{a}^{\dagger}_{k}\hat{a}_{k'} \\
&- J\sum_{k,k'}\hat{a}^{\dagger}_{k}\hat{a}^{\dagger}_{k'}\hat{a}^{\dagger}_{k''}\hat{a}_{k'''}e^{i(\vec{k'''}-\vec{k''})\cdot\vec{\delta}} - 2\mu_B Bx\sum_i s + 2\mu_B B\sum_{k,k'}\hat{a}^{\dagger}_{k}\hat{a}_{k'} \\
&- \mu_e Ex\sum_i s + \mu_e E\sum_{\delta,k,k'}\hat{a}^{\dagger}_{k}\hat{a}_{k'}e^{i(\vec{k'}-\vec{k})\cdot\vec{\delta}}Dx^2\sum_i s^2 \\
&- 2xsD\sum_{k,k'}\hat{a}^{\dagger}_{k}\hat{a}_{k'} + D\sum_{k,k'}(\hat{a}^{\dagger}_{k}\hat{a}_{k'})^2e^{i(\vec{k'}-\vec{k})\cdot\vec{r}_i}.
\end{aligned} \tag{3.2.15}$$

Assuming $\sum_k = \sum_{k'}$ and also $k = k' = k'' = k'''$, Eq. (3.2.15) can be written as

$$\begin{aligned}
\hat{H} &= -Jxs - Jxs\sum_{\delta,k}\hat{n}_k e^{i\vec{k}\cdot\vec{\delta}} - Jxs\sum_{\delta,k}\hat{n}_k e^{-i\vec{k}\cdot\vec{\delta}} - Jx^2\sum_i s^2 + Jxs\sum_k \hat{n}_k \\
&+ Jxs\sum_k \hat{n}_k - J\sum_k(\hat{n}_k)^2 - 2\mu_B Bx\sum_i s + 2\mu_B B\sum_k \hat{n}_k - \mu_e Ex\sum_i s \\
&+ \mu_e E\sum_k \hat{n}_k + Dx^2\sum_i s^2 - 2xsD\sum_k \hat{n}_k + D\sum_k(\hat{n}_k)^2, \\
&= -Jxs - 2Jxs\sum_{\delta,k}\hat{n}_k e^{i\vec{k}\cdot\vec{\delta}} - NJx^2s^2 + 2Jxs\sum_k \hat{n}_k - J\sum_k(\hat{n}_k)^2 - 2N\mu_B Bxs \\
&+ 2\mu_B B\sum_k \hat{n}_k - N\mu_e Exs + \mu_e E\sum_k \hat{n}_k + NDx^2s^2 - 2xsD\sum_k \hat{n}_k + D\sum_k(\hat{n}_k)^2,
\end{aligned}$$

Or,

$$\begin{aligned}
\hat{H} &= -2Jxs\sum_{\delta,k}\hat{n}_k e^{i\vec{k}\cdot\vec{\delta}} - (J + 2N\mu_B\mathbf{B} + N\mu_e\mathbf{E})xs + N(D-J)x^2s^2 \\
&+ (2Jxs + 2\mu_B\mathbf{B} + \mu_e\mathbf{E} - 2sD)\sum_k \hat{n}_k + (D-J)\sum_k(\hat{n}_k)^2, \qquad (3.2.16)
\end{aligned}$$

where $\hat{n}_k = \hat{a}_k^\dagger \hat{a}_k$.

For one dimensional system, with z number of nearest neighbors, the following identity holds:

$$\tfrac{1}{z}\textstyle\sum_\delta e^{i\vec{k}\cdot\vec{\delta}} = \tfrac{1}{z}(e^{ika} + e^{-ika}) = \tfrac{1}{z}(2\cos(ka)). \qquad (3.2.17)$$

Putting Eq. (3.2.17) into Eq. (3.2.16) and for $z = 2$, we get

$$\begin{aligned}
\hat{H} &= -2Jxs\sum_k \hat{n}_k(\cos(ka)) - (J + 2N\mu_B B + N\mu_e E)xs + N(D-J)x^2s^2 \\
&+ (2Jxs + 2\mu_B B + \mu_e E - 2sD)\sum_k \hat{n}_k + (D-J)\sum_k(\hat{n}_k)^2. \qquad (3.2.18)
\end{aligned}$$

For long wave excitation, $(ka \ll 1)$, $cos(ka) \approx 1 - k^2a^2/2$, so that Eq. (3.2.18) can be rewritten

as

$$\begin{aligned}
\hat{H} &= -2Jxs\sum_k \hat{n}_k(1-\frac{k^2a^2}{2}) - (J+2N\mu_B B+N\mu_e E)xs + N(D-J)x^2s^2 \\
&+ (2Jxs+2\mu_B B+\mu_e E-2sD)\sum_k \hat{n}_k + (D-J)\sum_k(\hat{n}_k)^2 \\
&= (Jxsk^2a^2+2\mu_B B+\mu_e E-2sD)\sum_k \hat{n}_k \qquad (3.2.19)\\
&- (J+2N\mu_B B+N\mu_e E)xs + N(D-J)x^2s^2 + (D-J)\sum_k(\hat{n}_k)^2 \\
&= \sum_k \hat{n}_k\omega_k - (J+2N\mu_B B+N\mu_e E)xs + N(D-J)x^2s^2 + (D-J)\sum_k(\hat{n}_k)^2.
\end{aligned}$$

In Eq. (3.2.19), introducing the notation $\hat{H}_0$ so that,

$$\hat{H}_0 = -(J+2N\mu_B B+N\mu_e E)xs + N(D-J)x^2s^2 + (D-J)\sum_k(\hat{n}_k)^2,$$

the magnon energy takes the form

$$\begin{aligned}
\hat{H}_{magnon} &= \hat{H}-\hat{H}_0 \qquad (3.2.20)\\
&= \sum_k \hat{n}_k\omega_k.
\end{aligned}$$

where $\hat{n}_k$ is the number of magnons in state $\mathbf{k}$ and

$$\omega_k = Jxsk^2a^2+2\mu_B B+\mu_e E-2sD, \qquad (3.2.21)$$

is the overall magnon dispersion.

For the purpose of analysis the following parameters are used: (GaFe)Sb has fcc lattice structure and lattice parameter $a = 6.09593\ \mathring{A}$ as a host semiconductor. In Fe^{3+} the 3d electrons would give rise to $s = 5/2$, $\mu_B = 9.2741\times10^{24}\ J/T \approx 0.0579\ meV/T$, $\mu_e \approx 0.08625\ C.m$ and $J \approx 0.1258\ meV$. We also used B, E, and D for different values of the magnitudes of the MF, EF and MAE, respectively.

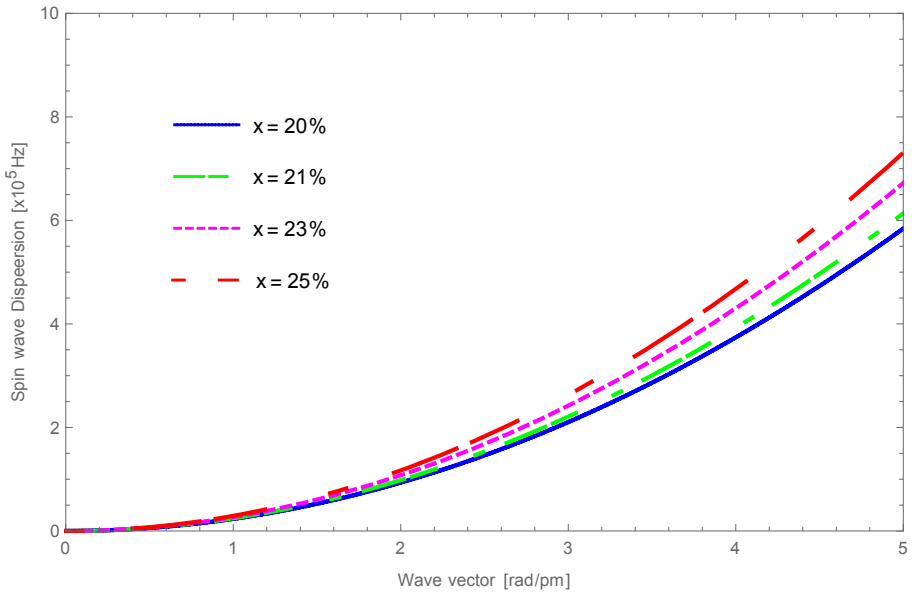

Figure 3.2: The magnon dispersion relation as a function of wave vector for different values of the concentration x with B, E, and D set to zero.

Fig. 3.2 illustrates the increase in the magnon dispersion with an increase in impurity concentration x for a given value of k and quadratic increase in the magnon dispersion with increase in the wave vector k for a fixed value of impurity concentration x with B, E, and D set to zero. No magnon dispersion gap is observed, since zero impurity concentration or no wave vector leads to zero magnon dispersion, which could be clearly verified using Eq. (3.2.21).

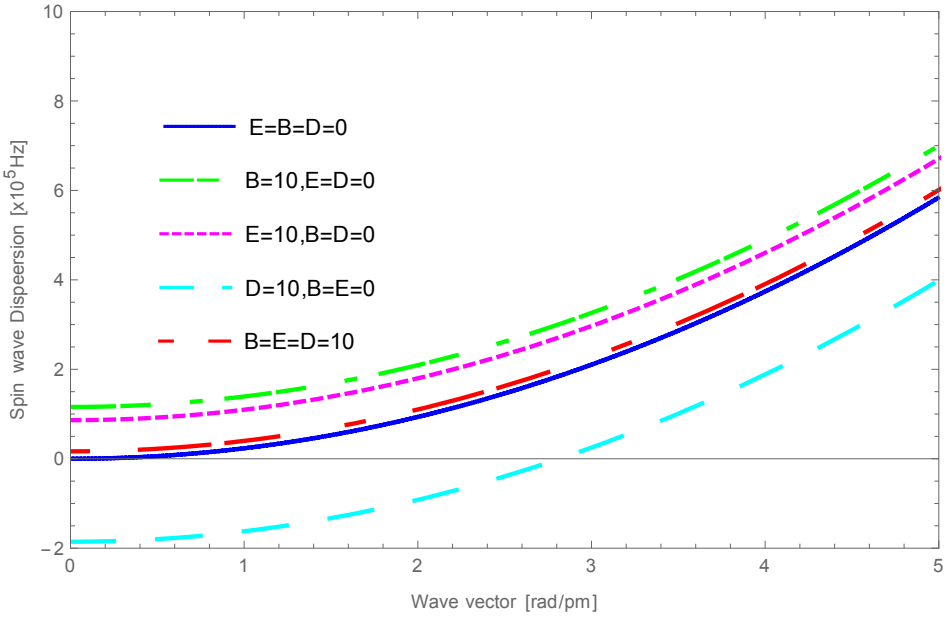

Figure 3.3: The magnon dispersion relation as a function of wave vector with different values of the magnitude of MF, EF, and MAE at a concentration of $x = 20\%$.

In Fig. 3.3, an increase in the gap of the dispersion curve is observed with an increase in the magnitude of magnetic field or electric field and even more when both are applied simultaneously . On the other hand, an increase in the magnitude of the anisotropic energy results in the reduction of the dispersion band gap significantly.

3.3 Magnetization and Ferromagnetic Transition Temperature

At a temperature T, the magnetization per site is given by [78]

$$M(T) = M(0) - g\mu_B \sum_k \hat{n}_k. \tag{3.3.1}$$

The total number of magnons for these systems is described by $\sum_k \hat{n}_k$, where

$$\hat{n}_k \;=\; \frac{1}{e^{\beta\omega_k} - 1}, \tag{3.3.2}$$

in which $\beta \;=\; \frac{1}{k_B T}$ and k_B being the Boltzman's constant.

Introducing the notations $R = Jxsa^2$ and $F = 2\mu_B B + \mu_e E - 2sD$, Eq. (3.2.21) may be rewritten as $\omega_k = Rk^2 \;+\; F$. Substituting ω_k and Eq. (3.3.2) into Eq. (3.3.1), we obtain

$$M(T) = M(0) - g\mu_B \sum_k \frac{1}{e^{\beta(Rk^2+F)} - 1}. \tag{3.3.3}$$

Since the system is expected to resonate in bulk, Eq. (3.3.3) requires integration over the whole system as

$$\begin{aligned} M(T) &= M(0) - \frac{g\mu_B}{(2\pi)^3} \int_0^\infty \frac{k^2}{e^{\beta(Rk^2+F)} - 1} dk \\ &= M(0) - \frac{g\mu_B}{(2\pi)^3} \int_0^\infty \frac{k^2}{ce^{vk^2} - 1} dk, \end{aligned} \tag{3.3.4}$$

where $c = e^{\beta F}$ and $v = \beta R$.

Let $vk^2 = x$. Then $k = (\frac{x}{v})^{\frac{1}{2}}$, $dx = 2vkdk$ and $kdk = \frac{dx}{2v}$. Substituting these values into Eq.

(3.3.4) gives

$$\begin{aligned} M(T) &= M(0) - \frac{g\mu_B}{(2\pi)^3}\int_0^\infty \frac{\left(\frac{x}{v}\right)^{\frac{1}{2}}\left(\frac{dx}{2v}\right)}{ce^x - 1} \\ &= M(0) - \frac{g\mu_B}{(2\pi)^3(2v^{\frac{3}{2}})}\int_0^\infty \frac{x^{\frac{1}{2}}}{ce^x - 1}dx. \end{aligned} \tag{3.3.5}$$

Note that the integral in Eq. (3.3.5) is similar to the Bose-Einstein (BE) function given by

$$B_{\nu-1} = \frac{1}{\Gamma(\nu)}\int_0^\infty \frac{x^{\nu-1}}{\frac{1}{z}e^x - 1}dx, for\ \nu > 1 \tag{3.3.6}$$

For small z ($z \ll 1$), i.e., classical limit $T \gg 0$, we can use the following identity:

$$B_{\nu-1}(z) = \sum_{n=1}^{\infty}\frac{z^n}{n^\nu}. \tag{3.3.7}$$

Combining Eq. (3.3.6) and Eq. (3.3.7), we get

$$\sum_{n=1}^{\infty}\frac{z^n}{n^\nu}\,\Gamma(\nu) = \int_0^\infty \frac{x^{\nu-1}}{\frac{1}{z}e^x - 1}dx. \tag{3.3.8}$$

Using Eq. (3.3.8) in Eq. (3.3.5), with $\nu = \frac{3}{2}$ and $z = \frac{1}{c} = e^{-\beta F}$, results to

$$M(T) = M(0) - \frac{g\mu_B}{2(2\pi)^3 v^{3/2}}\sum_{n=1}^{\infty}\frac{e^{(-\beta F)^n}}{n^{3/2}}\,\Gamma\left(\frac{3}{2}\right). \tag{3.3.9}$$

Assuming that the first term ($n = 1$) is much larger than all other terms and neglecting higher order terms, Eq. (3.3.9) becomes

$$\begin{aligned} M(T) &\approx M(0) - \frac{g\mu_B}{2(2\pi)^3 v^{3/2}}\,[e^{-\beta F}\left(\frac{\sqrt{\pi}}{2}\right)] \\ &\approx M(0) - \frac{g\mu_B}{2(2\pi)^3(\beta R)^{3/2}}\,e^{\beta F}\left(\frac{\sqrt{\pi}}{2}\right) \\ &\approx M(0) - \frac{g\mu_B(k_BT)^{3/2}}{32\pi^{\frac{5}{2}}(Jxsa^2)^{3/2}}\,e^{-\frac{F}{k_BT}}. \end{aligned} \tag{3.3.10}$$

Defining the reduced magnetization as $\frac{M(T)}{M(0)}$ with $M(0) = g\mu_B ns$, the magnetization at absolute zero, where all spins are parallel, with $g = 2S + 1 = 2$ for a system of spin $\frac{1}{2}$ particles, Eq.

(3.3.10) becomes

$$\frac{M(T)}{M(0)} = 1 - \frac{A}{x^{\frac{3}{2}}} T^{\frac{3}{2}}\ e^{-\frac{F}{k_B T}}, \tag{3.3.11}$$

where A is a constant given by

$$A = \frac{1}{32\pi^{5/2} ns} \left(\frac{k_B}{Jsa^2}\right)^{\frac{3}{2}}. \tag{3.3.12}$$

Fig. 3.5 to Fig. 3.8 show the reduced magnetization as a function of temperature for constant and varied values of concentration x and/or applied B, E, and D, where $n = 4/a^3$.

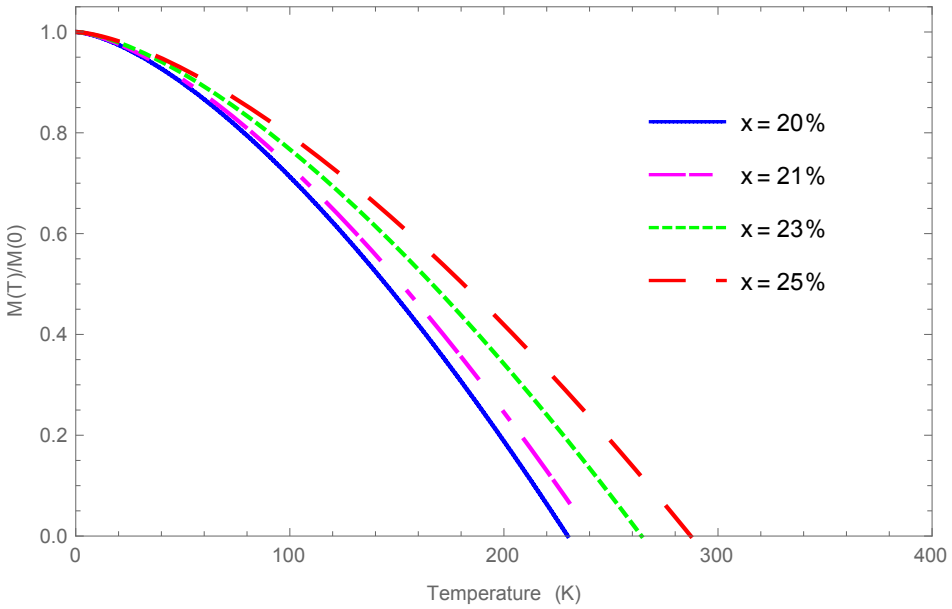

Figure 3.4: The reduced magntization as a function of temperature for different values of x with B, E, and D set to zero.

Fig. 3.4 illustrates an increase in critical temperature with an increase in the magnetic impurity concentration x with B, E and D set to zero. At absolute zero temperature, the figure shows maximum magnetization which is equal to the magnetization at absolute zero of the system. It decays as the temperature increases, becomes zero as the temperature equals the critical temperature, which is in good agreement with the experimental result reported by Tu, et al. [12].

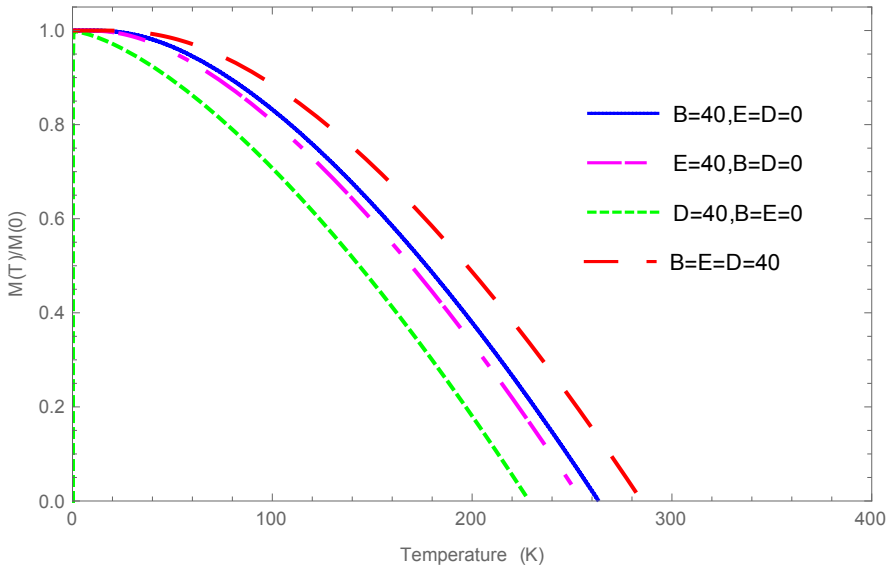

Figure 3.5: The reduced magntization as a function of temperature for different values of B, E, D and B=E=D=40 at a concentration of $x = 20\%$.

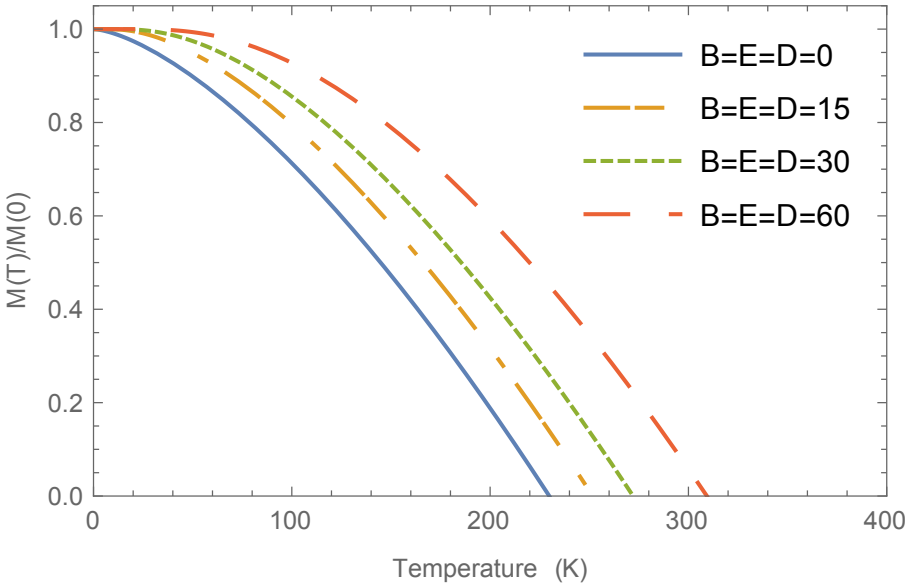

Figure 3.6: The reduced magntization as a function of temperature with the same values of B, E, and D, simultaneously at a concentration of $x = 20\%$.

Fig. 3.5 shows the graph of the reduced magnetization for different values of B, E, and D at a concentration of $x = 20\%$. Note that setting any one of B, E, or D values to 40 while setting the remaining two to zero, the critical temperature, T_c is found to be larger for $B = 40$ (with $E = D = 0$) than that for $E = 40$ (with $B = D = 0$) or $D = 40$ (with $B = E = 0$). It means that the magnetic field B, has a significant effect in increasing T_c followed by E. Moreover, it is seen that setting $B = E = D = 40$ results to a further increase in T_c compared with the previous cases.

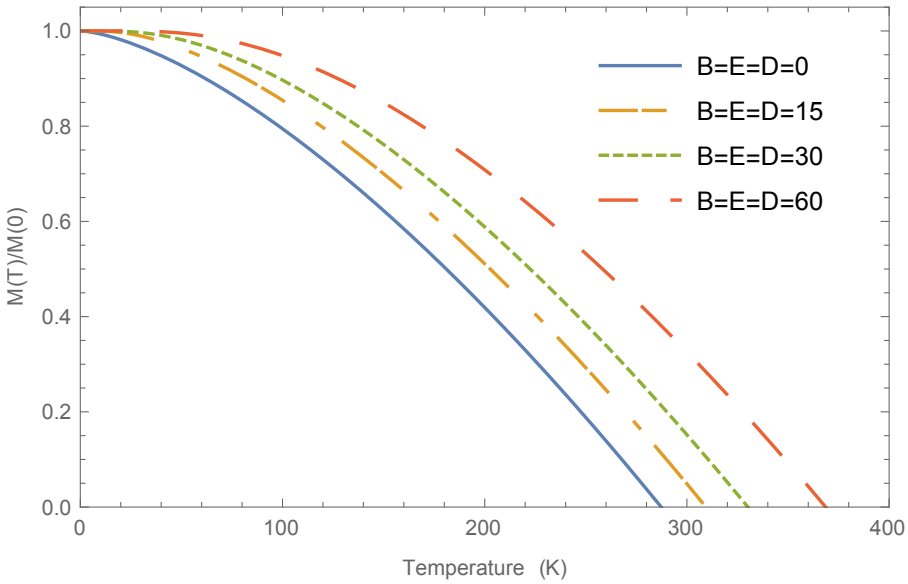

Figure 3.7: The reduced magntization as a function of temperature with the same values of B, E, and D at a concentration of $x = 25\%$.

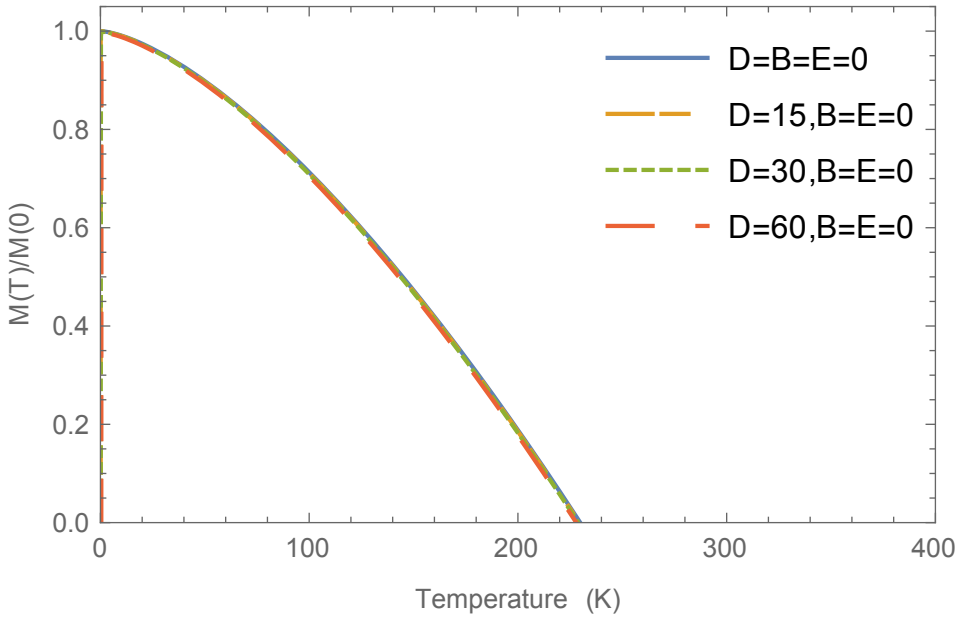

Figure 3.8: The reduced magntization as a function of temperature for different values of D at the concentration $x = 20\%$ with B and E set to zero.

Fig. 3.6 shows the graph of the reduced magnetization for same values of B, E, and D at a concentration of $x = 20\%$. It is seen that setting $B = E = D = 15$ results to an increase in T_c compared with setting $B = E = D = 0$ and setting $B = E = D = 30$ results to an increase in T_c compared with setting $B = E = D = 15$. Moreover, it is seen that setting $B = E = D = 60$ results to a further increase in T_c compared with the previous cases. It means that increasing the combination values has a significant effect in magnetization.

Fig. 3.7 shows a further increase in the critical temperature when all values of B, E, and D are increased at the same time by the same amount at a concentration of $x = 25\%$.

Fig. 3.8 demonstrates the slight reduction in the critical temperature of the system due to the increase in magnetic anisotropy energy at the concentration $x = 20\%$ with B and E set to zero.

All the results show the falling of the magnetization curve to zero as the temperature approaches the ordering temperature T_c. Perhaps, the applied fields increase the coupling between the localized spin and the itinerant holes spins and produces spin polarized carriers which in turn creates molecular field which is responsible for the enhancement of magnetic ordering. The slow drop of the magnetization is due to the low temperature approximation and the rejection of the strong spin fluctuation compared to the Curie-Weiss mean field approximation. These results are also in good agreement with the experimental work of Ohno, et al. [67] and Chiba, et al. [68] that suggested the hole induced ferromagnetism could be turned on and off by the applied fields.

3.4 Conclusion

This section reports the effects of electric field, magnetic field, and magnetic anisotropy energy on the magnetic properties of Fe/GaSb diluted magnetic semiconductor. At all temperatures the magnetization and magnon dispersion are found to be enhanced with an increase in these fields and the percentage of magnetic spin concentration, x, at a time or alternatively. Due to the inclusion of magnetic anisotropy energy, we could identify escalation of the magnon dispersion/band gap energy significantly and a slight reduction of magnetization. Hence, the magnetic critical temperature T_c can be controlled by careful tuning of the electromagnetic field sources and concentration limit in such multiferroics systems. However, once the Fe concentration becomes sufficiently high, there could be considerable overlap of orbitals making the localized electrons mobile/itinerant and overshadowing semiconductivity and/or leading to precipitation and spin glas ordering, as occurs in many DMSs [69] and superconductors [70].

Chapter 4

Specific Heat Capacity and Susceptibility of Fe Alloyed GaSb DMS in the Presence of Applied Electric and Magnetic Fields and Anisotropic Energy

4.1 Introduction

A class of materials known as dilute magnetic semiconductors (DMSs), transition element dopped semiconductor crystals, was developed and studied in the 1980s [3]. Substitution of a transition metal element on a small fraction of impurity concentration x for a host semiconductor element adds local magnetic moments to the systems's low-energy degrees of freedom [1, 71]. The underlying principle behind ferromagnetism in these materials was the interaction between the itinerant electrons in the semiconductor and the atomic magnetic moments of the dopants via an exchange bias mechanism which resulted in spin-polarized carriers in the semiconductor.

Initial work by Ohno and Munekata [1] on Mn doped InAs opened up the technologically significant group III-V semiconductors as potential hosts for DMS applications. This field has

been advancing rapidly ever since. However, the search for better materials and an understanding of the physical mechanisms underlying the magnetism is an ongoing process.

Control of the magnetic phase in DMS is one of the most important processes for magnetic recording and information storage. The use of electric field-controlled magnetization reduces power consumption for storage devices [67, 72]. Electric field control of ferromagnetism was so far demonstrated in a field effect transistor (FET) structure which have been used for non-volatile spin logic devices via carrier-mediated effect [73, 74].

Currently, there has been tremendous upthrust in research activities of GaSb-based systems [12, 13]. This compound has proved to be an interesting material for both basic and applied research for applications in the new branch of technology called spin electronics (spintronics) [75, 76], which employ the spin degree of freedom of electrons in addition to their charge.

The specific heat capacity of ferromagnetic magnons show the characteristic $T^{1.5}$ [77] relation and ferromagnetic susceptibility of a material is quite temperature sennsitive, and above a temperature known as the Curie temperature, the material ceases to become ferromagnetic, and it becomes merely paramagnetic [29].

In this Chapter, the specific heat capacity and susceptibility of $Fe/GaSb$ DMS system is theoretically investigated using the Kondo lattice model type Hamiltonian to explain the influence of applied electric field, magnetic field, and magnetic anisotropic energy.

4.2 The Magnon Specific Heat Capacity

The expression for specific heat, C_{mag}, of the diluted magnetic semiconductor system would be obtained from internal energy, U, of magnons given by

$$U = \sum_{k} \hat{n}_k \omega_k. \tag{4.2.1}$$

We start again with the Hamiltonian of the system used in the preceding Chapter. Hence using the obtained result Eq. (3.3.2), values of β and ω_k into Eq. (4.2.1), we get

$$\begin{aligned} U &= \sum_k \frac{Rk^2+F}{e^{\beta(Rk^2+F)}-1} \\ &= \sum_k \frac{Rk^2}{ce^{\beta(Rk^2)}-1} + \sum_k \frac{F}{ce^{\beta(Rk^2)}-1} \\ &= \sum_k \frac{Rk^2}{ce^{vk^2}-1} + \sum_k \frac{F}{ce^{vk^2}-1} \\ &= \frac{R}{(2\pi)^3}\int_0^\infty \frac{k^4}{ce^{vk^2}-1}dk + \frac{F}{(2\pi)^3}\int_0^\infty \frac{k^2}{ce^{vk^2}-1}dk, \end{aligned} \tag{4.2.2}$$

where $c = e^{\beta F}$, $v = \beta R$ and $\sum_k = \frac{1}{(2\pi)^3}\int_0^\infty k^2 dk$.

Let $vk^2 = x$. Then $k = (x/v)^{1/2}$, $dx = 2vkdk$ and $kdk = dx/(2v)$, putting these values into Eq. (4.2.2) gives

$$\begin{aligned} U &= \frac{R}{(2\pi)^3}\int_0^\infty \frac{(dx/(2v))(x/v)^{3/2}}{ce^x-1}dx + \frac{F}{(2\pi)^3}\int_0^\infty \frac{(dx/(2v))(x/v)^{1/2}}{ce^x-1}dx \\ &= \frac{R}{2(2\pi)^3 v^{\frac{5}{2}}}\int_0^\infty \frac{x^{3/2}}{ce^x-1}dx + \frac{F}{2(2\pi)^3 v^{\frac{3}{2}}}\int_0^\infty \frac{x^{1/2}}{ce^x-1}dx. \end{aligned} \tag{4.2.3}$$

Using $z = \frac{1}{c} = e^{-\beta F}$ and applying Eq. (3.3.8) into Eq. (4.2.3) results

$$\begin{aligned} U &= \frac{R}{2(2\pi)^3 v^{5/2}}\int_0^\infty \frac{x^{((5/2)-1)}}{\frac{1}{z}e^x-1}dx + \frac{F}{2(2\pi)^3 v^{3/2}}\int_0^\infty \frac{x^{((3/2)-1)}}{\frac{1}{z}e^x-1}dx \\ &= \frac{R}{2(2\pi)^3 v^{\frac{5}{2}}}\sum_{n=1}^\infty \frac{e^{(-\beta F)^n}}{n^{5/2}}\ \Gamma(\frac{5}{2}) + \frac{F}{2(2\pi)^3 v^{\frac{3}{2}}}\sum_{n=1}^\infty \frac{e^{(-\beta F)^n}}{n^{3/2}}\ \Gamma(\frac{3}{2}). \end{aligned} \tag{4.2.4}$$

Also assuming the contribution of values for n greater than one is too small over the sum, Eq. (4.2.4) can be approximately writeen as

$$U = \frac{R}{2(2\pi)^3 v^{5/2}} e^{(-\beta F)}(\frac{3\sqrt{\pi}}{4}) + \frac{F}{2(2\pi)^3 v^{3/2}} e^{(-\beta F)}(\frac{\sqrt{\pi}}{2}). \tag{4.2.5}$$

Finally replacing values and rearanging terms Eq. (4.2.5) becomes

$$U = \frac{P}{x^{3/2}}(\frac{3}{2}k_B T^{5/2} e^{\frac{-F}{k_B T}} + FT^{3/2} e^{\frac{-F}{k_B T}}), \tag{4.2.6}$$

where P is a constant given by

$$P = \frac{1}{32\pi^{5/2}} \left(\frac{k_B}{Jsa^2} \right)^{3/2}. \tag{4.2.7}$$

The specific heat is the differential of the internal energy with respect to temperature. That is,

$$\begin{aligned} C_{mag} &= \frac{\partial U}{\partial T} \\ &= \frac{P}{x^{3/2}} \left[(\frac{\partial U}{\partial T} \left(\frac{3}{2} k_B T^{5/2} e^{\frac{-F}{k_B T}} + F T^{3/2} e^{\frac{-F}{k_B T}} \right) \right] \\ &= \frac{P}{x^{3/2}} \Big[\Big[\frac{3}{2} k_B \frac{5}{2} T^{3/2} e^{\frac{-F}{k_B T}} + \frac{3}{2} k_B T^{5/2} e^{\frac{-F}{k_B T}} \left(\frac{F}{k_B T^2} \right) \Big] \\ &+ \Big[\frac{3}{2} F T^{1/2} e^{\frac{-F}{k_B T}} + F T^{3/2} e^{\frac{-F}{k_B T}} \left(\frac{F}{k_B T^2} \right) \Big] \Big] \\ &= \frac{P}{x^{\frac{3}{2}}} \Big[\frac{15}{4} k_B T^{3/2} + \frac{3}{2} k_B T^{5/2} \left(\frac{F}{k_B T^2} \right) + \frac{3}{2} F T^{1/2} + F T^{3/2} \left(\frac{F}{k_B T^2} \right) \Big] e^{\frac{-F}{k_B T}}. \end{aligned} \tag{4.2.8}$$

Eq. (4.2.8) can be rewritten in simplified form as

$$C_{mag} = \frac{P}{x^{3/2}} \Big[\frac{15}{4} k_B T^{3/2} + 3 F T^{1/2} + \frac{F^2}{K_B \sqrt{T}} \Big], \tag{4.2.9}$$

or

$$C_{mag} \approx \frac{P}{x^{3/2}} \Big[0.323 T^{3/2} + 3 F T^{1/2} + 11.6 \frac{F^2}{\sqrt{T}} \Big] e^{\frac{-F}{k_B T}}. \tag{4.2.10}$$

The magnon specific heat capacity of diluted magnetic semiconductor Fe/GaSb material is explained with the increase in impurity concentration and/or, magnitude of the MF, EF and MAE, as shown in Fig. 4.1 to Fig. 4.5, in which maximum values at $T = 400\ K$ are used for comparison.

Fig. 4.1 shows zero magnon specific heat at a temperature equal to the absolute zero of the system, increases exponentially as the temperature increases and the increase in the magnon specific heat curve with temperature tends to decreases as the magnetic impurity concentration x increases with B, E, and D set to zero.

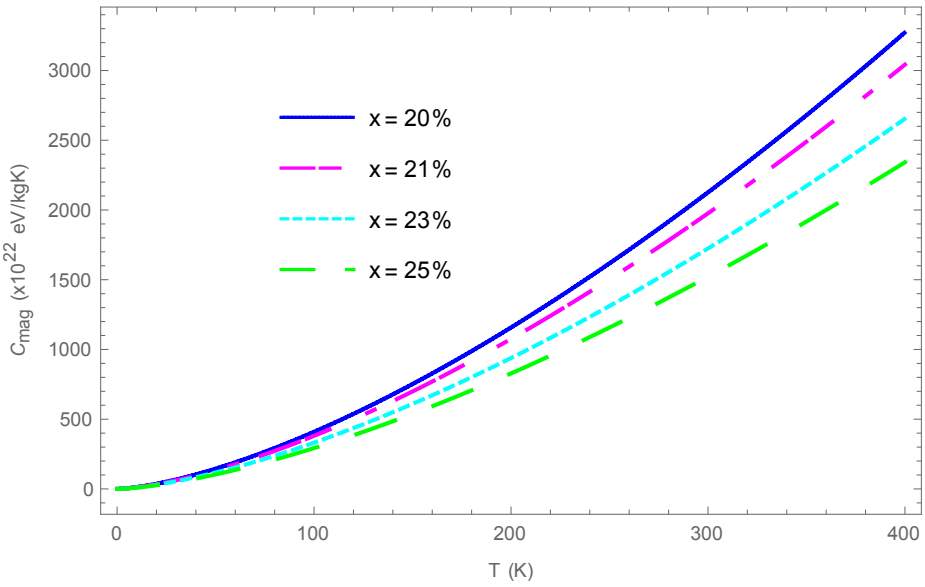

Figure 4.1: Magnon specific heat as a function of temperature for different values of x with B, E, and D set to zero.

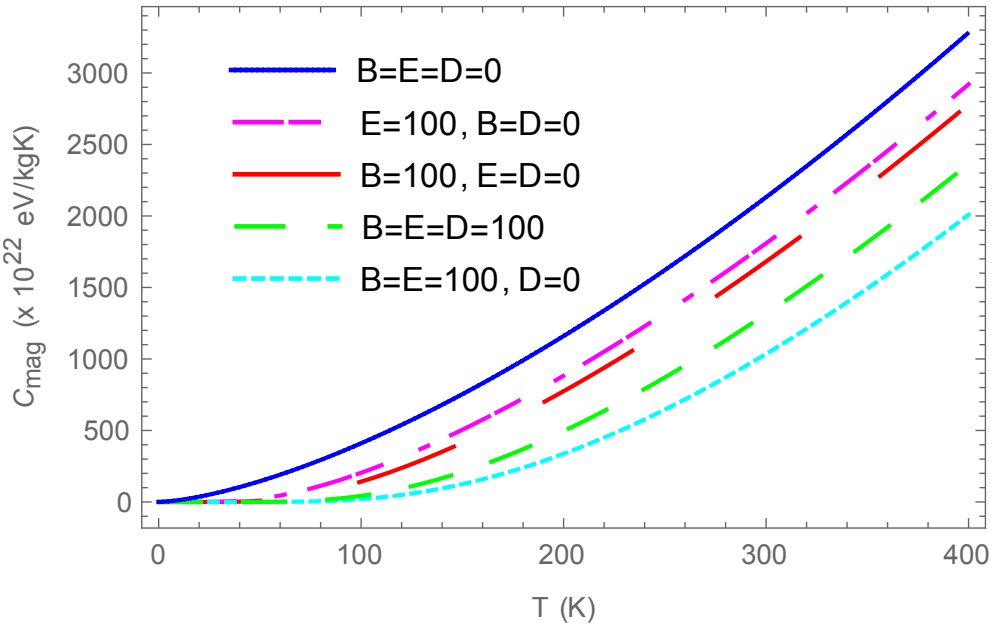

Figure 4.2: Magnon specific heat as a function of temperature with the same values of B, E, D, and all together, successively at a concentration of $x = 20\%$.

Fig. 4.2 illustrates the difference in the exponential increase of the magnon specific heat capacity with only B, when E and D set to zero; with only E, when B and D set to zero; with only D, when E and B set to zero; and with a combination as the temperature increases. Further reduction of specific heat capacity increase is observed with the temperature when both the magnitude of the MF and EF are turned on compared to that shown to the individual results at concentration $x = 20\%$.

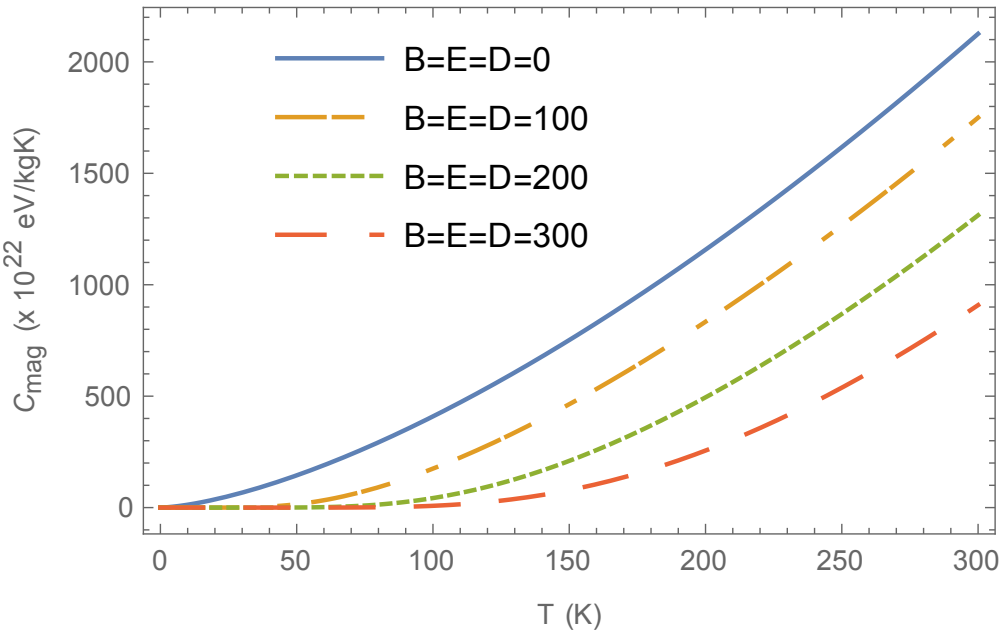

Figure 4.3: Magnon specific heat as a function of temperature with the same values of B, E and D simultaneously at a concentration $x = 20\%$.

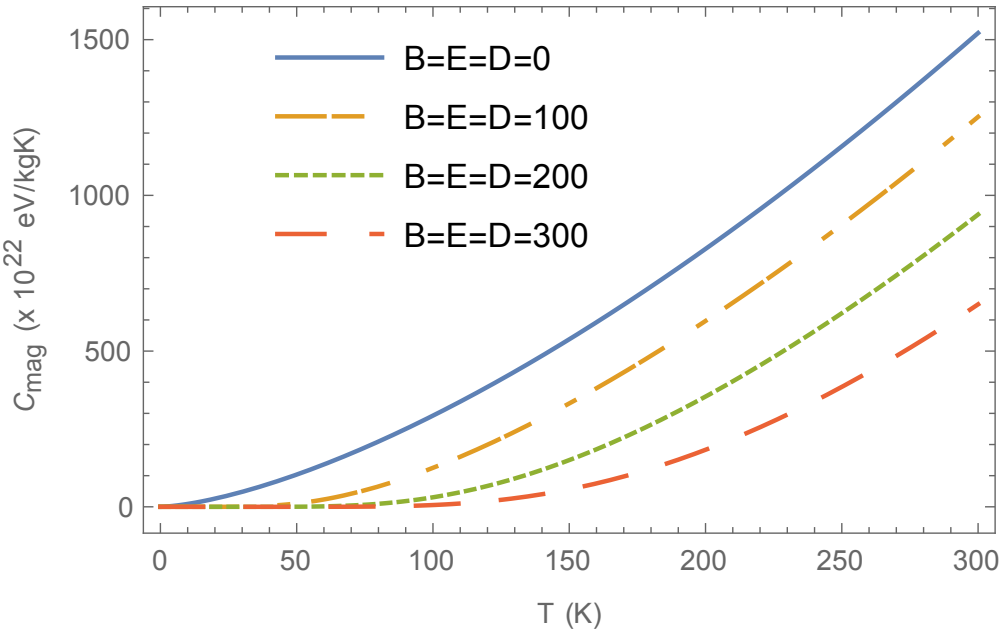

Figure 4.4: Magnon specific heat as a function of temperature with the same values of B, E, and D simultaneously at a concentration of $x = 25\%$.

Fig. 4.3 shows how the exponential increase in the specific heat capacity decresas as the temperature increases with the increase in both values of B and E at the same time by the same amount at a concentration of $x = 20\%$ and Fig. 4.4 shows the further decrease in the specific heat curve as the temperature increases when the values of B, E, and E are increased at the same time by the same amount at a concentration of $x = 25\%$.

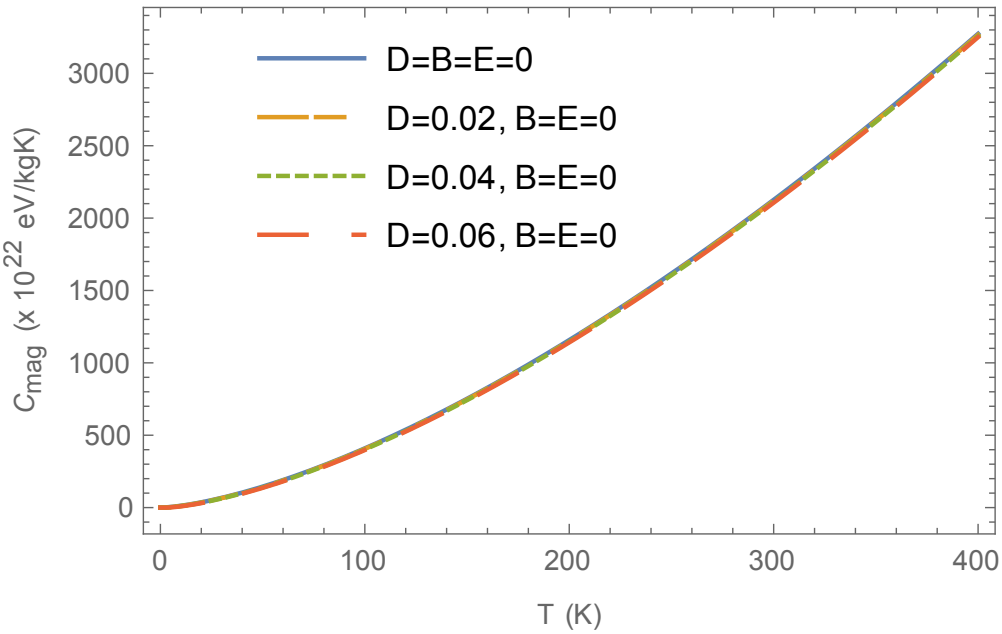

Figure 4.5: Magnon specific heat as a function of temperature for different values of D at the concentration $x = 20\%$ with B and E set to zero.

The increase in the magnon specific heat capacity with temperature tends to decrease as the combination of the applied magnetic and electric fields increase, in agreement with the result obtained by Chernet Amente [78] at lower temperatures for $Ga_{1-x}Mn_xAs$ diluted magnetic semiconductor ferromagnetism and by Twardowski, et al. [79] for the case of $Zn_{1-x}Fe_xS$ DMS; and further decrease when both MF and EF are tuned on along with the increase in the impurity concentration.

However, the inclusion of magnetic anisotropic energy into the basic Hamiltonian has resulted in slight increase in magnon specific heat capacity. Fig 4.5 demonstrates the slight increase in the magnon specific heat capacity due to the increase in magnetic anisotropy energy and even faster increase for higher temperature which could be due to the reduction of magnetic ordering.

4.3 The Magnetic Susceptibility

Substituting M(0) and rearranging terms in Eq. (3.3.10) yields

$$\begin{aligned} M(T) &= M(0) - \frac{g\mu_B(k_BT)^{3/2}}{32\pi^{5/2}(Jxs)^{3/2}a^3}\, e^{-\frac{F}{k_BT}} \\ &= M(0) - \frac{Y}{x^{3/2}}T^{\frac{3}{2}}\, e^{-\frac{F}{k_BT}}, \end{aligned} \tag{4.3.1}$$

where Y is a constant given by

$$Y = \frac{g\mu_B (k_B)^{3/2}}{32\pi^{5/2}(Js)^{3/2}a^3}. \tag{4.3.2}$$

Putting the result of Eq. (4.3.2) back into Eq. (4.3.1) and replacing the F values, gives

$$M(T) \approx M(0) - \frac{Y}{x^{3/2}} T^{3/2}\ e^{-(\frac{2\mu_B B + \mu e E - 2sD}{k_B T})}. \tag{4.3.3}$$

The corresponding magnetic susceptibility becomes

$$\begin{aligned} \chi &= \frac{\partial M(T,B)}{\partial B} \\ &\approx \frac{Y}{x^{\frac{3}{2}}} \left(\frac{2\mu_B}{k_B T}\right) T^{\frac{3}{2}}\ e^{-(\frac{F}{k_B T})} \\ &\approx \frac{Q}{x^{\frac{3}{2}}} T^{\frac{1}{2}}\ e^{-(\frac{F}{k_B T})}, \end{aligned} \tag{4.3.4}$$

where Q is another constant given by

$$Q = Y\left(\frac{2\mu_B}{k_B}\right). \tag{4.3.5}$$

Differentiation of Eq. (4.3.4) with respect to temperature shows the susceptibility is a maximum at the Curie temperature. i.e.,

$$\frac{\partial \chi}{\partial T} = \nabla_T \chi \approx \frac{Q}{x^{\frac{3}{2}}} \left[T^{\frac{-1}{2}} + FT^{\frac{-3}{2}}\right]\ e^{-(\frac{F}{k_B T})}. \tag{4.3.6}$$

Fig. 4.6 shows the magnetic susceptibilities as a function of temperature for various values of impurity concentrations, $x = 20\%$, 21%, 23%, and 25% with $B = E$ set to five and D set to zero. As the temperature increases, though the variation is too small, the curve increases until the maximum value x_{max} has been attained at a certain temperature and then decreases with the increase of temperature. The area under the curve for the temperature interval 230 K to the temperature at which the function reaches at its maximum value, which is the susceptibilities of

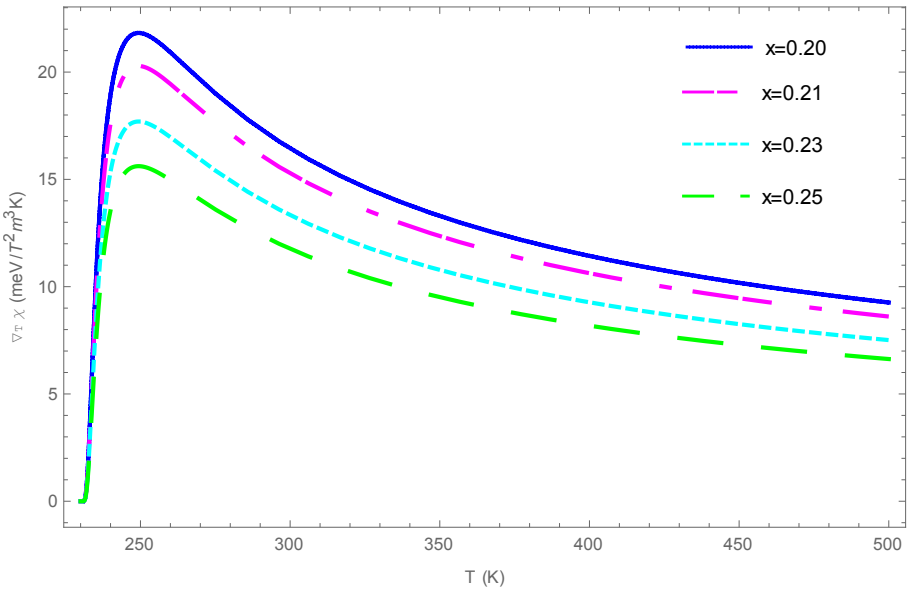

Figure 4.6: Variation of susceptibility with temperature for different values of x with B=E set to five and D set to zero.

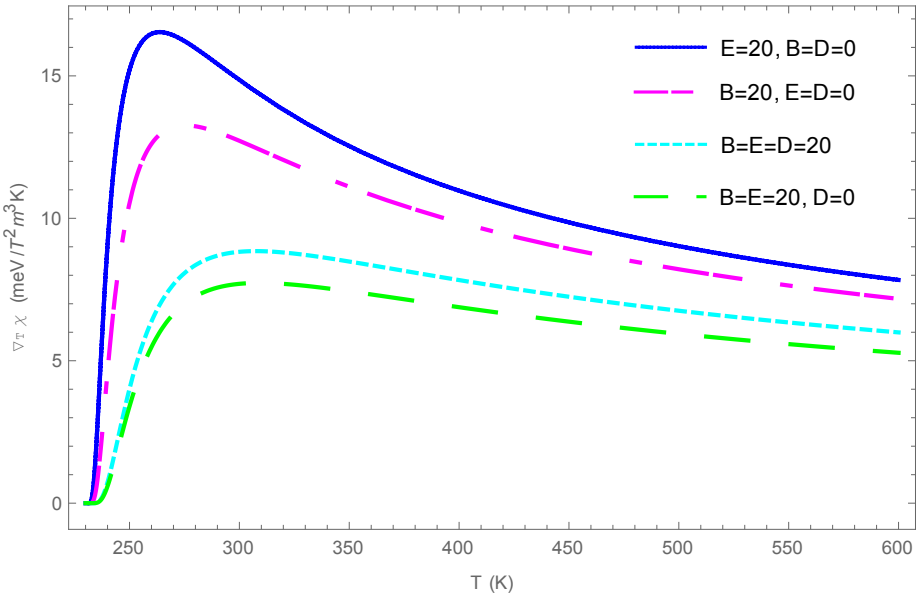

Figure 4.7: Variation of susceptibility with temperature for the same values of $E = 20$, $B = 20$, $B = E = 20$, and $B = E = D = 20$ all together, simultaneously at a concentration $x = 20\%$.

the system, increases as the impurity concentration increases.

Fig. 4.7 compares the increase in the magnetic susceptibilities with values of B, E, B plus E and B plus E plus D, tuned with the same values of B and E, simultaneously at a concentration $x = 20\%$. Similarly, for the four different cases, the function exhibit similar temperature variation and maximum susceptibility as illustrated with the combination of B and E as the temperature increases to the point at which the function reaches at its maximum value.

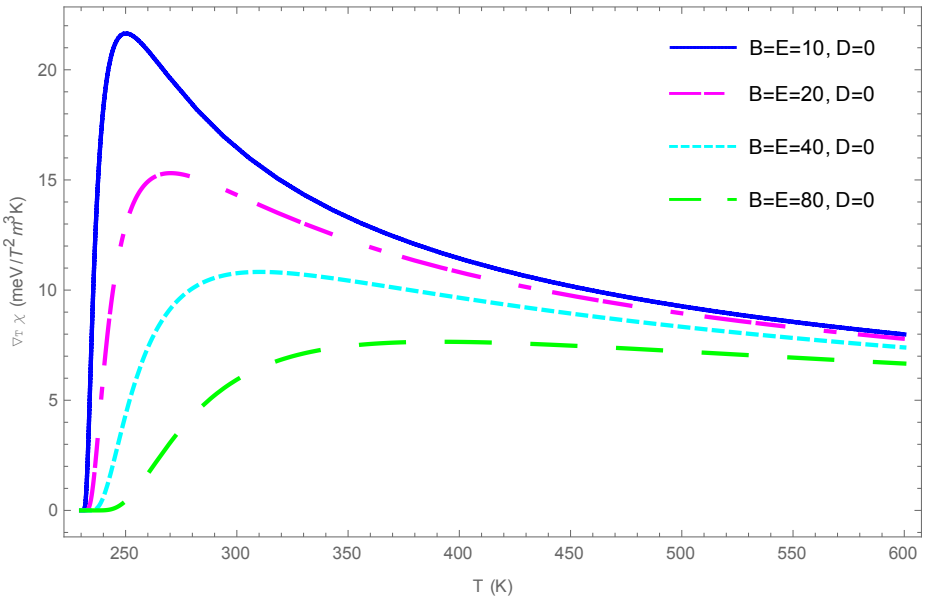

Figure 4.8: Variation of susceptibility with temperature with different values of $B = E$ at a concentration of $x = 20\%$.

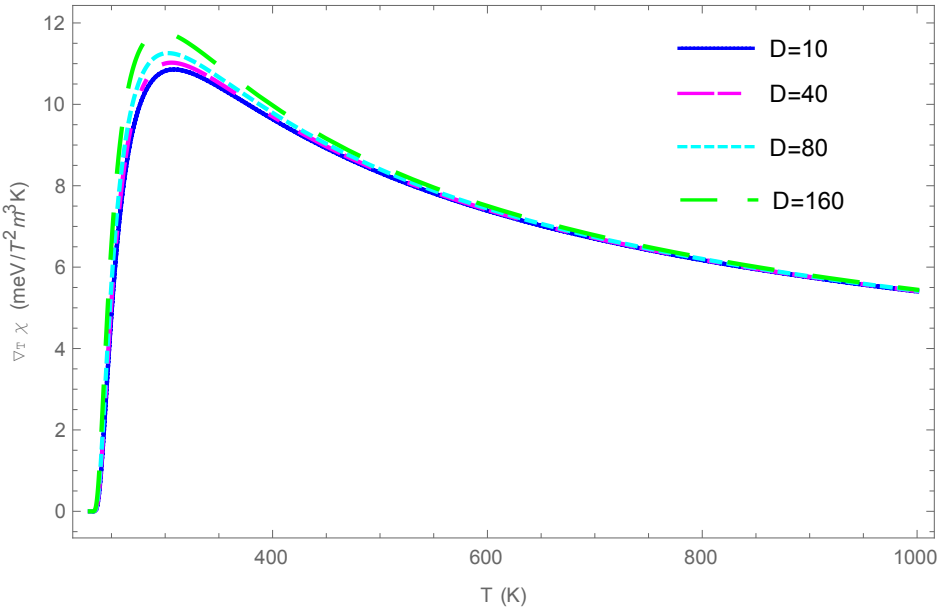

Figure 4.9: Variation of susceptibility with temperature for different values of D at the concentration $x = 20\%$ with B and E set to twenty.

Fig. 4.8 illustrates the increase in the susceptibility of the system as a function of temperature when the values of the combination of B and E increases as the values of B and E increase by the same value at the same time at a concentration of $x = 20\%$ with D set to zero.

Fig. 4.9 illustrate the decrease in the peak of the function, decrease in the susceptibility, as a function of temperature with the increase values of D at the concentration $x = 20\%$ with B and E set to twenty. As the temperature increases, the magnetic susceptibility of the sample increases

until the maximum value has been attained at a certain temperature and then decreases with the increase of temperature. The specific temperature where the function reaches at its maximum for each of the above figures is believed to be transition temperatures. These temperatures are increasing with the increasing of the impurity concentration x and/or with the magnitude of MF, EF alone and even higher with the increase in the combination of both values of B and E, simultaneously. Once the system reaches at this temperature, further increase in the temperature of the system will result to a lose of its ferromagnetic property and hence becomes paramagnetic. However, the increase in the magnetic anisotropic energy results in the decrease of the magnetic susceptibility of the sample until the maximum value is attained at the Curie temperature and then shows similar decreases with the increase of temperature.

4.4 Conclusion

Our results with the applied magnetic field, electric field and magnetic anisotropy energy on the specific heat and susceptibility of ferromagnetic magnons show the characteristic $T^{3/2}$ and $T^{-1/2}$ equivalent dependence that agree with the result obtained in [77] and the Curie-Weiss law in the mean field approximation with Curie constant C for $T > T_c$, respectively. At relatively high temperature, the dispersion relation $\omega_k = Jxsk^2a^2 + 2\mu_B\mathbf{B} + \mu_e\mathbf{E} - 2sD'$ is a good approximation, the specific heat found decreased and the susceptibility enhanced with increase of these fields and percentage of magnetic spin concentration, x at a time or alternatively. Due to the inclusion of the magnetic anisotropy energy, we could identify escalation of magnon specific heat significantly and a slight reduction of susceptibility. Hence, the magnetic specific heat capacity and the magnon susceptibility can be controlled by careful tuning of the electromagnetic field sources and the concentration limit in such multiferroics systems.

Chapter 5

Density Functional Theory

5.1 Introduction

Density functional theory (DFT) is a clever way to solve the Schrödinger equation for a many-body system [80]. It is also called ab-intitio or first principle method, as it is based only on the fundamental laws and constants of quantum mechanics, not on empirical inputs. In the formulation given by Kohn, Hohenberg, and Sham in the 1960's the real system is described by an effective one-body system. In principle, DFT replace the many-body electronic wave function, which is the solution of the Schrödinger equation, with the electronic density $n(\mathbf{r})$ as the basic quantity. The energy is then just a function of this function, i.e., a density functional.

This chapter reviews the general many-body problem with in the Born-Oppenheimer approximation and the theoretical backbones of DFT: the Hohenberg-Kohn theorems and the Kohn-Sham equations. Moreover, brief review of the exchange-correlation functionals, the local density approximation (LDA), and the generalized gradient approximation (GGA) are also introduced. Moreover, the hybrid functional method, the Hubbard correction model, and practical calculations are also briefly discussed.

5.2 The Many-Body Problem

We consider N-electron system (atom, molecule, or solid) in the Born-Oppenheimer and non-relativistic approximations. The electronic Hamiltonian in the position representation is given

by [81]

$$H(r_1, r_2, ..., r_N) = \frac{1}{2}\sum_{i=1}^{N} \nabla_{r_i}^2 + \frac{1}{2}\sum_{i=1}^{N}\sum_{j=1 i\neq j}^{N} \frac{1}{|\mathbf{r}_i - \mathbf{r}_j|} - \sum_{i=1}^{N}\sum_{\alpha} \frac{Z_\alpha}{|\mathbf{r}_i - \mathbf{R}_\alpha|}, \tag{5.2.1}$$

in atomic units. Also, R_α and Z_α are the positions and charges of the nuclei, respectively. The three terms of the Hamiltonian in Eq. (5.2.1) can be denoted as

$$\hat{H} = \hat{T} + \hat{V}_{ee} + \hat{V}_{ne}, \tag{5.2.2}$$

where, $\hat{T}$ is the kinetic energy operator, $\hat{V}_{ee}$ is the electron-electron interaction and $\hat{V}_{ne}$ is the nuclei-electron interaction.

The quantum mechanical many-body problem is described by the following time independent Schrödinger equation:

$$\hat{H}\psi(\mathbf{r}_1, \sigma_1, \mathbf{r}_2, \sigma_2, ..., \mathbf{R}_1, \mathbf{R}_2, ...) = E\psi(\mathbf{r}_1, \sigma_1, \mathbf{r}_2, \sigma_2, ...; \mathbf{R}_1, \mathbf{R}_2...), \tag{5.2.3}$$

where ψ is the many-body wave function which is dpendent on the position and the spin of the electrons, $\mathbf{r_i}$, R_i are the positions of the nuclei, $\mathbf{R_i}$ (with $\mathbf{r_i}$ and $\mathbf{R_i}$ ϵ $\mathbf{\Re^3}$) and $\sigma_i = \uparrow \ or \ \downarrow$ which is antisymmetric with respect to the exchange of two coordinates, and E is the associated energy.

Using Dirac notations, Eq. (5.2.3) can be rewritten in representation independent formalism as

$$\hat{H}|\psi\rangle = E|\psi\rangle. \tag{5.2.4}$$

The quantity of prime interest is the ground-state energy, E_0. The variation theorem establishes that E_0 can be obtained by the following minimization:

$$E_0 = min_\psi \langle\psi|\hat{H}|\psi\rangle, \tag{5.2.5}$$

where the search is over all N-electron antisymmetric wave function, ψ, normalized to unity, i.e.,

$\langle\psi|\psi\rangle = 1$.

The historical predecessor of DFT is the Thomas-Fermi approach dating back to 1927 [82] and its aim is to formulate the quantum mechanical theory in terms of the density instead of the wave function. The electron density, $n(\mathbf{r})$, can be calculated from the electron wave function using the following equation [81]

$$n(\mathbf{r}) = \sum_{i=1}^{N} \int ... \int \psi^*(\mathbf{r}_1, \mathbf{r}_2, ...\mathbf{r}_N)\sigma(\mathbf{r} - \mathbf{r}_i)\psi(\mathbf{r}_1, \mathbf{r}_2, ...\mathbf{r}_N)\mathbf{dr}_1\mathbf{dr}_2...\mathbf{dr}_N, \tag{5.2.6}$$

where N is the number of electrons.

5.2.1 The Universal Density Functional

A functional is a function with another function as a variable and is denoted as $F[f]$. In DFT, the energy is written as a functional of the electron density, $E[n]$. The functional derivative is defined as

$$\frac{\delta}{\delta f(x)}F(f) = lim_{\varepsilon\to 0}\frac{F[f(x) + \varepsilon\delta(x - x')] - F[f(x)]}{\varepsilon}. \tag{5.2.7}$$

Functional derivation include the following important properties;

$$\frac{\delta}{\delta f(x)}\left(\int F[f]dx\right) = \frac{\partial F[f]}{\partial f(x)}, \tag{5.2.8}$$

$$\frac{\delta}{\delta f(x)}\left(\int F[f]f(x)dx\right) = \frac{\partial F[f]}{\partial f(x)}f(x) + F[f(x)] \tag{5.2.9}$$

and

$$\frac{\delta}{\delta f(x)}\left(\frac{1}{2}\int\int g(x, x')f(x)f(x')dxdx'\right) = \int g(x, x')f(x')dx'. \tag{5.2.10}$$

A) Hohenberg-Kohn Theorems

Consider an electron system with an arbitrary external local potential, $v(\mathbf{r})$, in place of $V_{ne}(\mathbf{r})$. A corresponding ground-state wave function ψ (there can be several of them if the ground state is degenerate) can be obtained by solving the Schrödinger equation, from which the associated ground-state density, $n(\mathbf{r})$, can be deduced. Therfore, one has a mapping from the potential, $v(\mathbf{r})$, to the considered ground-state density, $n(\mathbf{r})$, as

$$v(\mathbf{r}) \longrightarrow n(\mathbf{r}). \tag{5.2.11}$$

P. Hohenberg and W. Kohn formulated the two theorems, Hohenberg and Kohn (HK) theorems, in 1964 [88].

The first HK theorem states that

- *For any system of interacting particles an external potential, V_{ext}, is determined uniquely - except for a constant - by the ground state density $n_0(\mathbf{r})$.*

and The second HK theorem states that

- *A universal functional for the energy, E[n], in terms of the density, $n(\mathbf{r})$, can be defined, valid for any external potential, $V_{ext}(\mathbf{r})$. The exact ground-state energy of the system is the global minimum of this functional and the density that minimizes the functional is the exact ground-state density, $n_0(\mathbf{r})$.*

Hohenberg and Kohn showed the mapping in Eq. (5.2.11) can be inverted, i.e., the ground-state density, $n(\mathbf{r})$, determines the potential $v(\mathbf{r})$ up to an arbitrary additive constant, which in turn determines the Hamiltonian and thus everything about the many-body problem. That is,

$$n(\mathbf{r}) \longrightarrow v(\mathbf{r}) + const. \tag{5.2.12}$$

In other words, the potential $v(\mathbf{r})$ is a unique (up to an additive constant) functional of the ground-state density, n_0, and all other properties as well. The ground-state wavefunction, $\psi[n]$, for the potential $v(\mathbf{r})$ is itself a functional of n, which was exploited by Hohenberg and Kohn to

define the universal (i.e., independent from the external potential) density functional, as

$$F[n] = \langle \psi[n] | \hat{T} + \hat{V}_{ee} | \psi[n] \rangle, \tag{5.2.13}$$

which can be used to define the total electronic energy functional expressed as

$$E[n] = F[n] + E_{ext}[n], \tag{5.2.14}$$

with the external energy, $E_{ext}[n]$, for the specific external potential $V_{ne}(\mathbf{r}) = \int \upsilon_{ne}(\mathbf{r}) n(\mathbf{r}) \mathbf{dr}$ of the system considered. Note that for degenerate ground states, $\psi[n]$ is not unique but stands for any degenerate ground-state wave function. However, all $\psi[n]$ gives the same $F[n]$, which is thus a unique functional of n.

Hohenberg and Kohn further showed that the energy functional $E[n]$ satisfies a variational property: the ground-state energy E_0 of the system considered is obtained by minimizing this functional with respect to N-electron densities that are ground-state densities associated with some local potential (refered to as υ-representable densities). That is,

$$E_0[n] = min_n \left\{ F[n] + \int \upsilon_{ne}(\mathbf{r}) n(\mathbf{r}) d\mathbf{r} \right\}, \tag{5.2.15}$$

with the minimum being reached for ground-state density $n_0(\mathbf{r})$ corresponding to the potential $\upsilon_{ne}(\mathbf{r})$.

B) Levy's Constrained-Search Formulation

In 1979 Levy [89, 90] and later Lieb [91], proposed to redefine the universal density functional $F[n]$ using constrained-search formulation to be

$$E_{zero}[n] = min_{\psi \to n} \langle \psi | \hat{T} + \hat{V}_{ee} | \psi \rangle = \langle \psi[n] | \hat{T} + \hat{V}_{ee} | \psi[n] \rangle, \tag{5.2.16}$$

where $\psi \to n$ means that the minimization is done over normalized antisymmetric wave functions ψ which yield the fixed density n via Eq. (5.2.6). For a given density n, the minimizing wave function is denoted by $\psi[n]$ (possibly nonunique in case of degeneracy). This definition

of $F[n]$ is more straight forward than the Hohenberg-Kohn definition. It does not require the existance of local potential associated to density: it is defined on large set of N-electron densities coming from an antisymmetric wave function (referred to as N-representable densities). The variational property of the total electronic energy functional can be eaily demonstrated using the constrained-search formulation. One starts from the usual variational theorem and decomposes the minimization over ψ in two steps: a constrained minimization over ψ giving fixed density n, followed by a minimization over n. That is,

$$\begin{aligned} E_0[n] &= min_{\psi}\langle\psi|\hat{T}+\hat{V}_{ee}+\hat{V}_{ne}|\psi\rangle \\ &= min_n min_{\psi\to n}\langle\psi|\hat{T}+\hat{V}_{ee}+\hat{V}_{ne}|\psi\rangle \\ &= min_n\{min_{\psi\to n}\langle\psi|\hat{T}+\hat{V}_{ee}|\psi\rangle+\int \upsilon_{ne}(\mathbf{r})n(\mathbf{r})d\mathbf{r}\} \\ &= min_n\{F[n]+\int \upsilon_{ne}(\mathbf{r})n(\mathbf{r})d\mathbf{r}\}, \end{aligned} \tag{5.2.17}$$

and again the minimization is reached for ground-state density $n_{zero}(\mathbf{r})$ correspondig to the potential $\upsilon_{ne}(\mathbf{r})$.

The ground-state energy and density can then be in principle obtained by minimizing over the density $n(\mathbf{r})$, i.e., a simple function of three variables, which is a tremendous simplification compared to the minimization over a complicated many-body wave function ψ. However, the explicit expression of $F[n]$ in terms of the density is not known and the direct approximations for $F[n]$ that have been tried so far turn out not to be accurate enough, especially for kinetic energy part $T[n]$ included in $F[n]$:

$$F[n] = T[n] + V_{ee}[n], \tag{5.2.18}$$

where $T[n] = \langle\psi[n]|\hat{T}|\psi[n]\rangle$ and $V_{ee} = \langle\psi[n]|\hat{V}_{ee}|\psi[n]\rangle$

C) The Khon-Sham Method

The HK theorems provide a formal framework to find the ground-state density and the ground state energy of a many-body system. But they do not provide a method to simplify the many-

body problem within DFT. The most widely used method for this purpose has been established by W. Kohn and L. J. Sham [92].

Faced with the difficulty of approximating directly $F[n]$, Kohn and Sham (KS) proposed to decompose $F[n]$ as

$$F[n] = T_s[n] + E_{Hxc}[n], \tag{5.2.19}$$

where $T_s[n]$ is the non-interacting kinetic-energy functional which can be defined with constrained-search formulation

$$T_s[n] = min_{\Phi\to n}\langle\Phi|\hat{T}|\Phi\rangle = \langle\Phi[n]|\hat{T}|\Phi\rangle, \tag{5.2.20}$$

where $\Phi \to n$ means that the minimization is done over normalized *single-determinant wavefunction* Φ which yield the fixed density n. For a given density n, the (not necessary unique) minimizing single-determinant wavefunction is called the KS *wavefunction* and is denoted by $\Phi[n]$. The remaining functional $E_{Hxc}[n]$ in Eq. (5.2.19) is called the Hartree-exchange correlation functional. The idea of the KS method is then to use the exact expression of $T_s[n]$ by reformulating the variational property of $F[n]$ in terms of single-determinant wave function Φ. Thus,

$$\begin{aligned} E_0[n] &= min_n\left\{F[n] + \int \upsilon_{ne}(\mathbf{r})n(\mathbf{r})d\mathbf{r}\right\} \\ &= min_n\left\{min_{\Phi\to n}\langle\Phi|\hat{T}|\Phi\rangle + E_{Hxc}[n] + \int \upsilon_{ne}(\mathbf{r})n(\mathbf{r})d\mathbf{r}\right\} \\ &= min_n min_{\Phi\to n}\left\{\langle\Phi|\hat{T} + \hat{V}_{ne}|\Phi\rangle + E_{Hxc}[n_\Phi]\right\} \\ &= min_n\left\{\langle\Phi|\hat{T} + \hat{V}_{ne}|\Phi\rangle + E_{Hxc}[n_\Phi]\right\}, \end{aligned} \tag{5.2.21}$$

with the minimizing single-determinant KS wave function giving the exact ground-state density $n_0(\mathbf{r})$. Thus, the exact ground-state energy and density can in principle be obtained by minimizing over single determinant wave functions only. Eventhough a wave function has been reintroduced compared to Eq. (5.2.17), it is only a single-determinant wave function Φ and therefore it still represents a tremendous simplification over the usual varitional theorem involv-

ing a multideterminant wave function Ψ. The advantage of Eq. (5.2.21) over Eq. (5.2.17) is that a major part of the kinetic energy can be treated explicitly with the single-determinant wave function Φ, and only $E_{Hxc}[n]$ needs to be approximated as functional of the density.

In practice, $E_{Hxc}[n]$, is written as

$$E_{Hxc}[n] = E_H[n] + E_{xc}[n], \tag{5.2.22}$$

where $E_H[n]$ is the Hartree energy functional given by

$$E_H[n] = \frac{1}{2}\int\int \frac{n(\mathbf{r})n(\mathbf{r}')}{|\mathbf{r}-\mathbf{r}'|} d\mathbf{r} d\mathbf{r}', \tag{5.2.23}$$

representing the classical electrostatic repulsion energy for the charge distribution $n(\mathbf{r})$ with product of the densities $n(\mathbf{r})n(\mathbf{r}')$ corresponds to the case of independent electrons.

$E_{xc}[n]$ is the exchange-correletion energy functional that remains to be approximated. This functional is often decomposed as

$$E_{xc}[n] = E_x[n] + E_c[n], \tag{5.2.24}$$

where $E_x[n]$ is the exchange energy functional defined as

$$E_x[n] = \langle \Phi[n] | \hat{V}_{ee} | \Phi[n] \rangle - E_H[n], \tag{5.2.25}$$

where

$$\langle \Phi[n] | \hat{V}_{ee} | \Phi[n] \rangle = \frac{1}{2}\int\int \frac{n_2(\mathbf{r},\mathbf{r}')}{|\mathbf{r}-\mathbf{r}'|} d\mathbf{r} d\mathbf{r}'.$$

Mirroring the decomposition of the Hartree-exchange-correlation energy performed in the KS method Eq. (5.2.22), the pair density can be decomposed as

$$n_2(\mathbf{r},\mathbf{r}') = n(\mathbf{r})n(\mathbf{r}') + n_{2,xc}(\mathbf{r},\mathbf{r}') \tag{5.2.26}$$

where $n_{2,xc}(\mathbf{r}, \mathbf{r}')$ represents the modification of the pair density due to exchange and correlation effects between the electrons and can be further written as

$$n_{2,xc}(\mathbf{r}, \mathbf{r}') = n(\mathbf{r}) n_{xc}(\mathbf{r}, \mathbf{r}'), \tag{5.2.27}$$

where $n_{xc}(\mathbf{r}, \mathbf{r}')$ is the exchange correlation hole which can be interpreted as the modification due to exchange and correlation effects of the conditional probability of finding an electron at $\mathbf{r}$ **'** knowing that one has been found at $\mathbf{r}$. The positivity of $n_2(\mathbf{r}, \mathbf{r}')$ implies that

$$n_{xc}(\mathbf{r}, \mathbf{r}') \geq -n(\mathbf{r}'). \tag{5.2.28}$$

Moreover, we have the following sum rule;

$$\int n_{xc}(\mathbf{r}, \mathbf{r}') d\mathbf{r}\text{'} = -1. \tag{5.2.29}$$

Just like the exchange-correlation hole, the exchange hole $n_x(\mathbf{r},\ \mathbf{r}\text{'})$ satisfies the conditions in Eq. (5.2.28) and Eq. (5.2.29) with n_{xc} replaced by n_x following the same decomposition steps used above.

Making use of Eqs. (5.2.25), (5.2.26), and (5.2.27) for the exchange-correlation hole, it can be seen that the exchange energy functional can be written in terms of the exchange hole as

$$E_x[n] = \frac{1}{2} \int \int \frac{n(\mathbf{r}) n_x(\mathbf{r},\ \mathbf{r}')}{|\mathbf{r} - \mathbf{r}'|} d\mathbf{r} d\mathbf{r}\text{'} \tag{5.2.30}$$

leading to the interpretation of E_x as the electrostatic interaction energy of an electron and its exchange hole. It is also useful to write the exchange energy functional as

$$E_x[n] = \int n(\mathbf{r}) \varepsilon_x[n(\mathbf{r})] d\mathbf{r}, \tag{5.2.31}$$

where $\varepsilon_x[n(\mathbf{r})]$ is the exchange energy per particle given by

$$\varepsilon_x[n](\mathbf{r}) = \frac{1}{2} \int \frac{n_x(\mathbf{r},\ \mathbf{r}')}{|\mathbf{r} - \mathbf{r}'|} d\mathbf{r}\text{'}, \tag{5.2.32}$$

which is itself a functional of the density. In approximate exchange density functionals, the quantity $\varepsilon_x[n(\mathbf{r})]$ is usually what is approximated.

In addition, the correletion energy functional $E_c[n]$ may be defined as

$$E_c[n] = \langle\psi[n]|\hat{T} + \hat{V}_{ee}|\psi[n]\rangle - \langle\Phi[n]|\hat{T} + \hat{V}_{ee}|\Phi[n]\rangle = T_c[n] + U_c[n], \tag{5.2.33}$$

which contains a kinetic contribution $T_c[n] = \langle\psi[n]|\hat{T}|\psi[n]\rangle - \langle\Phi[n]|\hat{T}|\Phi[n]\rangle$ and a potential contribution $U_c[n] = \langle\psi[n]|\hat{V}_{ee}|\psi[n]\rangle - \langle\Phi[n]|\hat{V}_{ee}|\Phi[n]\rangle$. The correlation hole is defined as

$$n_c(\mathbf{r}, \mathbf{r}') = n_{xc}(\mathbf{r}, \mathbf{r}') - n_x(\mathbf{r}, \mathbf{r}'), \tag{5.2.34}$$

and from Eq. (5.2.29), it satisfies the sum rule

$$\int n_c(\mathbf{r}, \mathbf{r'})d\mathbf{r'} = 0, \tag{5.2.35}$$

which implies that the correlation hole has negative and positive contributions [93] . The potential contribution to the correlation energy can be written in terms of the correlation hole as

$$U_c[n] = \frac{1}{2}\int\int \frac{n(\mathbf{r})n_c(\mathbf{r},\ \mathbf{r}')}{|\mathbf{r} - \mathbf{r}'|}d\mathbf{r}d\mathbf{r'}+. \tag{5.2.36}$$

D) The Khon-Sham Equations

The essence of the KS approach is rewriting the many-body problem as an auxilaiary system of non-interacting electrons moving in an effective potential. The constraint is that this auxiliary system should lead to the same electron density as the real system. The function of the real system takes the form

$$E[n] = T[n] + E_{int}[n] + E_{ext}[n]. \tag{5.2.37}$$

We can rewrite $E_{int}[n]$ as

$$E_{int}[n] = E_H[n] + E_{xc}[n] = \frac{1}{2}\int\int \frac{n(\mathbf{r})n(\mathbf{r}')}{|\mathbf{r}-\mathbf{r}'|}drdr' + E_{xc}[n]. \tag{5.2.38}$$

According to the second HK theorem the energy functional is minimal for the true ground state density. Therfore, functional derivation with respect to n, using Eq. (5.2.8) to Eq. (5.2.10) results

$$\frac{\delta E[n]}{\delta n} = \frac{\delta T}{\delta n} + V_H(\mathbf{r}) + \frac{\delta E_{xc}}{\delta n} + V_{ext}(\mathbf{r}) = \mu, \tag{5.2.39}$$

where $V_H(\mathbf{r}) = \int \frac{n(\mathbf{r}')}{|\mathbf{r}-\mathbf{r}'|}d\mathbf{r}$' is the Hartree potential and μ is the chemical potential, fixing the number of electrons in the system.

The functional of the auxiliary system of non-interacting electrons contain an effective potential $V_{KS}(\mathbf{r})$ replacing the interaction. The total electronic energy functional becomes

$$E[n] = T_0[n] + \int V_{KS}(\mathbf{r})n(\mathbf{r})d\mathbf{r}), \tag{5.2.40}$$

where $T_0[n]$ is the kinetic energy of the fictitious non-interacting electrons. The functional derivation using Eq. (5.2.8) yields

$$\frac{\delta E[n]}{\delta n} = \frac{\delta T_0}{\delta n} + V_{KS}(\mathbf{r}) = \mu. \tag{5.2.41}$$

From Eqs. (5.2.39) and (5.2.41), the effective KS potential can be specified as

$$\begin{aligned} V_{KS}(\mathbf{r}) &= \frac{\delta T}{\delta n} - \frac{\delta T_0}{\delta n} + \frac{\delta E_{xc}}{\delta n} + V_H(\mathbf{r}) + V_{ext}(\mathbf{r}) \\ &= V_{xc}(\mathbf{r}) + V_H(\mathbf{r}) + V_{ext}(\mathbf{r}), \end{aligned} \tag{5.2.42}$$

where an exchange-correlation (XC) type potential has the form:

$$V_{xc}(\mathbf{r}) = \frac{\delta T}{\delta n} - \frac{\delta T_0}{\delta n} + \frac{\delta E_{xc}}{\delta n}.$$

The corresponding Hamiltonian of the non-interacting system is

$$\hat{H} = \sum_{i=1}^{N} \left(-\frac{\hbar^2}{2m} \nabla_i^2 + V_{KS}(\mathbf{r}) \right) = \sum_{i=1}^{N} \hat{h}_{KS}(i). \tag{5.2.43}$$

The solution of the Schrödinger equation $\hat{H}\psi = E\psi$ is a Slater determinant, $\psi = |\phi_1, \phi_2, ..., \phi_N|$, since there are no interactions, leading to the KS equation given by

$$\hat{h}_{KS}(i)\phi_i(\mathbf{r}) = \varepsilon_i \phi_i(\mathbf{r}), \tag{5.2.44}$$

where $\phi_i(\mathbf{r})$ and ε_i are the KS orbitals and eigenvalues, respectively. The ground state density is related to the KS orbitals by

$$n_0(\mathbf{r}) = \sum_{i=1}^{N} |\phi_i(\mathbf{r})|^2, \tag{5.2.45}$$

with the sum running over the N orbitals with the lowest eigenvalues. The challenge in the KS approch is to find suitable approximation for the XC functional.

E) The Energy Functional

Using Eqs. (5.2.37) and (5.2.38), the total electronic energy in KS method reads as

$$E[n] = T_0[n] + E_H[n] + E_{XC}[n] + E_{ext}[n]. \tag{5.2.46}$$

The kinetic energy of the fictitious non-interacting electrons functional in terms of KS equation can be written using Eq. (5.2.40) as

$$T_0[n] = \sum_{i=1}^{N} \varepsilon_i - \int V_{KS}(\mathbf{r}) n(\mathbf{r}) d\mathbf{r}, \tag{5.2.47}$$

and substituting Eq. (5.2.42) into Eq. (5.2.47) gives

$$T_0[n] = \sum_{i=1}^{N} \varepsilon_i - \int V_{XC}(\mathbf{r}) n(\mathbf{r}) d\mathbf{r} - 2E_H[n] - E_{ext}[n]. \tag{5.2.48}$$

Putting Eq. (5.2.48) back to Eq. (5.2.46) produces

$$E[n] = \sum_{i=1}^{N} \varepsilon_i - E_H[n] + E_{XC}[n] - \int V_{XC}(\mathbf{r}) n(\mathbf{r}) d\mathbf{r}. \tag{5.2.49}$$

The functional $E_{XC}[n]$ can also be written as

$$E_{XC}[n] = \int \varepsilon_{XC}[n(\mathbf{r})] n(\mathbf{r}) d\mathbf{r}. \tag{5.2.50}$$

From Eq. (5.2.9) for functional derivation it follows that

$$E_{XC}[n] = \frac{\delta E_{XC}[n]}{\delta n(\mathbf{r})} = \varepsilon_{XC}[n(\mathbf{r})] + \frac{\partial \varepsilon_{XC}[n(\mathbf{r})]}{\partial n(\mathbf{r})} n(\mathbf{r}). \tag{5.2.51}$$

Using the last result of Eq. (5.2.47) and Eq. (5.2.51) in Eq. (5.2.46) and rearanging terms for the total energy of the elecrons, we obtain

$$E[n] = \sum_{i=1}^{N} \varepsilon_i - E_H[n] - \int \frac{\partial \varepsilon_{XC}[n(\mathbf{r})]}{\partial n(\mathbf{r})} n(\mathbf{r}) d\mathbf{r}. \tag{5.2.52}$$

The correspondence of the charge density and energy of the many-body and the non-interacting system is only exact if the exact functional is known. In this sense Kohn-Sham density functional theory is an empirical methodology, which we do not know (and have no way of systematically approaching) the exact functional. However, the functional is universal and it does not depend on the materials being studied. For any particular system we could, in principle, solve the Schrödinger equation exactly and determine the energy functional and its associated potential. This, of course, involves a greater effort than a direct solution for the energy. Nevertheless, the ability to determine exact properties of the universal functional in a number of systems allows excellent approximations to the functional to be developed and used in a wide range of materials, a property usually associated with an ab-initio theory. For this reason, the approximations to density functional theory discussed below are often referred to as ab-initio or first principles methods.

The computational cost of solving the Kohn Sham equations, Eq. (5.2.44), scales formally

as N^3 (due to the need to maintain the orthogonality of N orbitals) but in current practice is dropping towards N^1 through the exploitation of the locality of the orbitals.

For calculations in which the energy surface is the quantity of primary interest, DFT offers a practical and potential highly accurate alternative to the wave function methods discussed above. In practice, the utility of the theory rests on the approximation used for $E_{XC}[n]$.

5.2.2 Exchange-Correlation Functionals

We will review the most widely used exchange-correlation (XC) approximations, the Local Density Approximation (LDA), the Generalised Gradient Approximation (GGA), and briefly the hybrid functionals.

A) The Local Density Approximation for E_{XC}[n]

Thomas and Fermi studied the homogeneous electron gas in the early 1920s [94]. The orbitals of the system are, by symmetry, plane waves. If the electron-electron interaction is approximated by the classical Hartree potential (that is, exchange and correlation effects are neglected), then the total energy functional can be readily computed [94]. Under these conditions, the dependence of the kinetic and exchange energy on the density of the electron gas can be extracted [95, 96, 97] and expressed in terms of a local functions of the density. This suggests that in the inhomogeneous system, we might approximate the functional as an integral over a local function of the charge density.

The local exchange correlation energy per electron might be approximated as a simple function of the local charge density (say, $\varepsilon_{xc}(n)$). That is, an approximation of the form:

$$E_{XC}^{LDA}[n] = \int n(\mathbf{r})\varepsilon_{XC}^{UEG}[n(\mathbf{r})]d\mathbf{r}, \tag{5.2.53}$$

where $\varepsilon_{XC}^{UEG}[n(\mathbf{r})]$ is the exchange-correlation energy per particle of the infinite uniform electron gas (UEG) with density $n(\mathbf{r})$. Within the LDA, $\varepsilon_{XC}[n]$ is a function of only the local value of

the density. It can be separated into exchange and correlation contributions as

$$\varepsilon_{XC}^{UEG}[n] = \varepsilon_{X}^{UEG}[n] + \varepsilon_{C}^{UEG}[n]. \tag{5.2.54}$$

The Dirac form can be used for $\varepsilon_{X}^{UEG}[n]$, and hence

$$\varepsilon_{X}^{UEG}[n] = -C[n(\mathbf{r})]^{\frac{1}{3}}, \tag{5.2.55}$$

where for generality a free constant, C, has been introduced rather than that determined for the homogeneous electron gas. This functional form is much more widely applicable than is implied from its derivation and can be established from scaling arguments [96]. The functional form for the correlation energy density, $\varepsilon_{C}^{UEG}[n]$, is unknown and has been simulated for the homogeneous electron gas in numerical quantum Monte-Carlo calculations which yield essentially exact results [98]. The resultant exchange correlation energy has been fitted by a number of analytic forms [99, 100, 101] all of which yield similar results in practice and are collectively referred to as LDA functionals. Fig. 5.1 depicts how the self consistent solution of the KS equation is obtained.

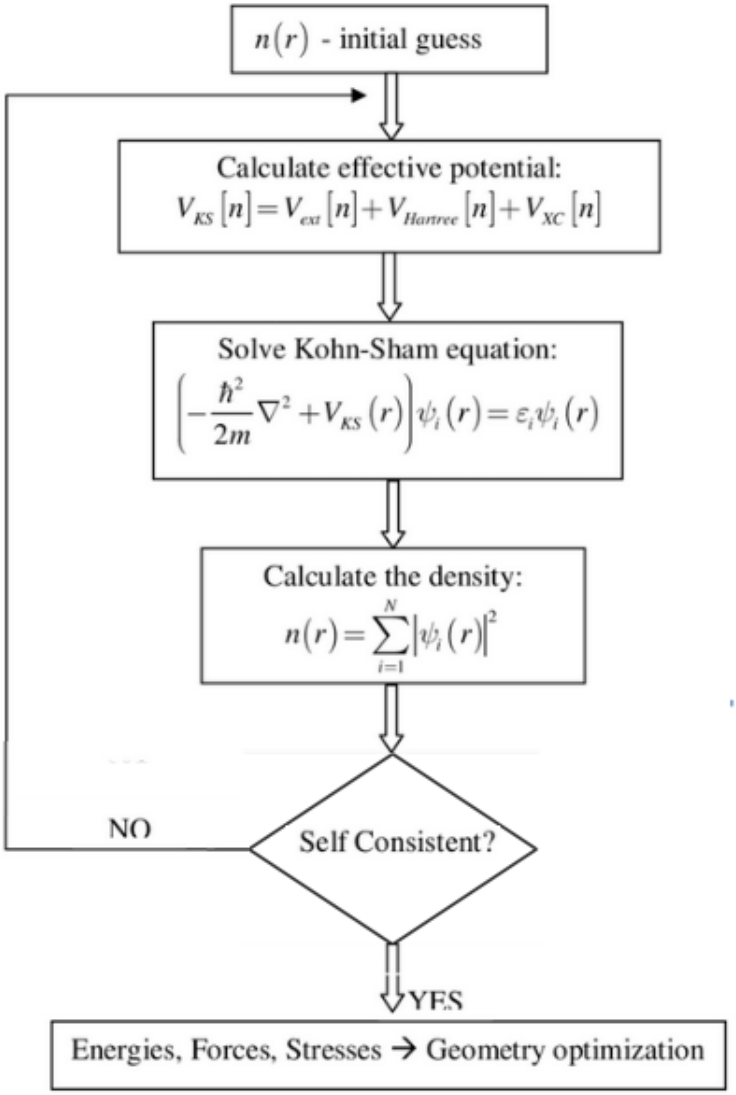

Figure 5.1: Schematic flow chart of the self-consistent solution of the Kohn-Sham equation.

The LDA has proven to be a remarkably fruitful approximation. Properties such as structure, vibrational frequencies, elastic moduli, and phase stability (of similar structures) are described reliably for many systems. However, in computing energy differences between rather different structures the LDA can have significant errors. For instance, the binding energy of many systems is overestimated (typically by 20-30 %) and energy barriers in diffusion or chemical reactions may be too small or absent. Nevertheless, the remarkable fact is that the LDA works as well as it does given the reduction of the energy functional to a simple local function of the density [102].

B) The Generalized Gradient Approximation

The local density approximation can be considered to be the zeroth order approximation to the semi-classical expansion of the density matrix in terms of the density and its derivatives [103]. A natural progression beyond the LDA is thus to the gradient expansion approximation (GEA) in which first order gradient terms in the expansion are included. This results in an approximation for the exchange hole [24] which has a number of unphysical properties: it does not ensure the normalization condition, it is not negative definite, and it contains oscillations at large magnitude of the separation between an electron at $\mathbf{r}$ and an electron at $\mathbf{r}'$ (i.e., $\mathbf{r} - \mathbf{r}'$) [104].

In the generalized gradient approximation (GGA), a functional form is adopted which ensure the normalization condition and that the exchange hole is negative definite [105, 106]. This leads to an energy functional that depends on both the density and its gradient but retains the analytic properties of the exchange correlation hole inherent in the LDA.

The typical form for a GGA functional is

$$E_{XC}^{GGA}[n] = \int \varepsilon[n(\mathbf{r}), |\nabla n(\mathbf{r})|] d\mathbf{r}, \tag{5.2.56}$$

where ε is some function. The GGAs are semi-local approximations in the sense that ε does not only use the local value of the density $n(\mathbf{r})$ but also its gradient $\nabla n(\mathbf{r})$ [107]. In practice, GGA functionals are more generally formulated in terms of spin densities ($n_\uparrow$, $n_\downarrow$) and their gradients ($\nabla n_\uparrow$, $\nabla n_\downarrow$) [100].

Many GGA functionals have been proposed. We very briefly review here some of the most widely used ones.

(i) PW91 exchange-correlation functional

The Perdew-Wang 91 (PW91) (see Refs. [108, 109]) exchange-correlation functional is based on a model of the exchange hole $n_x(\mathbf{r}, \mathbf{r}')$ in Eq. (5.2.32) and of the coupling-constant-integrated correlation hole $n_c(\mathbf{r}, \mathbf{r}')$ by replacing n_x by n_c in Eq. (5.2.32). The idea is to start from the GEA model of these holes given as gradient expansions and remove the unrealistic long-range parts of these holes to restore important conditions satisfied by the LDA. Specifically, a cutoff in $|\mathbf{r} - \mathbf{r}'|$ is applied to enforce the normalization condition of Eq. (5.2.29). Similarly, a cutoff is applied

on the correlation hole to enforce the condition that the hole integrates to zero as stated in Eq. (5.2.1). The exchange and correlation energies per particle calculated from these numerical holes are then fitted to functions of n and $|\nabla n|$ chosen to satisfy a number of exact conditions.

(ii) PBE exchange-correlation functional

The Perdew-Burke-Ernzerhof (PBE) [109] exchange-correlation functional is a simplification of the PW91 functional. The exchange and correlation energies per particle are expressed as simpler functions of n and $|\nabla n|$ enforcing less exact conditions and with no fitted parameters.

C) The Hybrid Functional Method

The excitation energies of a system are not accurately described by DFT in local approximations. As a result, the band gaps of insulators and semiconductors are systematically underestimated, which is known as the DFT band gap problem.

One of the most recent and best solutions to the DFT band gap problem is the hybrid functional method, where exact (Hartree) exchange is mixed into the functional, at the short range [110, 111]. Hybrid functional (HF) calculations are very computationally intensive. The HF method, on which hybrid functionals are based, uses the wave functions instead of the density, which have less symmetric, as a result of the Bloch theorem.

5.2.3 Hubbard Correction Model, DFT+U

The DFT+U (the Hubbard correction (+U) applied to a generic approximate DFT functionals) is another simple corrective approach that were formulated to improve the accuracy of DFT functionals in describing the ground-state of correlated systems [112, 113, 114]. The idea is quite simple and consists in using the Hubbard Hamiltonian to describe strongly correlated electronic states (typically, localized d or f orbitals for which the Coulomb d-d interaction should be taken into account), while the rest of the valence electrons (delocalized s and p electrons) are treated at the standard level of approximation (LDA or GGA). The Hubbard Hamiltonian of the non-interacting system is

$$\hat{H} = \sum_{i=1}^{N} \left(-\frac{1}{2}\nabla_i^2 + V_{KS}(\mathbf{r}_i) + V_U(\mathbf{r}_i) \right) = \sum_{i=1}^{N} \hat{h}_{KS}(i). \tag{5.2.57}$$

The solution of the Schrödinger equation $\hat{H}\psi = E\psi$ is a Slater determinant, $\psi = |\phi_1, \phi_2, ..., \phi_N|$, since there are no interactions, leading to the KS equation

$$\hat{h}_{KS}(i)\phi_i(\mathbf{r}) = \varepsilon_i\phi_i(\mathbf{r}), \tag{5.2.58}$$

where $V_U(\mathbf{r})$, $\phi_i(\mathbf{r})$, and ε_i are the Hubbard potential, the KS orbitals and eigenvalues, respectively. The ground-state density is related to the KS orbitals by

$$n_0(\mathbf{r}) = \sum_{i=1}^{N} |\phi_i(\mathbf{r})|^2, \tag{5.2.59}$$

with the sum running over the N orbitals with the lowest eigenvalues.

DFT+U performs a linearization of the energy only with respect to the electronic degrees of freedom for which self-interaction is expected to be stronger (localized atomic states) and with an effective coupling that, although orbital-independent (indeed corresponding to an atomically averaged quantity), can be evaluated ab-initio. Thus, it results, at the same time, more computationally efficient and (arguably) more physically transparent than the hybrid functionals as a corrective scheme to DFT. DFT+U is also effective in correcting the under-estimated energy band gap.

5.3 Practical Calculations

5.3.1 Introduction

This section reviews the practical methods for DFT such as the Bloch theorem, the basis set, the electronic wave vector k-point grid, and briefly discuss the pseudo-potential approach, the widespread technique for performing DFT calculations for periodic systems, in combination with a plane wave basis set and the software package used in computational part of this thesis (Quantum EXPRESSO).

5.3.2 The Bloch Theorem

The first requirement for a practical approch to DFT is the use of the spatial periodicity of the crystal lattice. A periodic structure is defined by a unit cell, which is repeated in all spatial directions. Accordingly, the KS potential is periodic for all lattice vectors $\mathbf{R}$ of the lattice given by

$$V_{KS}(\mathbf{R}) = V_{KS}(\mathbf{r}+\mathbf{R}). \tag{5.3.1}$$

For the periodic lattice that has been introduced, the Bloch theorem holds:

- The wave function of a particle in a periodic potential can be written as a product of a plane wave and a periodic function with the same periodicity as the lattice.

The Bloch wave function can be written as

$$\phi_{i\mathbf{k}} = e^{i\mathbf{k}.\mathbf{R}} u_{i\mathbf{k}}(\mathbf{r}), \tag{5.3.2}$$

with

$$u_{i\mathbf{k}}(\mathbf{r}) = u_{i\mathbf{k}}(\mathbf{r}+\mathbf{R}). \tag{5.3.3}$$

It follows easily that the energy spectrum is periodic with respect to the reciprocal lattice. That is,

$$E_{i\mathbf{k}(\mathbf{k})} = E_{i\mathbf{k}}(\mathbf{k}+\mathbf{G}), \tag{5.3.4}$$

for all reciprocal lattice vectors $\mathbf{G}$. Therfore, the energy spectrum is fully represented within the Brillouin zone (BZ), the primitive cell of all reciprocal lattices. This representation is called the band structure.

5.3.3 Plane Wave Basis Set

It is convenient to expand a periodic function such as $u_{i\mathbf{k}}(\mathbf{r})$ using a plane wave basis set as

$$u_{n\mathbf{k}}(\mathbf{r}) = \sum_{\mathbf{G}} c_{i\mathbf{k}}(\mathbf{G}) e^{i\mathbf{G}.\mathbf{r}}, \tag{5.3.5}$$

where the summation runs over all reciprocal lattice vectors. The plane waves form a complete basis set and thus the expansion is a Fourier series. Here in lies one of the main advantages of a plane wave basis, namely, a fast Fourier transform (FFT) can be performed to switch between real and reciprocal spaces. Substituting Eq. (5.3.5) into Eq. (5.3.2), it follows the electronic wave functions are given by

$$\phi_{i\mathbf{k}}(\mathbf{r}) = \sum_{\mathbf{G}} c_{i\mathbf{k}}(\mathbf{G}) e^{i(\mathbf{k}+\mathbf{G}).\mathbf{r}}. \tag{5.3.6}$$

The kinetic energy is related to plane waves in this expansion by $(\mathbf{k}+\mathbf{G})^2/2$. The summation over $\mathbf{G}$ is infinite and thus for practical reasons an upper boundary, the cutoff energy E_{cut} should be set so that $(\mathbf{k}+\mathbf{G})^2/2 < E_{cut}$. The cutoff energy can be understood in terms of a 'resolution': details in the wave function smaller than $2\pi/G_{max}$ are neglected. It results in the second important advantage of the plane wave basis set, namely, the accuracy can be improved systematically by increasing E_{cut}.

5.3.4 Integration Over the First Brillouin Zone: the k-Point Grid

In DFT, all quantities are derived from the electronic density defined by

$$n(\mathbf{r}) = \int_{BZ} d\mathbf{k} \sum_{i=1}^{N_k} f_{i\mathbf{k}} |u_{i\mathbf{k}}(\mathbf{r})|^2, \tag{5.3.7}$$

where the sum runs over all bands at point $\mathbf{k}$, $N_\mathbf{k}$ and $f_{i\mathbf{k}}$ are the occupancy of the band, either 1 - below the Fermi level - or 0, otherwise. In order to facilitate the convergence of the integration with respect to the number of $\mathbf{k}$-points, it is advantageous to replace the step function by a smooth function. This is so-called finite-temperature approach, also known as smearing, since it

mimics the effect of temperature [115]. Gaussian functions are frequently used to describe this smearing.

From an infinitely extended real space lattice, $\mathbf{k}$ is continuous variable, restricted to the first BZ owing to periodicity. In numerical calculations, integration over a continuous variables is not attainable. Therefore, a $\mathbf{k}$-point grid is constructed to sample the first BZ. Commonly, a Monkhorst-Pack grid, an equidistant grid, is selected [116]. Additionally, sampling of the irreducible BZ (IBZ), the reduction of the first BZ by the lattice symmetries, is sufficient for calculation of the density. The normalized weight $w_{\mathbf{k}}$ has to be included, to take into account the multiplicity of each $\mathbf{k}$-point. Consequently, the electron density becomes

$$n(\mathbf{r}) = \sum_{\mathbf{k}\epsilon IBZ} w_{\mathbf{k}} \sum_{i=1}^{N_k} f_{i\mathbf{k}} |u_{i\mathbf{k}}(\mathbf{r})|^2, \tag{5.3.8}$$

5.3.5 Pseudopotential and Plane Waves Method

The pseudopotential is an attempt to replace the complicated effects of the motion of the core (i.e., non-valence) electrons of an atom and its nucleus with an effective potential, or pseudopotential, so that the *Schrödinger* equation contains a modified effective potential term instead of the Coulombic potential term for the core electrons normally found in the *Schrödinger* equation.

In physics, a pseudopotential or effective potential is used as an approximation for the simplified description of complex systems. Applications include atomic physics and neutron scattering. The pseudopotential approximation was first introduced by Hans Hellmann in 1934 [117].

The electronic wave function (orbitals) of the elements contained in the unit cell are fed as input to a practical DFT routine. The true (all-electron) orbitals may contain many nodes, leading to a huge basis set (a high E_{cut}). Moreover, for bonding, the core electrons are usually not relevant. The oscillations of the true valence electron orbitals near the core are due to the core electrons. The nodes and thus the oscillations arise from the orthogonality of the orbitals to the core orbitals. In a pseudopotential (PP) method, the effect of the more complex, oscillatory behaviour of the wave functions close to the atom cores due to the core electrons, is effectively eliminated from the true orbitals yielding a smoothed function (see Fig. (5.2)). This allows the pseudo-wavefunctions to be described with far fewer Fourier nodes, thus making plane-wave

basis sets practical to use.

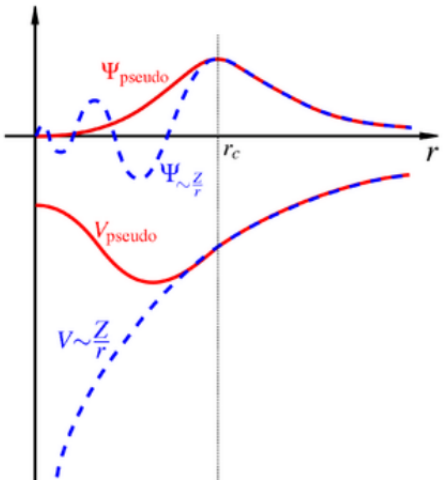

Figure 5.2: Comparison of a wave function in the Coulomb potential ($V \approx z/r$) of the nucleus to the one in the pseudo-potential (V_{pseudo}). The real ($\psi \approx z/r$) and the pseudo wavefunction (ψ_{pseudo}) and potentials match above a certain cutoff radius $\mathbf{r}_c$

A widespread technique for performing DFT calculations for periodic systems has turned out to be the pseudopotential approach in combination with a plane wave basis set and thus extract a smooth part ϕ_v from the valence orbital $|\psi_{c,v}\rangle = |\psi_v\rangle + \sum\langle\psi_c|\psi_v\rangle|\psi_c\rangle$ The smooth part ϕ_v of the valence state has no overlap with the core states ψ_c by construction.

Both valence and core electrons satisfy the atomic *Schrödinger* equation with the atomic Hamiltonian H and the core potential, V core. That is,

$$\hat{H}|\psi_{c,v}\rangle = [T + V_{ee} + V^{core}]|\psi_{c,v}\rangle = \epsilon_{c,v}|\psi_{c,v}\rangle. \tag{5.3.9}$$

An application of the atomic Hamiltonian on the new, smoothed valence states ϕ_v results in a modified Schrödinger equation with a new Pseudo Hamiltonian given by

$$\hat{H} + \sum_c (\epsilon_v - \epsilon_c)|\psi_c\rangle\langle\psi_c| = \epsilon_v|\phi_v\rangle. \tag{5.3.10}$$

Norm-conserving and ultr-asoft are the two most common forms of pseudopotential used in modern plane-wave electronic structure codes. They allow a basis-set with a significantly lower cut-off (the frequency of the highest Fourier mode) to be used to describe the electron wave

functions and so allow proper numerical convergence with reasonable computing resources.

5.3.6 Software Package: Quantum ESPRESSO

We discussed that DFT can be utilized to reduce the many-body problem. Still, the KS equations are to be solved self-consistently large basis set and an appropriate super cell have to be selected to implement more complex systems. So, DFT is implemented numerically in a wide variety of software packages, such as ABINIT, Gaussian, Quantum ESPRESSO, SIESTA, VASP, WIEN2k, etc. These differ in several aspects, i.e., the choice of the basis functions, the pseudo-potentials, and the algorithms used for diagonalization of the KS Hamiltonian. Quantum ESPRESSO is a distribution of packages, rather than a single monolithic tightly integrated package. The core distribution contains the two main packages [118]:

- the Plane-Wave Self-Consistent Field (Pwscf) used to perform self-consistent calculation of the Kohn Sham equations and
- the Car-Parrinello (Cp) used for performing molecular dynamics calculations.

They share a common installation method, input format, PP format, data output format, and large parts of the basic code. The quantum ESPRESSO package is available at the web-site "https://w.w.w quantum-espresso.org/".

5.4 Results and Discussions

5.4.1 Introduction

The structural and electronic properties calculations were performed on pure GaSb and Fe alloyed GaSb by employing the software quantum ESPRESSO package. All calculations were carried out by solving the Kohn-Sham equations using plane-wave pseudo-potential (pw.x code) in the framework of the Density Functional Theory (DFT). The ab-initio computational results on the structural and electronic properties such as the lattice parameters, total energy, crystalline structure, energy band structures, the band gap energies, the density of states (DOS), and the projected density of states (PDOS) for both GaSb semiconductor and (Ga,Fe)Sb DMS with

normalized Fermi levels were illustrated with different psudopotentials. Finally, the DFT+U calculation was performed with selected psudopotentials and its effect in correcting the band gap problem encountered due to the alloying is demonstrated.

5.4.2 The Electronic Wave Vector k-Point Grid

In DFT calculations all quantities are derived from electron density. This electron density, in principle, should be integrated over **k**-space in the reduced zone or first Brillouin zone (BZ) owing to periodicity of the lattice, and it is continuous in the reciprocal lattice space (IBZ). However, integration over continuous variables is impossible in numerical calculations. Therefore, a **k**-point grid should be constructed in order to sample the first BZ and hence facilitate the numerical calculations. Based on this fact, a thoughtful selection of **k**-point grid along suitable high-symmetry lines containing the L - Γ - X - K - Γ path was made and the corresponding convergence test was performed. The first Brillouin zone along with the symmetry point and symmetry lines are indicated in Fig. 5.3 and the result of the **k**-point grid optimization calculations performed was plotted in Fig. 5.4.

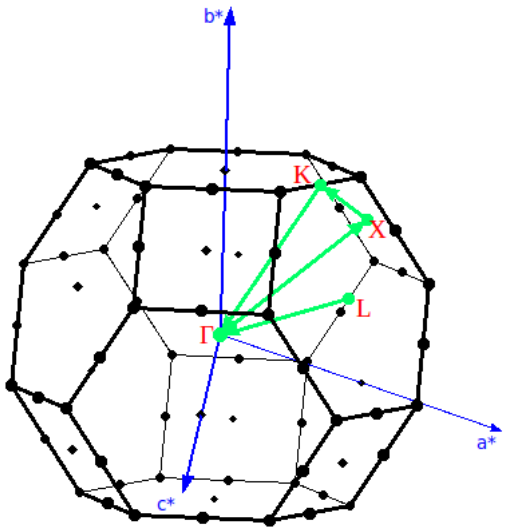

Figure 5.3: First Brillouin zone.

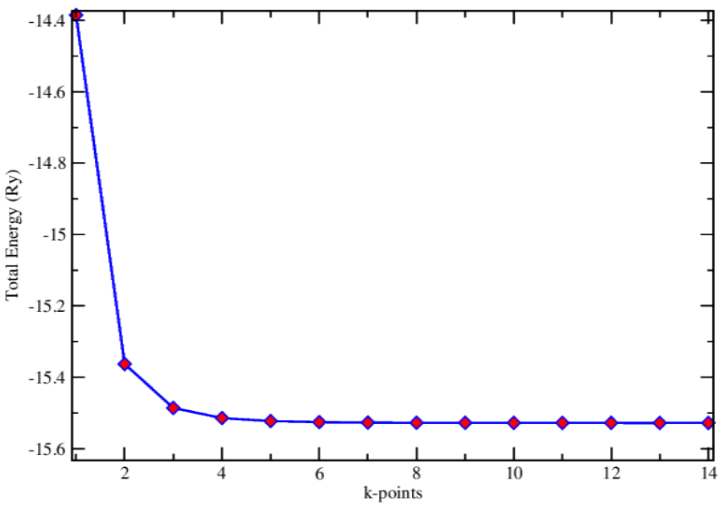

Figure 5.4: **k**-points convergence test.

From Fig. 5.4, optimized value of **k**-point grid $12 \times 12 \times 12$ was chosen and used in the subsequent calculations.

5.4.3 Crystalline Structures

Fig. 5.5 depict the optimized structures of bulk zinc-blende GaSb semiconductor and Fe/GaSb DMS for conventional unit cells and the results agree with the results obtained in [12, 43].

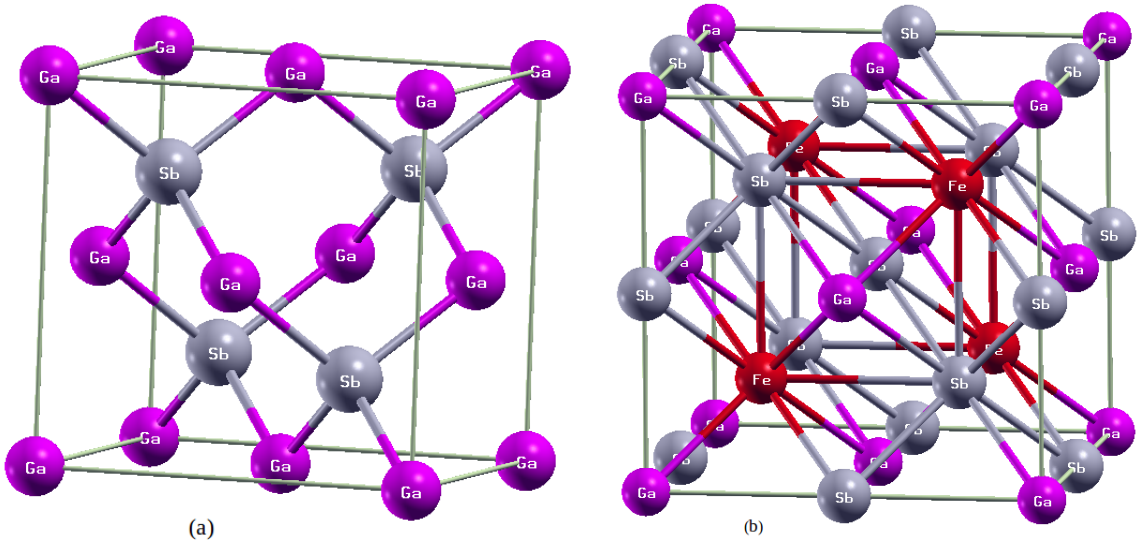

Figure 5.5: Conventional zinc-blende unit cell of bulk crystal structures of: (a) GaSb and (b) Fe/GaSb.

5.4.4 Lattice Parameters

The information about the bulk structures simplifies drastically the calculation of the equilibrium structure. In order to achieve the equilibrium structure, one has to calculate the lattice parameter that minimizes the DFT total energy. Three norm-conserving (pbe-mt-fhi-UPF, pz-bhs-UPF, and pz-mt-fhi-UPF) and one ultra-soft (pw91-n-van-UPF) psedopotentials were taken into account, and the results of the calculations performed for lattice parameter optimization were shown in Fig. 5.6 and Fig. 5.7 for undoped and Fe doped GaSb, respectively.

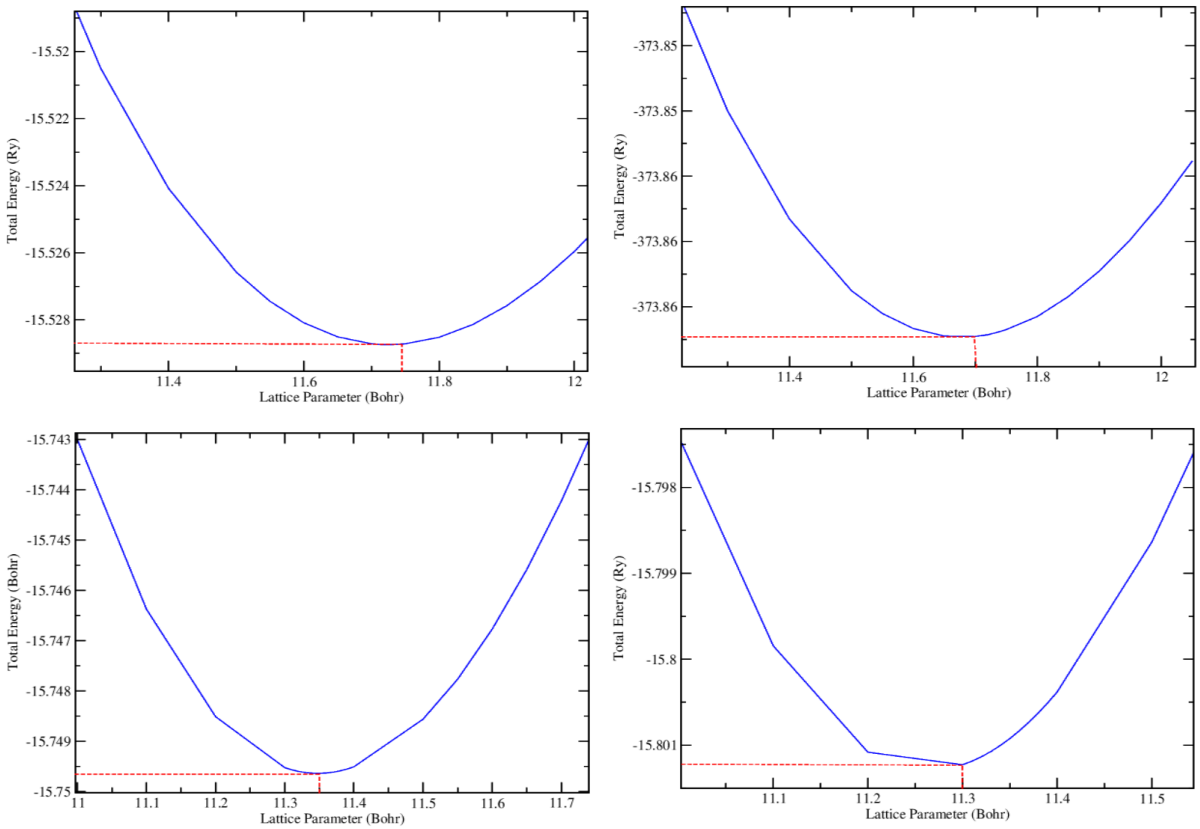

Figure 5.6: Lattice parameter convergence test for GaSb obtained with pseudopotential pbe-mt-fhi-UPF (left top panel), pw91-n-van-UPF (right top panel), pz-bhs-UPF (left bottom panel), and pz-mt-fhi-UPF (right bottom panel).

Fig. 5.6 shows the lattice parameters that minimize the DFT total energy for GaSb with pbe-mt-fhi-UPF close to 11.75 Bohr, for pw91-n-van-UPF close to 11.7 Bohr, for pz-bhs-UPF close to 11.35 Bohr and for pz-mt-fhi-UPF close to 11.3 Bohr. The energy versus lattice parameter curves are shifted down rather uniformly with increasing cutoff and are not strongly dependent on **k**-

points. All results agree well with the experimental values 6.09593 $\mathring{A}$ (11.52 Bohr) reported in Ref. [119]. The differences observed are attributed to different approximation schemes considered in our DFT calculations. These lattice parameters were used in all the subsequent GaSb electronic parameters calculations.

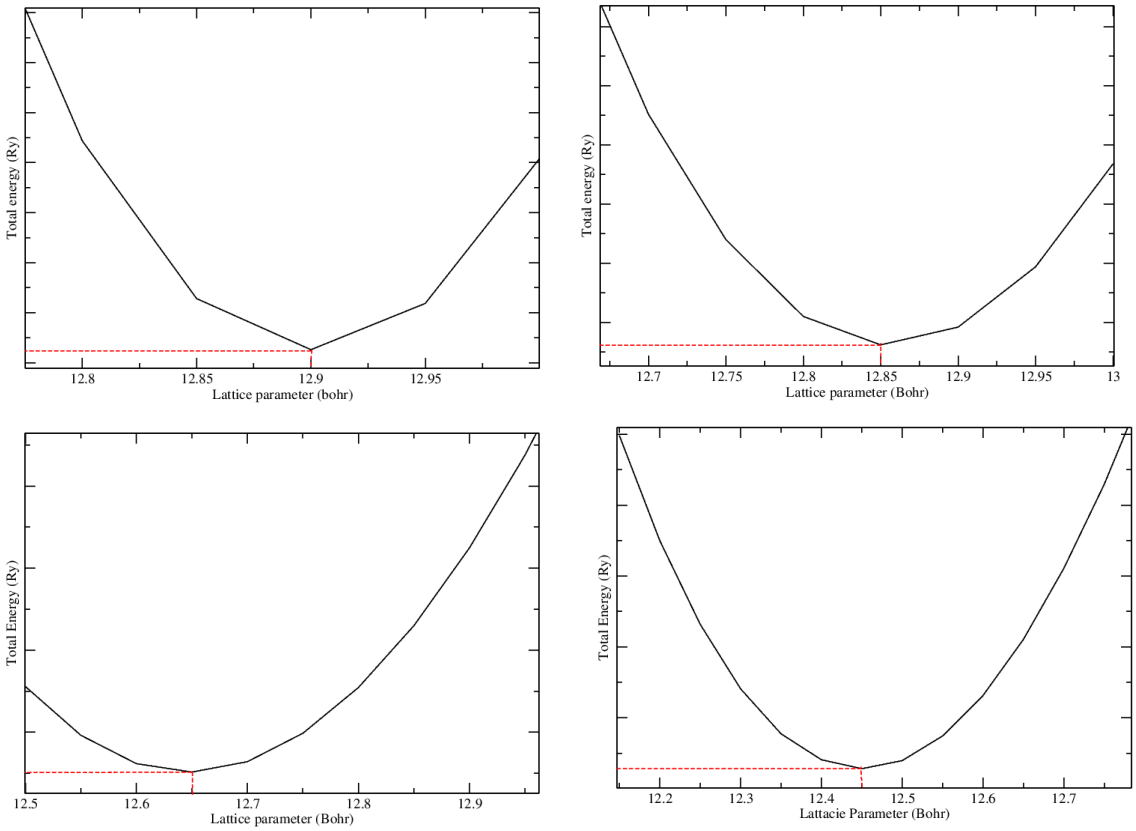

Figure 5.7: Lattice parameter convergence test for GaSb obtained with pseudopotential pbe-mt-fhi-UPF (left top panel), pw91-n-van-UPF (right top panel), pz-bhs-UPF (left bottom panel), and pz-mt-fhi-UPF (right bottom panel).

Fig. 5.7 shows the lattice parameters that minimize the DFT total energy for Fe/GaSb with pbe-mt-fhi-UPF close to 12.9 Bohr, for pw91-n-van-UPF close to 12.85 Bohr, for pz-bhs-UPF close to 12.65 Bohr, and for pz-mt-fhi-UPF close to 12.45 Bohr. These results compared to GaSb show significant increase and the results were used in all the subsequent Fe/GaSb electronic parameters calculations.

In our DFT calculations, we could also observe the effect of pressure by varying the lattice parameter of the system. The lattice parameter for psudopotential pbe-mt-fhi-UPF was decreased in steps starting from $\approx$ 12.9 Bohr at equilibrium. The obtained result was plotted in Fig. 5.8.

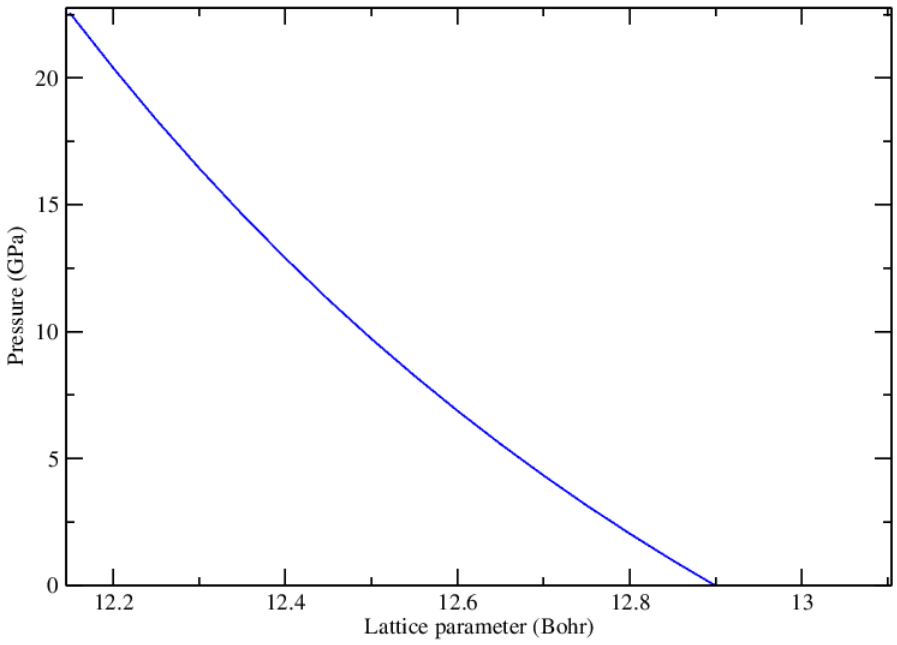

Figure 5.8: Pressure versus lattice parameter for GaSb obtained with pseudopotential pbe-mt-fhi-UPF.

Fig. 5.8 clearly revealing, pressure and lattice parameter have inverse relationship. As the lattice parameter decreases from 12.9 to 12.15 Bohr, the pressure in the system increases 0 to 22.55 GPa.

Most quantities that can be computed using DFT such as total energy, band structures, density of states (DOS), and the projected density of states (PDOS) depend critically on the kinetic energy cutoff (ecutwfc) which is employed for the calculations. Therefore, one should always perform ecutwfc convergence test before running the calculations. The kinetic energy cutoff ecutwfc (in Ry) determines the size of the plane-wave (PW) basis set used to expand wave functions (i.e., Kohn-Sham orbitals). The use of very small values of ecuwfc greatly affects the results of DFT calculations. Likewise, because of the fact that calculations with higher cutoff values are highly time consuming, one should also avoid the use of very large values of ecutwfc. Hence, a judicious choice of ecutwfc can save us from errors as well as computer run time problems. Based on these notations, a series ecutwfc convergence test calculations were undertaken for bulk fcc GaSb. The result obtained from these calculations was plotted in Fig. 5.9.

First principle calculations were performed within the GGA to the density functional theory. The valence electronic wave functions were expanded in plane wave basis sets with optimized kinetic energy cutoff 60 Ry ecutwfc value and the charge density was computed using 480 Ry ecutrho (for the ultrasoft psudopotential) and 240 Ry ecutrho (for the norm-conserving psudopotentials) also Γ-centered **k**-point mesh was chosen and employed in all subsequent calculations.

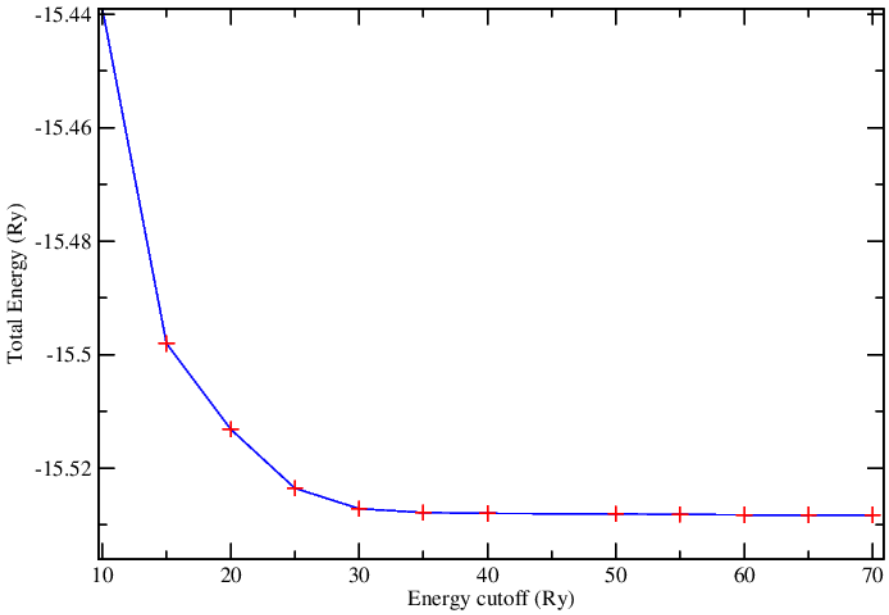

Figure 5.9: The ecutwfc convergence test for GaSb.

5.4.5 Energy Band Structures, DOSs, and PDOSs

As shown from the simulated energy band structure, the conduction bands for GaSb (Fig 5.10) and Fe/GaSb (Fig. 5.13) are characterized by three sets of minima: the lowest minima at Γ points, slightly higher minima at the L points at the surface of the first Brillouin zone, and even higher minima at the X- points. The valence band has the structure common to all zinc-blende semiconductors [43]. The path from the center of Γ zone to the points of high symmetry Γ $[k = 0]$ is very significant for the description of the band structure of the crystal.

A) Energy Band Structures, DOSs, and PDOS of GaSb

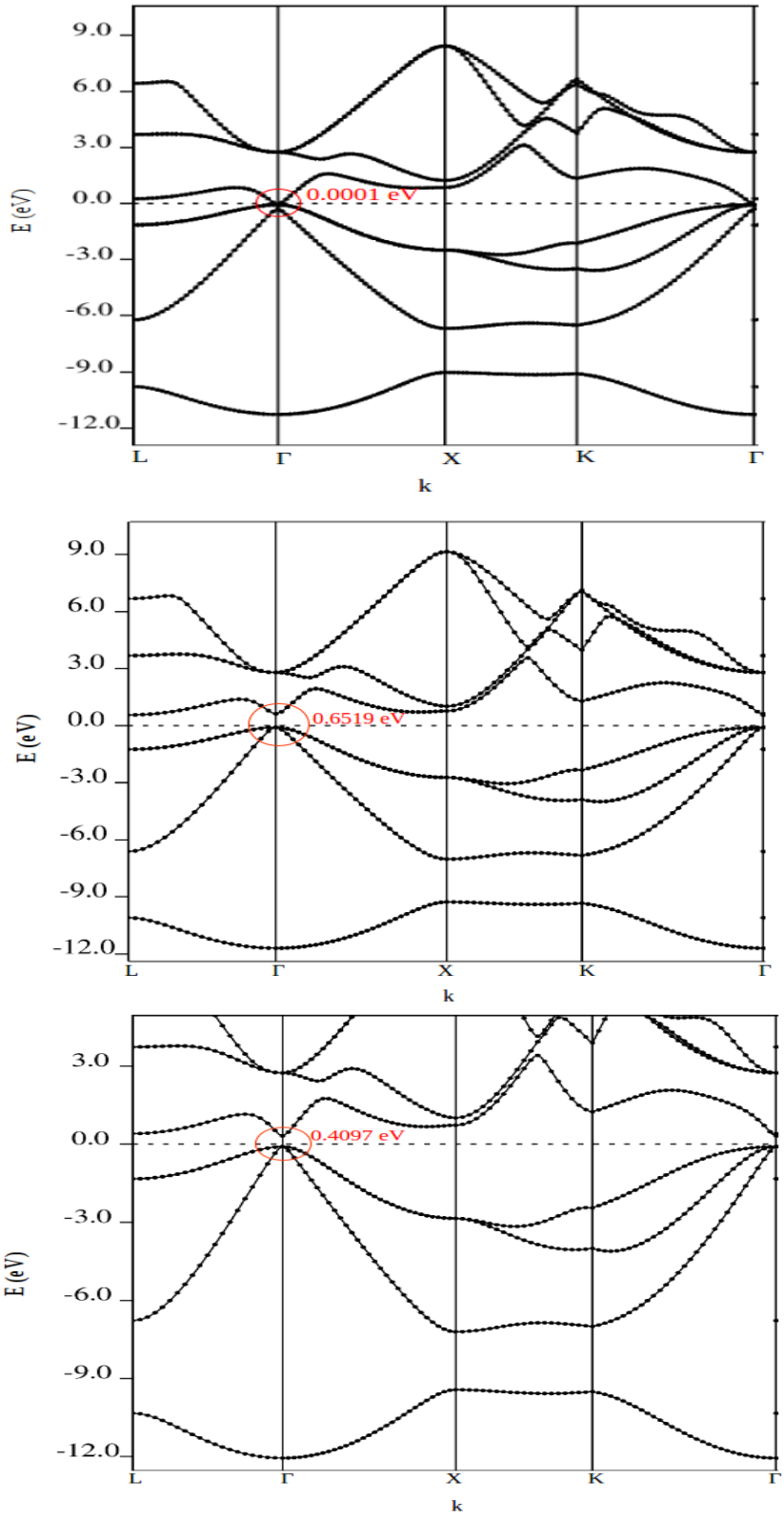

Figure 5.10: Energy band structure for GaSb obtained with pseudopotential pbe-mt-fhi-UPF (top panel), pz-bhs-UPF (middle panel), and pz-mt-fhi-UPF (bottom panel).

The band structures of zinc-blende GaSb at 0 K are shown in Fig. 5.10. The obtained results indicate that the valence band maximum and conduction band minimum lie at the Γ point, making zinc-blende GaSb and Fe/GaSb direct band gap. The energy gap for pz-bhs-UPF found largest and for pbe-mt-fhi-UPF found smallest or nearly zero.

The corresponding DOSs and PDOSs were also calculated for the optimized lattice parameters and the results are shown in Fig. 5.11 and Fig. 5.12 for GaSb.

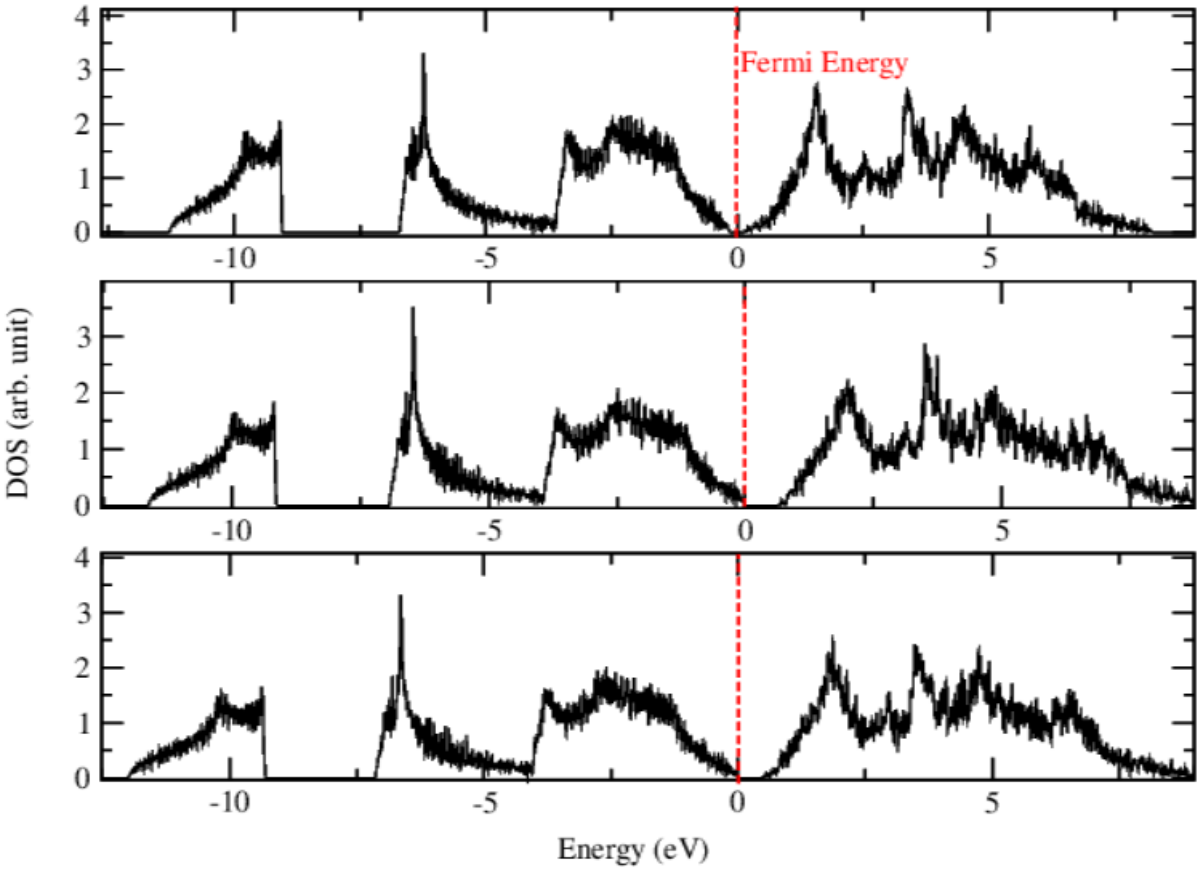

Figure 5.11: Density of state plots for GaSb obtained with pseudopotential pbe-mt-fhi-UPF (top panel), pz-bhs-UPF (middle panel), and pz-mt-fhi-UPF (bottom panel).

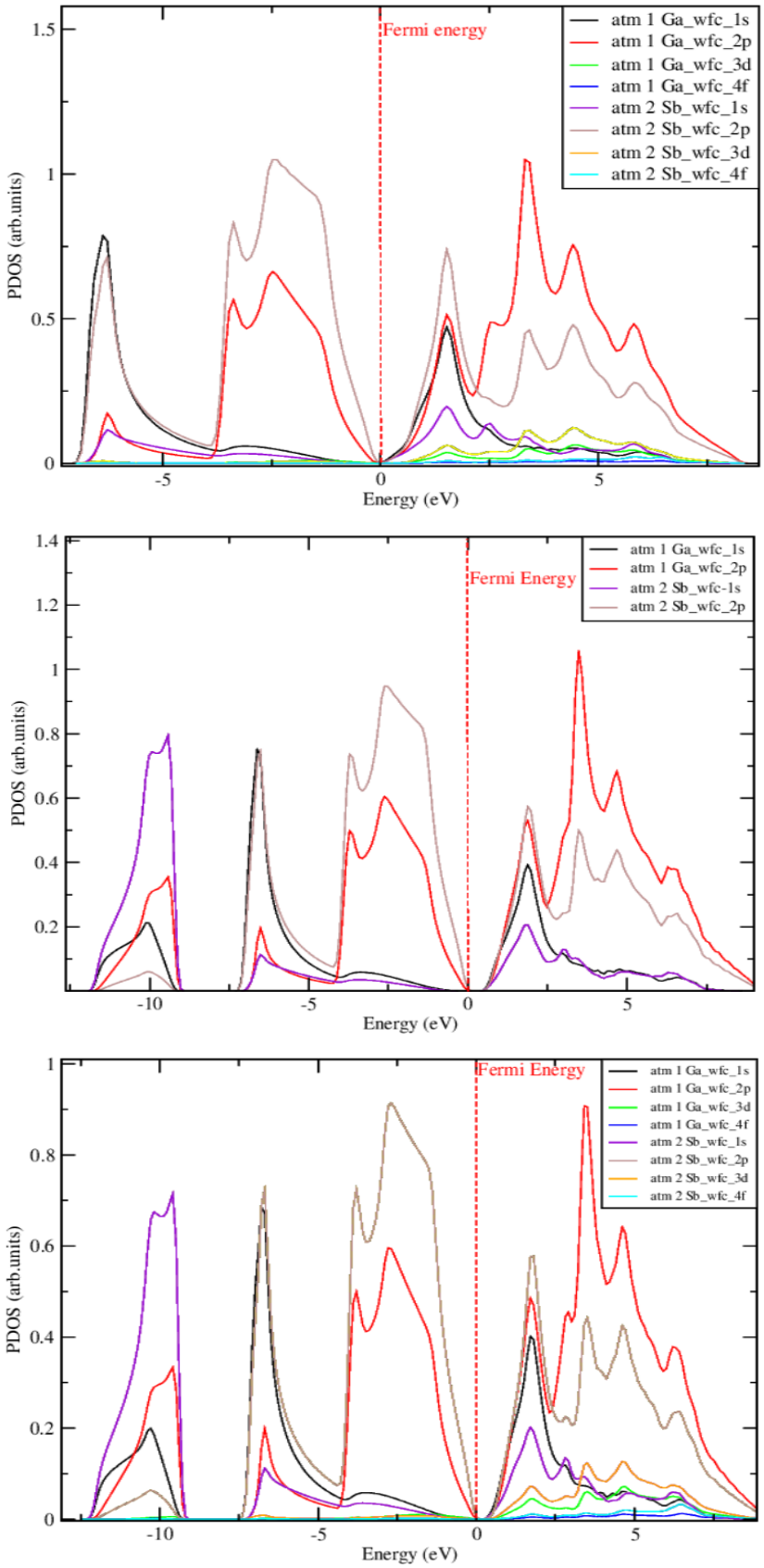

Figure 5.12: Projected density of state plots for GaSb obtained with pseudopotential pbe-mt-fhi-UPF (top panel), pz-bhs-UPF (middle panel), and pz-mt-fhi-UPF (bottom panel).

From the GGA calculation, the band gap energy at Γ [$k = 0$] points is 0.0001, 0.6519 and 0.4097 eV for pbe-mt-fhi-UPF, pz-bhs-UPF and pz-mt-fhi-UPF, respectively. For pw91-n-van-UPF we could not get the expected type of energy band structure. Comparing the band gap energy obtained for pz-bhs-UPF and pz-mt-fhi-UPF psudopotential with the experimental value reported, 0.726 eV [30] our results are significantly lower. This is because DFT ignored the discontinuity of exchange correlation effects among electrons; and hence the correlative reaction among excited state electrons in the multiparticle system was underestimated [114]. Thus, the computational band gap is much lower than the experimental values, generally smaller by 30 to 50% or even more. But this does not affect the analysis of electronic structure of GaSb [124]. Again the differences observed are attributed to different approximation schemes considered in our DFT calculations. Our results also suggest that appropriate choice of psudopotential is vital in obtaining the required results.

In all the band structures, the DOSs and the PDOS plot for undoped GaSb the normalized Fermi levels lie on the top of the valence band for all the three pseudopotential cases illustrate GaSb is indeed semiconductor material. The projected DOS, PDO plot (Fig. 5.12) in addition to the clear energy band gap illustration, also shows the highest peaks in the valence and conduction bands are due to Sb and Ga 2p states, respectively. The effects of the d and f states are seen to be negligible with pseudopotential pbe-mt-fhi-UPF, and pz-mt-fhi-UPF. Moreover, with pseudopotential pz-bhs-UPF, the two states did not exist and we did not see their effects.

B) Energy Band Structures, DOSs, and PDOS of Fe/GaSb

Fig. 5.13 to Fig. 5.15 show the energy band structures, the DOS, and the PDOS for Fe doped GaSb.

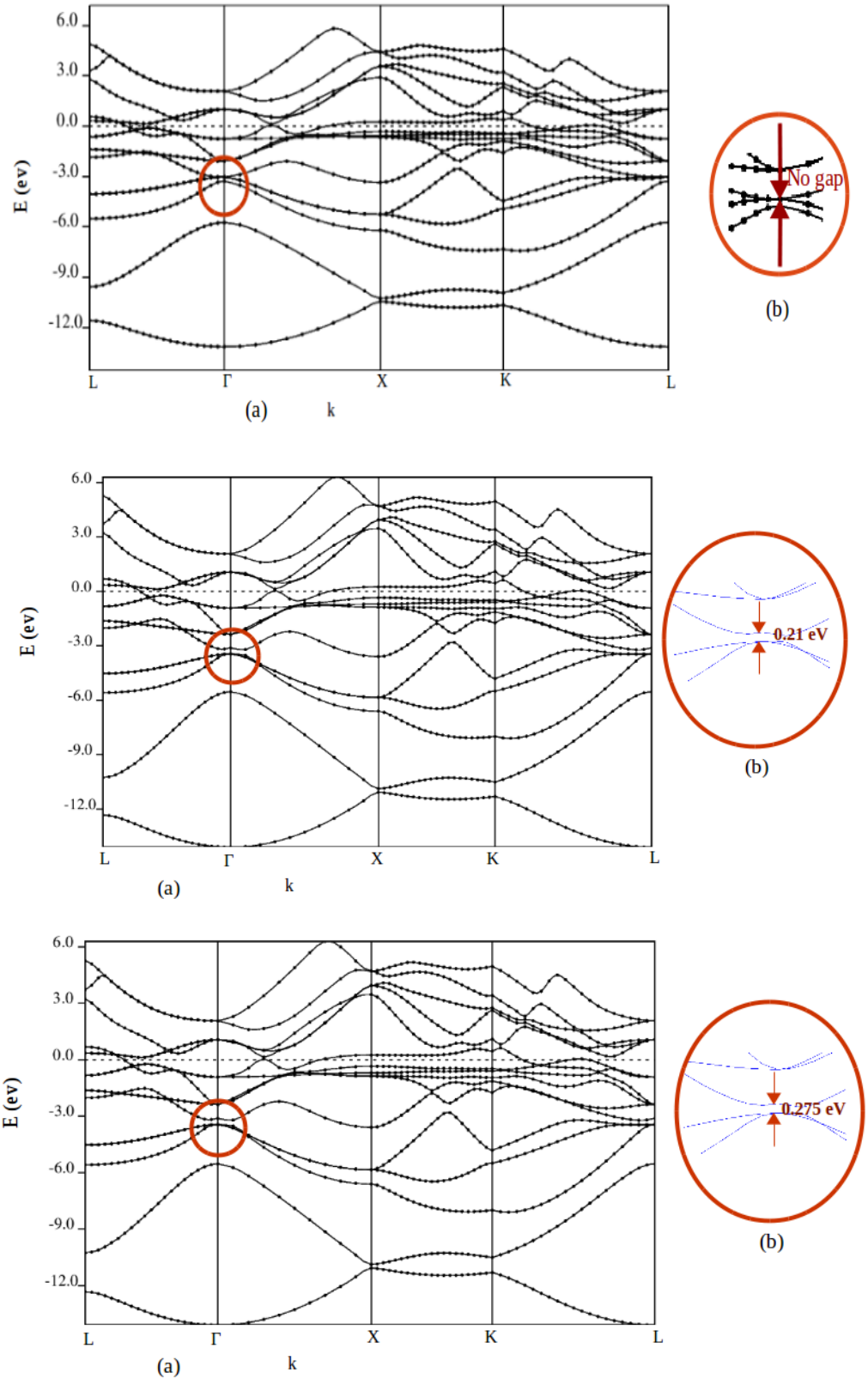

Figure 5.13: (a) Energy band structure for Fe/GaSb obtained with pseudopotential pbe-mt-fhi-UPF (top panel), pz-bhs-UPF (middle panel), and pz-mt-fhi-UPF (bottom panel), and (b) magnified view of the energy gap in the vicinity of the $k = 0$ zone center.

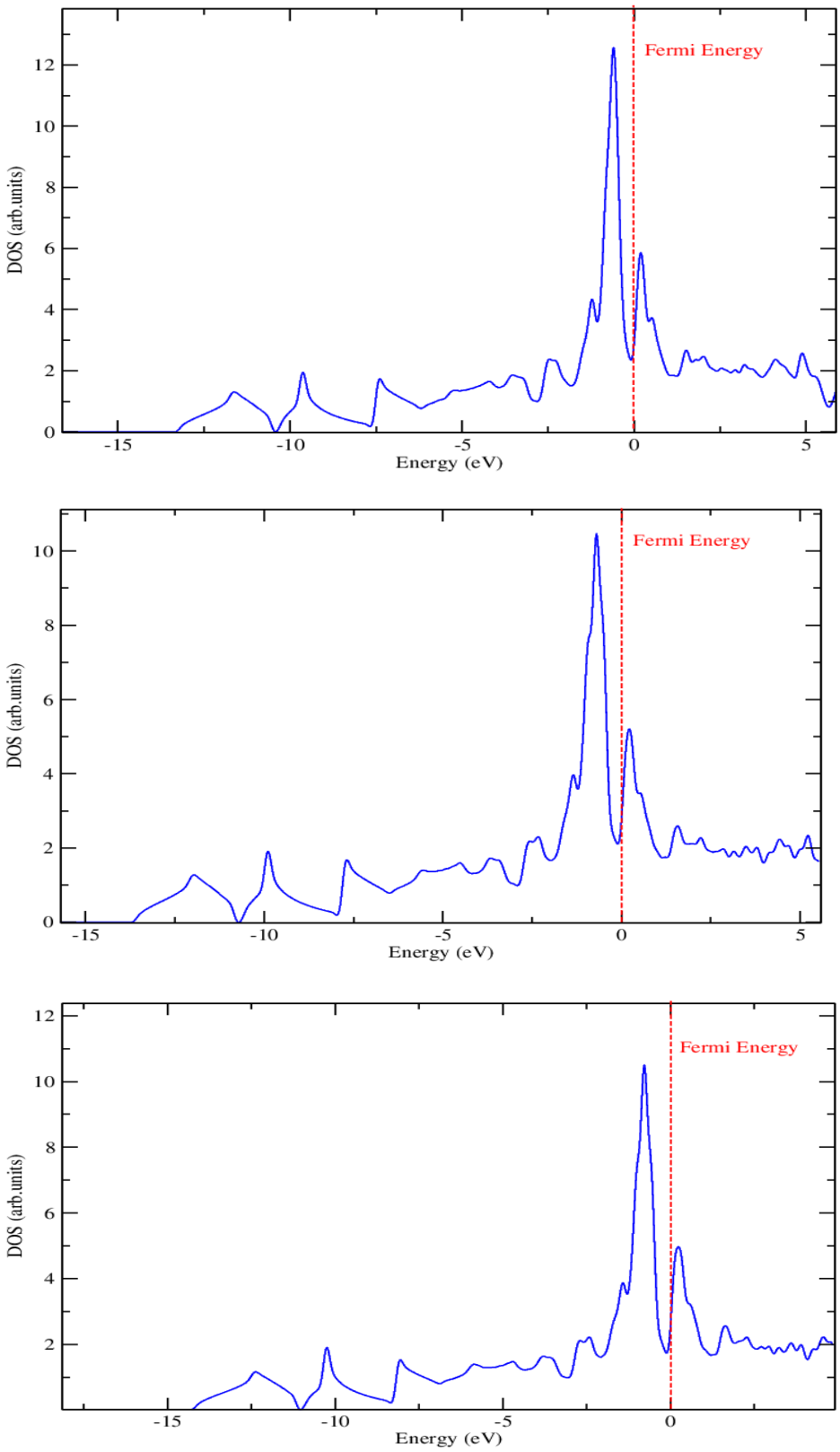

Figure 5.14: DOS plots for Fe/GaSb obtained with pseudopotential pbe-mt-fhi-UPF (top panel), pz-bhs-UPF (middle panel), and pz-mt-fhi-UPF (bottom panel).

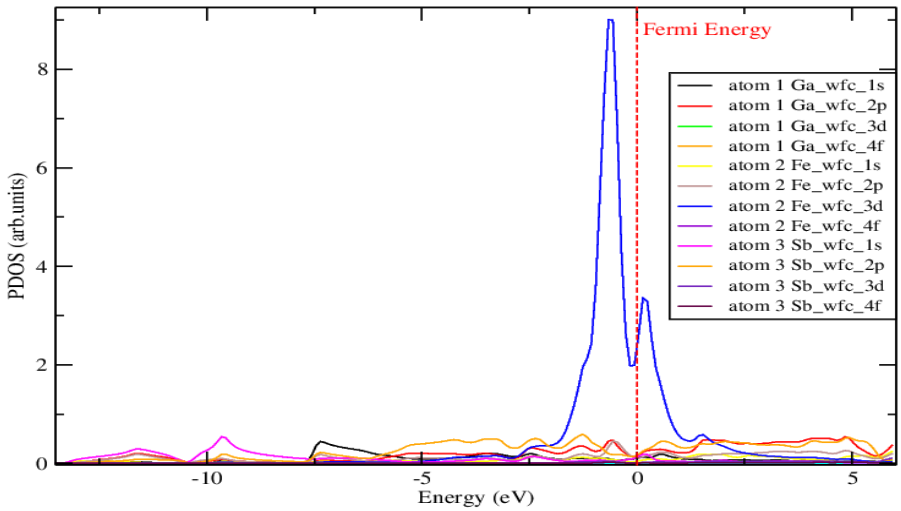

Figure 5.15: PDOS plots for Fe/GaSb obtained with pseudopotential pbe-mt-fhi-UPF.

The normalized Fermi levels (in all the band structures, the DOSs, and the PDOS plots for Fe doped GaSb) found within the conduction band for all the three psudopotential cases illustrate Fe/GaSb is semi-metallic material. We could also measure the band gap energy at Γ $[k = 0]$ points and obtain overlaps of the bottom of the conduction band and the top of the valence band for pbe-mt-fhi-UPF, 0.21 eV for pz-bhs-UPF, and 0.275 eV for pz-mt-fhi-UPF. These results show that doping reduce the band gap energy and takes the semiconductor material to semi-metallic material.

The PDOS plot for pseudopotential pbe-mt-fhi-UPF illustrates the highest peak in the valence band is due to Fe 3d state. The 3d electrons in transition metals form virtual bound states due to the strong attractive Coulomb potential, $-Z/r$, of the nucleus and the repulsive centrifugal potential, $+L(L+1)/r^2$, due to electron orbital motion, where Z and L are the atomic number and orbital quantum number, respectively [125]. Due to the density of states of the virtual bound d states, the effective exchange energy, which describes the magnetic interaction between two transition metal atoms, depends strongly on the number of d electrons and the chemical potential. The effective exchange energy is negative (i.e., is an antiferromagnetic interaction) for half-filled d shells. As the number of d electrons increases, the effective exchange energy gradually changes to a positive value (i.e., to a ferromagnetic interaction) [126].

Fig. 5.16 shows the total density of states (DOSs) for the pristine GaSb and Fe doped

GaSb. The upper and lower parts of the figure correspond to the spin up and spin down states, respectively. We obtained zero total magnetization for GaSb and 3.29 Bohr mag./cell using 6.826 $\mathring{A}$ (12.9 Bohr) lattice parameter obtained for Fe/GaSb which is less than 2.83 μ_B found in reference [126] using the experimental host GaSb lattice parameter 6.10 $\mathring{A}$ (11.52 Bohr). The difference in the local magnetic moments is mainly due to the lattice constants.

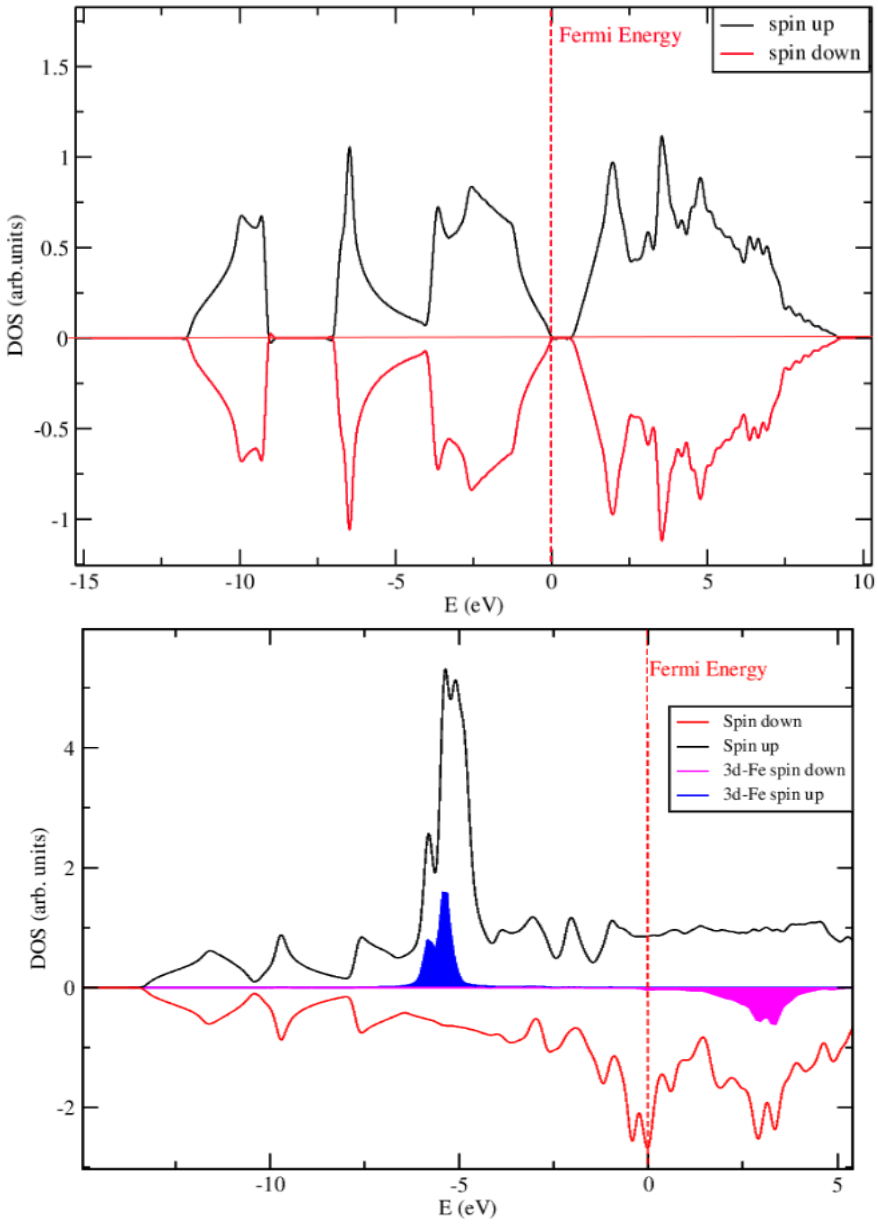

Figure 5.16: Total DOS for GaSb (top panel) and Fe/GaSb (bottom panel) obtained with pseudopotential pbe-mt-fhi-UPF. The total spin up and spin down DOSs are shown by red and black lines and the partial d DOSs are shown by magenta area for 3d-Fe spin down and blue area for 3d-Fe spin up, respectively.

5.4.6 Energy Band Structures using Hubbard Correction, DFT+U

In order to see how the band gap reduction problem in DFT calculation can be improved by DFT+U in our work, we first assumed value of the Hubbard U parameter to be $1 \times 10^{-8}\ eV$, which is essentially 0, in order just to let the code know which element we want to consider as a Hubbard atom. Convergence tests of U with respect to the kinetic-energy cutoff were then performed by hp.x code (Hubbard parameters, HP) for pbe-mt-fhi-UPF psudopotential with **k** point mesh $2 \times 2 \times 2$ and **q** point mesh $2 \times 2 \times 2$ results in converged value of U = 6.7553 eV at Ecutwfc 60 Ry as shown in (see. Fig. 5.17). The convergence tests of U with respect to the kinetic-energy cutoff is recomputed using the obtained U = 6.7553 eV as Hubbard U parameter to get more converged value of U at Ecutwfc 60 Ry and depicted in Fig. 5.18).

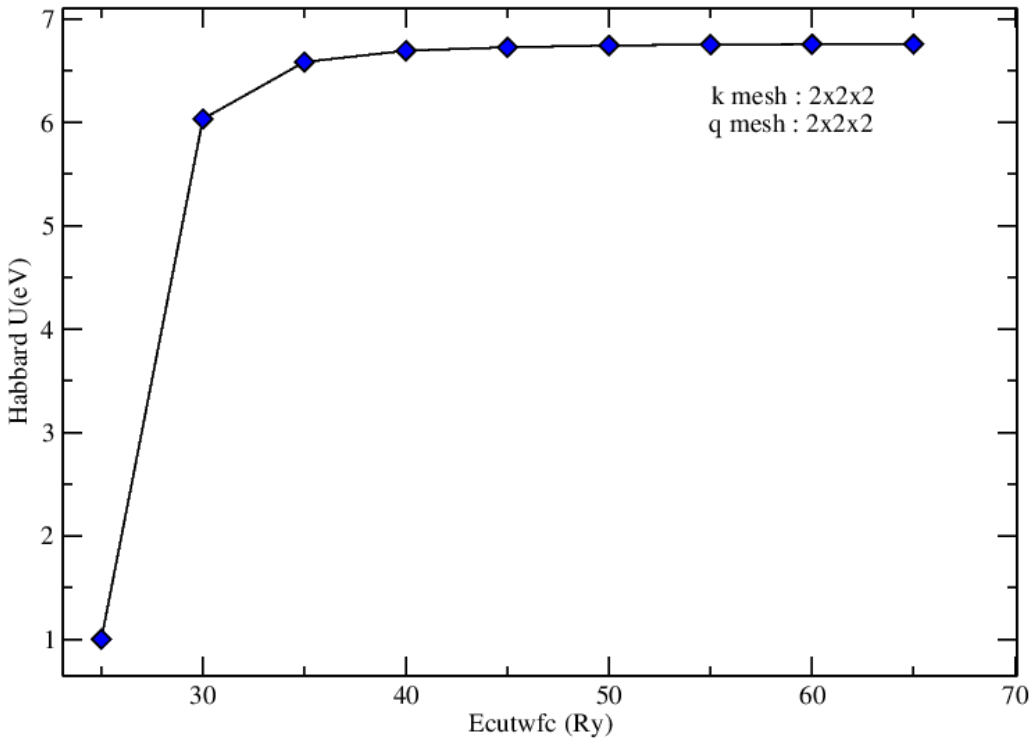

Figure 5.17: Convergence of U with respect to cutoff with **k** point mesh $2 \times 2 \times 2$ and **q** point mesh $2 \times 2 \times 2$ with Hubbard U parameter = $1 \times 10^{-8}\ eV$.

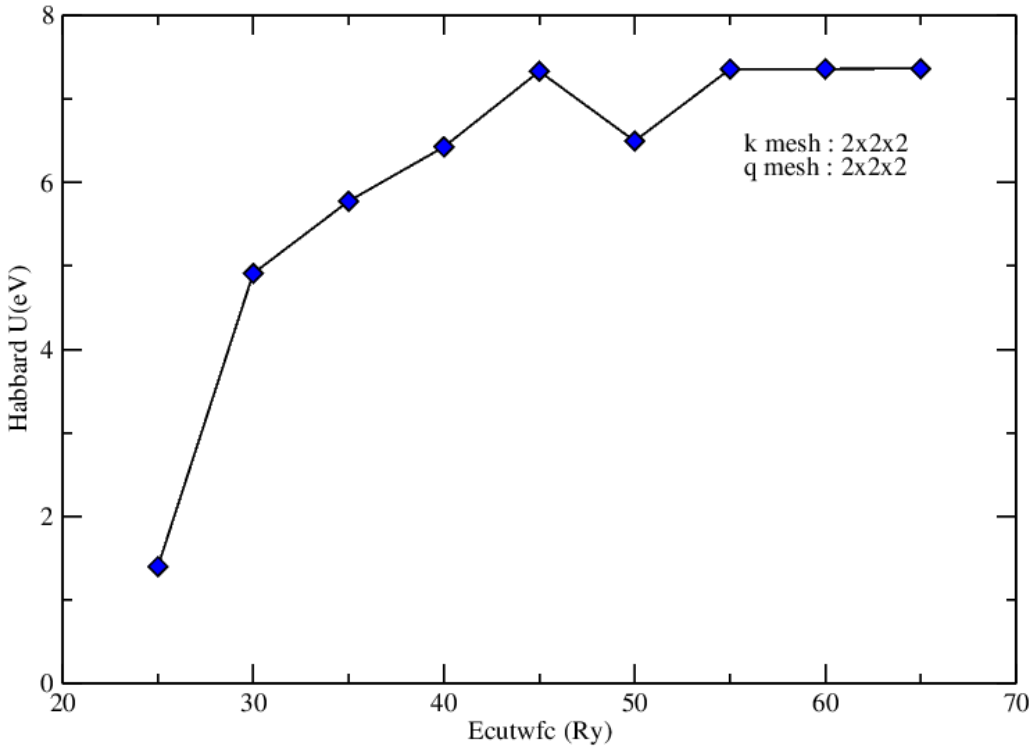

Figure 5.18: Convergence of U with respect to cutoff with **k** point mesh $2 \times 2 \times 2$ and **q** point mesh $2 \times 2 \times 2$ with Hubbard U parameter = 6.7553 eV.

Our convergence tests of U in (see. Fig. 5.18) shows at ecutwfc = 60 (Ry) and ecutrho = 240 (Ry) the new value of U = 7.3605 eV is converged very good (with the accuracy of $\approx 0.01eV$). However, this is not a universal finding of U, one has to check carefully the convergence of U with respect to the cutoff for every compound. Accordingly, the convergence tests were performed to check carefully the convergence of U with respect to the chosen ecutwfc and ecutrho with respect to the **k** mesh and **q** mesh for the combinations shown in Table 5.1.

k mesh	**q** mesh		**k** mesh	**q** mesh		**k** mesh	**q** mesh
$2 \times 2 \times 2$	$2 \times 2 \times 2$		$3 \times 3 \times 3$	$2 \times 2 \times 2$		$4 \times 4 \times 4$	$2 \times 2 \times 2$
$2 \times 2 \times 2$	$3 \times 3 \times 3$		$3 \times 3 \times 3$	$3 \times 3 \times 3$		$4 \times 4 \times 4$	$3 \times 3 \times 3$
$2 \times 2 \times 2$	$4 \times 4 \times 4$		$3 \times 3 \times 3$	$4 \times 4 \times 4$		$4 \times 4 \times 4$	$4 \times 4 \times 4$

Table 5.1: Combinations of **k** mesh and **q** mesh to perform convergence tests.

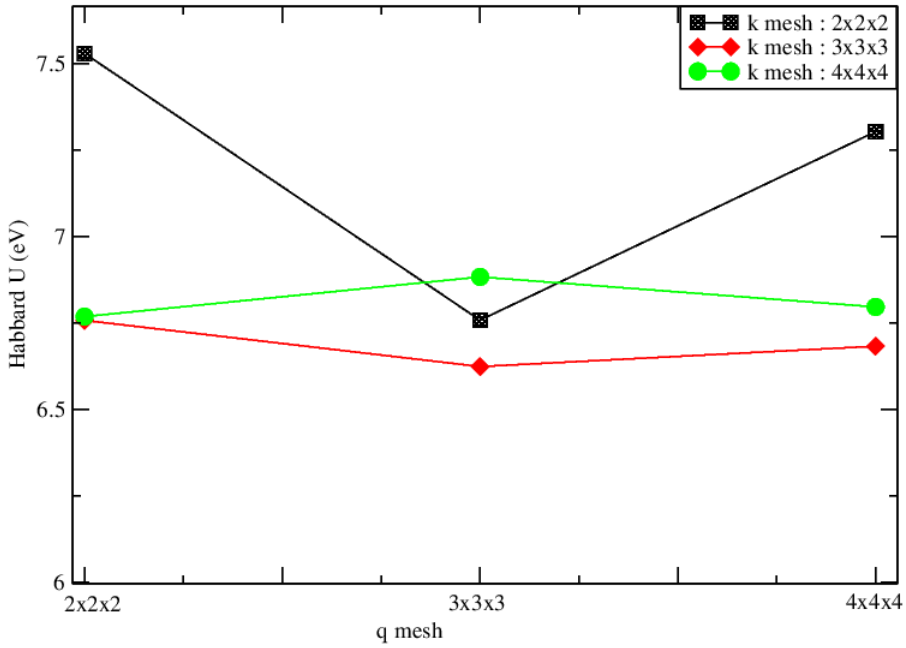

Figure 5.19: Convergence tests for combinations of **k** mesh and **q** mesh.

Fig. 5.19 illustrates the result of the performance tests for the combinations of **k** point mesh and **q** point mesh in (Table 6.1) and Hubbard value of 6.7916 eV was then chosen with the accuracy of 0.01 eV (in practice, such a high accuracy is typically not needed but considered as very good for most studies) at **k** point mesh $4\times4\times4$ and **q** point mesh $3\times3\times3$ for self-consistent U_{scf} calculations. The self-consistent computation of the a structural optimization (variable-cell (vc) relaxation) at the DFT+U level have changed the atomic position and the lattice parameters and hence U_{scf} was computed in self-consistent cycle for three iterations using the new geometry (i.e. Hubbard value of 6.7916 eV) until U_{scf} was converged. (see. Fig. 5.20).

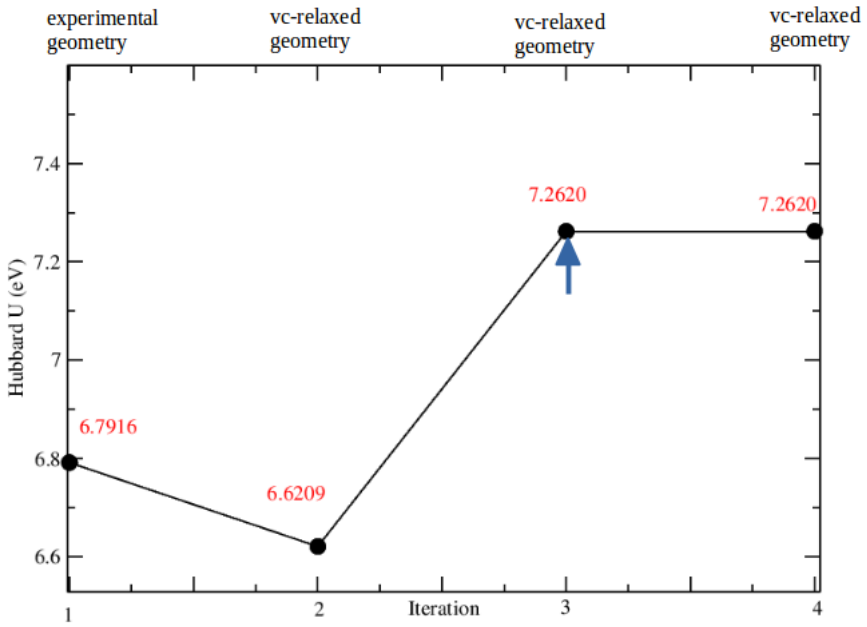

Figure 5.20: Convergence tests for self-consistent calculation of Hubbard U_{scf}.

Finally, the band structure was performed with the converged computed value of U_{scf}=7.262 eV obtained in previous steps and depicted in Fig. 5.21.

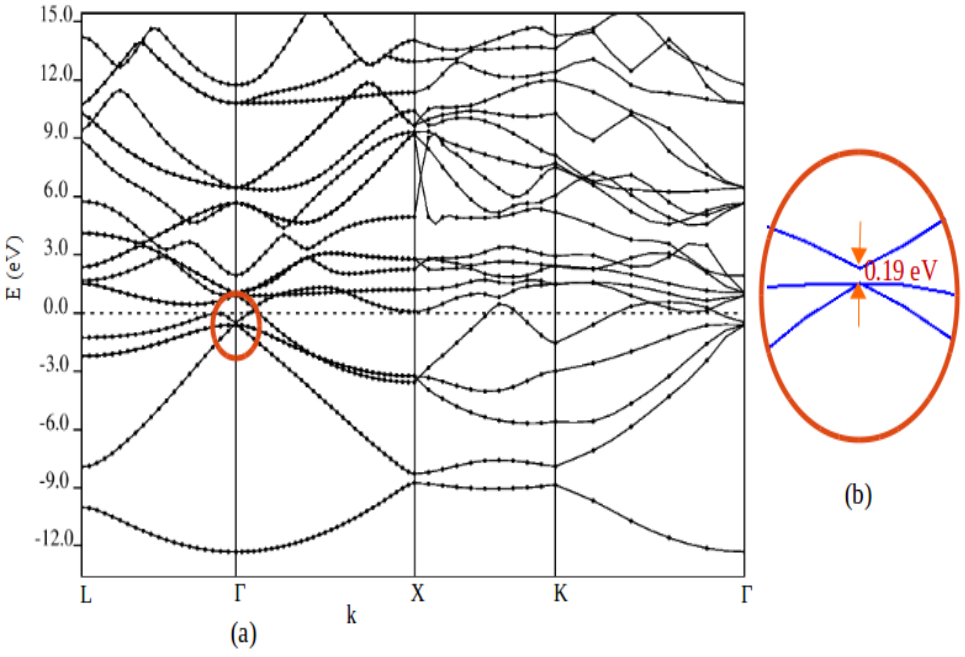

Figure 5.21: (a) Energy band structure for Fe/GaSb obtained with pseudopotential pbe-mt-fhi-UPF using DFT+U and (b) magnified view of the energy gap in the vicinity of the $k = 0$ zone center.

Fig. 5.21 shows a band gap of $E_(g) \approx 0.19\ eV$ at the Γ $[k = 0]$ point for Fe/GaSb and the result asserts that DFT+U increases the band gap and hence could rectify the band gap problem encountered during the DFT calculation.

5.4.7 Conclusion

Our investigation of the structural and electronic properties of undoped and Fe doped GaSb indicate that Fe/GaSb maintains the zinc-blende crystal structure. From the results of the different psudopotsentials, we could also observe that appropriate choice of relevant parametersis important to get a band structure as that of the host semiconductor GaSb since one psudoptential may be good at in its lattice parameter result while another one is in its band gap result. If possible, it is good to prepare a psudopotentiol which can give the same result as that of the host semiconductor. Our results also illustrated how the band gap problem encountered in heavily Fe-doped GaSb DFT calculation can be rectified by using DFT+U. Keeping the structural and electronic properties of Fe/GaSb to be as that of the host GaSb semiconductor is one of the requirement for spintronic application.

Chapter 6

Summary and Conclusions

6.1 Summary

In this thesis, we studied magnetic properties of pristine and Fe alloyed GaSb. The effect of external electric field, magnetic field, and anisotropic energy on the magnetic properties of Fe/GaSb DMS has been studied analytically with a Kondo lattice model type Hamiltonian consisting of Heisenberg type Hamiltonian describing spin-spin interaction of the Fe^{+3} localized spin, the Zeemann energy that arises when magnetic field is applied, the interaction of the localized moments with the applied magnetic field, electric field and the magnetic anisotropic energy. Such model is applicable to diluted magnetic semiconductorsdue to the fact that magnetism in them would be mediated by itinerant carriers.

Our analytical work in Chapters 2 and 3 demonstrate the feasibility of controlling the ferromagnetism of DMS externally by the application of magnetic field, electric field, and magnetic anisotropic energy. Our findings indicate the increase in the gap of the dispersion curve, magnetization and critical temperature with the increase in the magnitude of magnetic field or electric field and even more when both are applied together. On the other hand, the increase in the magnitude of the anisotropic energy results in the reduction of the dispersion band gap, magnetization and critical temperature significantly.

Further analysis show the decrease in the magnon specific heat with increase in impurity concentration contrary to the trend in magnetic susceptibility. The magnetic susceptibility (up

to the critical temperature) is also found to be significantly affected due to the magnitude of magnetic field and/or electric field and/or the magnitude of the anisotropic energy.

The applied electric field has an effect of increasing carrier concentration which in turn produces spin polarized carriers which creates a bound state: a localized hole is surrounded by the impurity spins and form bound magnetic polaron. Even though the direct exchange interaction of the localized carriers may be antiferromagnetic, the interaction between bound magnetic polarons can be ferromagnetic, when the concentration of the magnetic impurities is large enough to produce magnetization cloud. In general the analysis of the magnetic properties of the system revealed the possibility of electromagnetic manipulation of the ferromagnetism.

In Chapter 5, we have presented first principles studies of the structural and electronic properties of pristine GaSb and Fe doped GaSb in the freamwork of DFT and DFT+U using the software package quantum ESPRESSO. The summary of the results in comparison with the experimental and previous DFT works are presented in Table 6.1.

Basic parameters	**Our work**	**Experimental work**	**Previous theoretical work**
Crystal structure of GaSb	Zinc Blende	Zinc Blende [57]	Zinc Blende [127]
Crystal structure of Fe/GaSb	Zinc Blende	Zinc Blende [12]	Zinc Blende [127]
Lattice constant (Bohr) with DFT for GaSb using PP			
pbe-mt-fhi-UPF	11.75		
pw91-n-van-UPF	11.7	11.52 [119]	
pz-bhs-UPF	11.35		
pz-mt-fhi-UPF	11.30		
Lattice constant (Bohr) with DFT for Fe/GaSb using PP			
pbe-mt-fhi-UPF	12.9		
pw91-n-van-UPF	12.85		
pz-bhs-UPF	12.65		
pz-mt-fhi-UPF	12.45		
Band Gap (eV) with in DFT for GaSb using PP			
pbe-mt-fhi-UPF	0.001	0.726 [30]	0.65 [127]
pz-bhs-UPF	0.6519		
pz-mt-fhi-UPF	0.4097		
Band Gap (eV) with in DFT for Fe/GaSb using PP			
pbe-mt-fhi-UPF	0.00		
pz-bhs-UPF	0.21		
pz-mt-fhi-UPF	0.275		
Band Gap (eV) with DFT+U for Fe/GaSb using PP			
pbe-mt-fhi-UPF	0.19		

Table 6.1: Summary of obtained results along with experimental and previous DFT work results.

6.2 Conclusions

The work reported in this thesis focus on the external manipulation of the ferromagnetism of Fe/GaSb DMS. The main conclusions are as follows:

1. The presence of the external magnetic field, electric field, and the magnetic anisotropic energy in the Hamiltonian of the system is responsible for the controllability of the ferromagnetic properties.

2. The magnon energy is found to increase as the external magnetic and electric fields increase. As a result, the spontaneous magnetization of the system increases and hence the T_c increases. Due to this, such materials have received considerable attention in recent years as potential high T_c DMSs, which is the first important requirement that received considerable attention in recent years as potential semiconductor spintronics devices.

3. The calculation of the static magnetic susceptibility also confirms the tunning of the ferromagnetism using the external magnetic and electric fields.

4. In our approach, the ferromagnetic coupling of the carriers with the electric field leads to an additional term in the effective molecular field. As a result large spin polarized carriers, which depend on the external electric field is produced in the system. These spin polarized carriers have the advantage that the ferromagnetism in semiconductors is adjustable through the carrier density.

5. Our investigation of the structural and electronic properties of pristine and Fe doped GaSb indicate that Fe/GaSb maintains the zinc-blende crystal structure.

6. From the results of the different pesudopotsentials, we could also observe that appropriate choice of pesudopotential is important to get the structural and electronic properties as that of the host semiconductor GaSb or near to it which is another important requirement in semiconductor spintronics devices.

7. Our result also illustrated the use of DFT+U in correcting the band gap problem encountered in heavily Fe-doped GaSb with DFT calculation by, using DFT+U.

6.3 Future Outlook

The studies presented in the thesis were mainly focussed on bulk DMS material, though the phenomena has been demonstrated for thin films and nanostructures. In future, we would investigate magnetic as well as spin dependent transport properties such as anomalous Hall effect for thin films and nanostructures materials.

We would also perform the structural, electronic, magnetic, and others properties using DFT calculations for the system considered in this thesis with high computing computers for more precise results and compare our results in detail with experimental results with approprate pseudopotential.

For correcting band gap problems and others, we would apply hybrid functional method and compare its effect with the Hubbard correction methods.

Bibliography

[1] H. Munekata, H. Ohno, S. Von Molnar, A. Segmller, L. L. Chang, and L. Esaki, *Diluted magnetic III-V semiconductors*, Phys. Rev. Lett. **63**, 1849 (1989).

[2] T. Dietl, H. Ohno, F. Matsukura, J. Cibert, and D. Ferrand, *Zener model description of ferromagnetism in zinc-blende magnetic semiconductors*, Science **287**, 1019 (2000).

[3] H. Ohno, F. Matsukura, and Y. Ohno, *Semiconductor Spin Electronics*, General report, Cutting edge1 (2002).

[4] J. K. Furdyna and J. Kossut (Eds), *Semiconductor and Semimetals*, Volume **25**, Academic press, New York (1988).

[5] T. Jungwith, J. Sinova, J. Maek, J. Kuera, and A. H. MacDonald, *Theory of ferromagnetic (III,Mn)V semiconductors*, Rev. Mod. Phys. **78**, 809 (2006).

[6] T. Jungwirth, Jairo Sinova, J. Maek, J. Kuera, A. H. MacDonald, *Condensed Matter*, Vol. **78**, pp. 802-830 (2006).

[7] H. Shinya, T. Fukushima, A. Masago, K. Sato, and H. Katayama-Yoshida, *First-principles prediction of the control of magnetic properties in Fe-doped GaSb and InSb*, J. Appl. Phys. **124**, 103902 (2018).

[8] M. Tanaka, S. Ohya, and P. N. Hai, *Recent progress in III-V based ferromagnetic semiconductors: Band structure, Fermi level, and tunneling transport*, Appl. Phys. Rev. **1**, 011102 (2014).

[9] P. N. Hai, D. Sasaki, L. D. Anh, and M. Tanaka, *Heavily Fe-doped n-type ferromagnetic semiconductor (In,Fe)Sb with high Curie temperature and large magnetic anisotropy*, Appl. Phys. Lett. **100**, 262409 (2012).

[10] P. N. Hai, L. D. Anh, S. Mohan, T. Tamegai, M. Kodzuka, T. Ohkubo, K. Hono, and M. Tanaka, *Growth and characterization of n-type electron-induced ferromagnetic semiconductor (In,Fe)As*, Appl. Phys. Lett. **101**, 182403 (2012).

[11] P. N. Hai, L. D. Anh, and M. Tanaka, *Electron effective mass in n-type electron-induced ferromagnetic semiconductor (In,Fe)As: Evidence of conduction band transport*, Appl. Phys. Lett. **101**, 252410 (2012).

[12] N. T. Tu, P. N. Hai, L. D. Anh, and M. Tanaka, *Magnetic properties and intrinsic ferromagnetism in (Ga,Fe)Sb ferromagnetic semiconductors*, Phys. Rev. B. **92**, 144403 (2015).

[13] N. T. Tu, P. N. Hai, L. D. Anh, and M. Tanaka, *High-temperature ferromagnetism in heavily Fe-doped ferromagnetic semiconductor (Ga,Fe)Sb*, Appl. Phys. Lett. **108**, 192401 (2016).

[14] P. N. Hai, L. D. Anh, S. Mohan, T. Tamegai, M.Kodzuka, T. Ohkubo, K. Hono, and M. Tanaka, *Growth and characterization of n-type electron-induced ferromagnetic semiconductor (In,Fe)As*, Appl. Phys. Lett. **101**, 182403 (2012).

[15] L. D. Anh, D. Kaneko, P. N. Hai, and M. Tanaka, *Growth and characterization of insulating ferromagnetic semiconductor (Al,Fe)Sb*, Appl. Phys. Lett. **107**, 232405 (2015).

[16] H. Ohno, *Making Nonmagnetic Semiconductors Ferromagnetic*, Science **281**, 951 (1998).

[17] R. Janisch, P. Gopal and N. A. Spalding, *Transition metal-doped TiO_2 and ZnO - present status of the field*, J. Phys.: Condens. Matter **17**, R657 (2005).

[18] B. T. Matthias, R. M. Bozorth, and J. H. Van Vleck, *Ferromagnetic Interaction in EuO*, Phys. Rev. Lett. **7**, 160 (1961).

[19] A. Mauger and C. Godart, *The magnetic, optical, and transport properties of representatives of a class of magnetic semiconductors: The europium chalcogenides*, Phys. Rep. **141**, 51 (1986).

[20] J. K. Furdyna, *Diluted magnetic semiconductors*, J. Appl. Phys. **64**, R29 (1988).

[21] M. Dinu, I. Miotkowski, and D. D. Nolte, *Photorefractive Semiconductors and Quantum-Well Structures*, Phys. Rev. B **58**, 10435-10442 (1998).

[22] S. Rodrizuez and A. K. Ramdas, *Raman scattering by diluted magnetic semiconductors*, Pure and Appl. Chem., **59**, 1269-1284 (1987).

[23] M. V. Schilfgaarde and O. N. Myrasov, A*nomalous exchange interactions in III-V dilute magnetic semiconductors*, Phys. Rev. B **63**, 233205 (2001).

[24] K. W. Edmonds, K. Y. Wang, R. P. Campion, A. C. Neumann, N. R. S. Farley, B. L. Gallagher and C. T. Foxon, *High-Curie-temperature $Ga_{1-x}Mn_xAs$ obtained by resistance-monitored annealing*, Appl. Phys. Lett. **81**, 4991 (2002).

[25] D. Chiba, K. Takamura, F. Matsukura and H. Ohno, *Effect of low-temperature annealing on (Ga,Mn)As trilayer structures*, Appl. Phys. Lett.**82** 3020 (2003).

[26] L. Chen, X. Yang, F. Yang, J. Zhao, J. Misuraca, P. Xiong, and S. von Molnar, *Enhancing the Curie Temperature of Ferromagnetic Semiconductor (Ga,Mn)As to 200 K via Nanostructure Engineering*, Nano Lett. **11**, 2584 (2011).

[27] C. Kittel, *Introduction to Solid State Physics*, 8^{th} ed., California, Berkeley (2005).

[28] H. Hayashi, *Development of semiconductor devices-in search of immense possibility*, World Scientific Publishing Campany (2011).

[29] Matthew Hartmann Kane, *Investigation of the Stability of Wide band gap Diluted Magnetic Semiconductor for Spintronics*, Doctoral Thesis, Georgia Institute of Technology (2007).

[30] K. Sato, P. H. Dederichsa, H. Katayama-Yoshida, J. Kudrnovsky, *Dilute Magnetic Semiconductor: A Review of Theoretical Status*, Physica B**340**-342 863-869 (2003).

[31] Shivaraman Ramachandran, *Zinc Oxide based Diluted Magnetic Semiconductors*, PhD Thesis, North Carolina State University (2006).

[32] Yared Solomon, The Study of Ferromagnetism in Diluted Magnetic Semiconductor GaMnAs (2010).

[33] T. Kammermeier, *Structural and magnetic investigation of dilute magnetic semiconductors based on GaN and ZnO,* Doctoral Thesis, University of Duisburg, Essen (2008).

[34] K. Sato, and H. Katayama-Yosida, *First principles materials design for semiconductor spintronics*, Semicond. Sci. Technol. **17**, 367, 114 (2002).

[35] B. C. Rai, Kr. Sujeet and K. R. Ranjan, S*ome Inadequacies in Theories of Dilute Magnetic Semiconductors*, ISSN 0974-3081 Vol. **5**, pp. 1-5 (2014).

[36] L. M. Sandratskii, P. Bruno, *Exchange interactions and Curie temperature in (Ga,Mn)As*, Phys. Rev. B**66**, 134435, 114-115 (2002).

[37] L. M. Sandratskii, P. Bruno, *Electronic structure, exchange interactions, and Curie temperature in diluted III-V magnetic semiconductors: (GaCr)As, (GaMn)As, (GaFe)As*, Phys. Rev. B **67**, 214402 (2003).

[38] P. Kacman, *Spin interactions in diluted magnetic semiconductors and magnetic semiconductor structures*, Semicond. Sci. Technol. **16**, R**25** 114-124 (2001).

[39] J. Konig, J. Schliemann, T. Jungwirth, A.H. MacDonald, *Disorder effects in diluted magnetic semiconductors*, Cond-Mat. 0111314 (2003).

[40] P. Mahadevan, A. Zunger, *First-principles investigation of the assumptions underlying model-Hamiltonian approaches to ferromagnetism of 3d impurities in III-V semiconductors*, Phys. Rev. B **69**, 115211 (2004).

[41] Mikls Csontos, *High pressure magnetotransport study of (III,Mn)V dilute magnetic semiconductors*, Budapest University of Technology and Economics, Department of Physics (2007).

[42] Otfried, *Madelung Semiconductor*s, **116**, 317 (1996).

[43] Alexander O. E. Animalu, I*ntermediate quantum theory of crystalline solids*, **293**, 516 (1997).

[44] P. Krstajic and F. M. Peeters, V. A. Ivanov, V. Fleurov, and K. Kikoin, *Double-exchange mechanisms for Mn-doped III-V ferromagnetic semiconductors*, Phys. Rev. B **70**, 195215 (2004).

[45] R. Bouzerar, G. Bouzerar, and T. Ziman, *Why RKKY exchange integrals are inappropriate to describe ferromagnetism in diluted magnetic semiconductors*, Phys. Rev. B **73**, 024411 (2006).

[46] W. Heisenberg, *On the theory of ferromagnetism*, Z. Phys. **49**, 613 (1928).

[47] S. Hilbert and W. Nolting, *Magnetism in (III,Mn)-V diluted magnetic semiconductors: Effective Heisenberg model*, Phys. Rev. B **71**, 113204 (2005).

[48] L. Brey and G. Gomez-Santos, *Magnetic properties of GaMnAs from an effective Heisenberg Hamiltonian*, Phys. Rev. B **68**, 115205 (2003).

[49] T. Dietl, H. Ohno, and F. Matsukura, *Hole-mediated ferromagnetism in tetrahedrally coordinated semiconductors*, Phys. Rev. B **63**, 195205 (2001).

[50] C. Zener, I*nteraction Between the d Shells in the Transition Metals*, Phys. Rev. **81**, 440 (1950).

[51] Indium antimonide, Wikipedia, the free encyclopedia (2012).

[52] Gallium antimonide, Wikipedia, the free encyclopedia (2012).

[53] R. D. Baxter, R. T. Bate, and F. J. Reid, *Semiconductors and semimetals*, J. Phys. Chem. Solids **26**, 41 (1965).

[54] P. S. Dutta, C. Marln, E. Dieguez, H. L. Bhat, *Compositional mapping of GaSb wafers from as-grown crystals and after post-growth annealing treatments*, J. of Crystal Growth **160**, 207-210 (1996).

[55] C. Anayama, T. Tanahashi, H. Kuwatsuka, S. Nishiyama, S. Isozumi, and K. Nakajima, *High-purity GaSb epitaxial layers grown from Sb-rich solutions*, Appl. Phys. Lett. **56**, 239 (1990).

[56] K. F. Longenbach and W. I. Wang, *Molecular beam epitaxy of GaSb*, Appl. Phys. Lett. **59**, 2427 (1991).

[57] V. Nahirnyak, *Gallium antimonide (GaSb)*, Department of Physics, University of Cincinnati, Ohio 45221 (2002).

[58] A. Rogalski, P. Martyniuk, and M. Kopytko, *InAs/GaSb type-II superlattice infrared detectors: Future prospect*, Appl. Phys. Rev. **4**, 031304 (2017).

[59] C. Kittel, *Introduction to Solid State Physics*, 4^{th} edition (1971).

[60] R. Shioda, K. Ando, T. Hayashi, M. Tanaka, *Magnetic-field-induced structural phase transition in* $Gd_5(Si_{1.8}Ge_{22})$, Phys. Rev. B **58**, 1100-1102 (1998).

[61] A. Rahane, M. Deshpande, R. Pandey, *Theoretical study of small clusters of manganese-doped gallium oxide:* $Mn(GaO)_n$ *and* $Mn_2(GaO)_n$ *with* $n = 1 - 7$, J Nanopart Res, DOI **10**.1007/s11051-010-9871-z (2010).

[62] M. Kuzma, I. Stefaniuk, and M. Bester, *Symmetry and Structural Properties of Condensed Matter*, pp. 1-12 (2009).

[63] C. Kittel, *Quantum Theory of Solids*, 2^{nd} Ed., John Wiley and Sons Inc., University of California (1987).

[64] N. W. Ashcroft, and N. D. Mermin, *Solid State Physics*, Thomson Learning, Inc. (1976).

[65] C. Kittel, *Introduction to Solid State Physics*, Wiley, New York (1986).

[66] T. Holstein and H. Primakoff, *Field Dependence of the Intrinsic Domain Magnetization of a Ferromagnet*, Phys. Rev., **58**, 1098 (1940).

[67] H. Ohno, D. Chiba, F. Matsukura, T. Omiya, E. Abe, T. Dietl, Y. Ohno, and K. Ohtani, *Electric Field Controlled Ferromagnetism*, Nature, **408**, 21 (2000).

[68] D. Chiba, F. Matsukura, and H. Ohno, *Electric-field control of ferromagnetism in (Ga,Mn)As*, Appl. Phys. Lett **89**, 162505 (2006).

[69] P. M. Shand, A. D. Christianson, T. M. Pekare, L. S. Martinson, J. W. Schweitzer, I. Miotkowski, and B. Crooker, *Spin-glass ordering in the diluted magnetic semiconductor* $Zn_{1-x}Mn_xTe$, Phys. Rev. B **58**, 12786 (1998).

[70] R. Kishore and P. Singh, *A phenomenological theory for spin-glass ordering in Fe doped* $YBa_2Cu_3O_{7+y}$, Supercond. **7**, 631 (1994).

[71] S. J. Peaton, C. R. Abernathy, D. P. Norton, A. F. Hebard, Y. D. Park, L. A. Boatner, and J. D. Budai, *Materials Science and Engineering*, R. **40**, 137 (2003).

[72] J. I. Climente, M. Korkusinski, P. Hawrylak, J. Planelles, *Voltage control of the magnetic properties of charged semiconductor quantum dots containing magnetic ions*, Phys. Rev. B **71**, 123 (2005).

[73] F. Xiu, Y. Wang, J. Kim, A. Hong, J. Tang, A. P. Jacob, J. Zou, K. L. Wang, *Electric-field controlled ferromagnetism in high-Curie-temperature* $Mn_{0.05}Ge_{0.95}$ *quantum dots*, Nat. Mater. **9**, 337344 (2010).

[74] H. Boukari, P. Kossacki, M. Bertolini, D. Ferrand, J. Cibert, S. Tatarenko, A. Wasiela, J. A. Gaj, T. Dietl, *Light and Electric Field Control of Ferromagnetism in Magnetic Quantum Structures*, Phys. Rev. B **88**, 207204 (2002).

[75] S. A. Wolf, D. D. Awschalom, R. A. Buhrman, J. M. Daughton, S. von Molnr, M. L. Roukes, A. Y. Chtchelkanova, and D. M. Treger, *Spintronics: A Spin-Based Electronics Vision for the Future*, Science **294**, 1488 (2001).

[76] T. Dietl, *Advances in Solid State Physics*, Acta Phys. Polon. A **100**, 139 (2001).

[77] H. Sato, *Progress in Low Temperature Physics*, Progr. Theoret. Phys. **13**, 119 (1955).

[78] C. Amente, *Study of Photo-induced Ferromagnetism in Diluted Magnetic Semiconductor (Ga,Mn)As*, PhD Thesis, Department of Physics, Addis Ababa University (2010).

[79] A. Twardowski, H. J. M. Swagten, W. J. M. de Jonge, and M. Demianiuk, Magnetic behavior of the diluted magnetic semiconductor $Zn_{1-x}MnxSe$, Phys. Rev. B **44**, 2220 (1991).

[80] C. Fiolhais F. Nogueira M. Marques, *A Primer in Density Functional Theory*, Springer-Verlag, New York (1965).

[81] J. Toulouse, *Introduction to density-functional theory*, Laboratoire de Chimie Thorique, Universit Pierre et Marie Curie et CNRS, 75005, Paris, France (2017).

[82] H. Eschrig, *The Fundamentals of Density Functional Theory*, Institute for Solid State and Materials Research and University of Technology, Dresden, Germany (1996).

[83] M. Springborg, *Methods of electronic structure calculations*, John Wiley and Sons (2000).

[84] R. M. Martin, *Electronic structure: Basic theory and Practical Methods*, Cambridge University Press (2008).

[85] J. Kohanoff, *Electronic structure calculations for solids and molecules: Theory and computational methods*, Cambridge University Press (2006).

[86] D. Sholl and J. A. Steckel, *Density functional theory: a practical introduction*, John Wiley and Sons (2009).

[87] F. Giustino, *Material Modelling Using Density Functional Theory: Properties and prediction*, Oxford University Press (2014).

[88] P. Hohenberg and W. Kohn, *Inhomogeneous Electron Gas*, Phys. Rev. **136**, B 864 (1964).

[89] M. Levy, *Universal variational functionals of electron densities, first-order density matrices, and natural spin-orbitals and solution of the v-representability problem*, Proc. Natl. Acad. Sci. U.S.A. **76**, 6062 (1979).

[90] M. Levy, *Electron densities in search of Hamiltonians*, Phys. Rev. A **26**, 1200 (1982).

[91] E. H. Lieb, *Density functionals for Coulomb systems*, Int. J. Quantum Chem. **24**, 24 (1983).

[92] W. Kohn and L. J. Sham, *Self-Consistent Equations Including Exchange and Correlation Effects*, Phys. Rev. **140**, 1133 (1965).

[93] T. Helgaker, P. Jorgensen, and J. Olsen, *Density-Functional Theory: A Convex Treatment*, Wiley-Blackwell (2016).

[94] E. Fermi Z. Phys. **48** 73 (1928); L. H. Thomas, Proc. Camb. Phil. Soc. **23** 542 (1927); these articles are reproduced in N. H. March, *Self Consistent Fields in Atoms*, Plenum, Oxford (1975).

[95] P. A. M. Dirac, *Note on Exchange Phenomena in the Thomas Atom*, Proc. Camb. Phil. Soc. **26**, 376 (1930).

[96] R. G. Parr, and W. Yang, *Density-Functional Theory of Atoms and Molecules*, OUP, Oxford (1989).

[97] E. H. Lieb, *Thomas-Fermi and related theories of atoms and molecules*, Rev. Mod. Phys., **53**, 603 (1981).

[98] D. M. Ceperley and B. J. Alder, *Ground State of the Electron Gas by a Stochastic Method*, Phys. Rev. Lett., **45**, 566 (1980).

[99] J. P. Perdew and A. Zunger, *Self-interaction correction to density-functional approximations for many-electron systems*, Phys. Rev. B **23**, 5048 (1981).

[100] U. von Barth and L. Hedin, *A local exchange-correlation potential for the spin polarized case*, J. Phys. C **5**, 1629 (1972).

[101] S. H. Vosko, L. Wilk and M. Nusair, *Accurate spin-dependent electron liquid correlation energies of local spin density calculations: a critical analysis*, Can. J. Phys. **58**, 1200 (1980).

[102] N. M. Harrison, *An Introduction to Density Functional Theory*, Department of Chemistry, Imperial College of Science Technology and Medicine, SW7 2AY, London and CLRC, Daresbury Laboratory, Daresbury, Warrington, WA4 4AD.

[103] R. M. Dreizler and E. K. U. Gross, *Density Functional Theory* , Springer Verlag, Berlin (1990).

[104] Y. Yang, J. P. Perdew, J. A. Cevary, L. D. Macdonald and S. H. Vosko, *Exchange potentials in density-functional theory,* Phys. Rev. A **41**, 78 (1990).

[105] J. P. Perdew and Y. Wang, *Accurate and simple density functional for the electronic exchange energy: Generalized gradient approximation*, Phys. Rev. B **33**, 8800 (1986).

[106] J. P. Perdew, *in Electronic Structure of Solids*, edited by P. Ziesche and H. Eschrig, Akademie Verlag, Berlin (1991).

[107] A. D. Becke, *A multicenter numerical integration scheme for polyatomic molecules*, J. Chem. Phys. **88**, 2547 (1988).

[108] K. Burke, J. P. Perdew, and Y. Wang, *Derivation of a generalized gradient approximation: The PW91 density functional*, Plenum, NY, p. 81 (1997).

[109] J. P. Perdew, K. Burke, and M. Ernzerhof, *Generalized Gradient Approximation Made Simple*, Phys. Rev. Lett., **77**, 3865 (1996).

[110] A. D. Becke, *A new mixing of Hartree-Fock and local densityfunctional theories*, Phys. Rev. **98**, 1172 (1992).

[111] J. Heyd, G. E. Scuseria, and M. Ernzerhof, *Hybrid functionals based on a screened Coulomb potential*, Phys. Rev. **118**, 8727 (2003).

[112] V. I. Anisimov and O. Gunnarsson, *Density-functional calculation of effective Coulomb interactions in metals*, Phys. Rev. B **43**, 7570 (1991).

[113] V. I. Anisimov, J. Zaanen, and O. K. Andersen, *Band theory and Mott insulators: Hubbard U instead of Stoner*, Phys. Rev. B **44**, 943 (1991).

[114] V. I. Anisimov, F. Aryasetiawan, and A. I. Lichtenstein, *First-principles calculations of the electronic structure and spectra of strongly correlated systems: the LDA+U method*, J. Phys.: Condens. Matter **9**, 767 (1997).

[115] G. Kresse and J. Furthm, *Efficient iterative schemes for ab initio total-energy calculations using a plane-wave basis set*, Phys. Rev. B **54**, 11169 (1996).

[116] H. J Monkhorst and J. D.Pack, *Special points for Brillouin-zone integrations*, Phys. Rev. B **13**, 5188 (1976).

[117] P. Schwerdtfeger, *The Pseudopotential Approximation in Electronic Structure Theory*, Chem. Phys. Chem., Vol. **12**, 3143 - 3155 (2011).

[118] P. Giannozzi, *Introduction to quantum ESPRESSO:* Hands-on Tutorial on Electronic Structure Computations, Universit di Udine and IOM-Democritos, ICTP Trieste, Italy (2013).

[119] I. G. Greenfield and R. L. Smith, *Phase equilibria in ternary III-V systems*, Trans. A1ME **203**, 351 (1955).

[120] M. G. Holland, *Semiconductors and Semimetals*, edited by R. K. Willardson and A. C. Beer, New York (1966).

[121] A. Joullie, A. Z. Eddine, and B. Girault, *Resonant tunneling in AlSb-GaSb-AlSb and AlSb-InGaSb-AlSb double barrier heterostructures,* Phys. Rev. B **23**, 928 (1981).

[122] M. J. Frisch, et al, *Gaussian 09*, Inc., Pittsburgh, PA (2009).

[123] D. Apoorva, P. Saurabh, M. Neeraj, *Journal of Computational Methods in Molecular Design*, Department of Physics, Lucknow University, Lucknow, 3 (1): 1-8 (2013).

[124] W. E. Pickett, P*seudopotential methods in condensed matter applications*, Comput. Phys. Rep. **9**, 115 (1989).

[125] J. Friedel, *Metallic alloys*, Nuovo Cimento **7**, 287 (1958).

[126] H. Shinya, T. Fukushima, A. Masago, K. Sato, and H. Katayama-Yoshida, *First-principles prediction of the control of magnetic properties in Fe-doped GaSb and InSb*, J. Appl. Phys. **124**, 103902 (2018).

[127] S. Q Wang and H. Q. Ye, *A plane wave pseudopotential study on III-V semiconductor under pressure*, Journal of Physics: Condensed Matter, Vol. **14**, 9579-9587 (2002).

Publication

1. Mesfin Birile, Chernet Amente, and P Singh, *Effects of Magnetic Field, Electric Field, and Magnetic Anisotropic Energy on the Magnetic Properties of Fe Alloyed GaSb Diluted Magnetic Semiconductor*, AIP Advances **10**, 035120 (2020). [Published]

2. Mesfin Birile, Chernet Amente, and P Singh, *Magnon Specific Heat and Magnetic Susceptibility of Fe Alloyed GaSb Diluted Magnetic Semiconductor in the Presence of Magnetic Field, Electric Field, and Magnetic Anisotropic Energy.* [Submitted]

DECLARATION

I hereby declare that this PhD dissertation is my original work, has not been presented for a degree in any other university and that all the sources of material used for the dissertation have been dully acknowledged.

Name: Mesfin Birile

Signature: _____

This PhD dissertation has been submitted for examination with our approval as University advisor.

Name: Prof. P. Singh

Signature: _____

Name: Dr. Chernet Amente

Signature: _____

Place and time of submission:

Addis Ababa University

August 2020